Optische-val-gecontroleerde elektroforese
voor markeringvrije biodetectie

Optical Trapping Electrophoresis for Label-Free Biodetection

Toon Brans

Promotoren: prof. dr. ir. F. Beunis, prof. dr. ir. K. Neyts
Proefschrift ingediend tot het behalen van de graad van
Doctor in de Ingenieurswetenschappen: Fotonica

Vakgroep Elektronica en Informatiesystemen
Voorzitter: prof. dr. ir. R. Van de Walle
Faculteit Ingenieurswetenschappen en Architectuur
Academiejaar 2014 - 2015

UNIVERSITEIT
GENT

ISBN 978-90-8578-821-8
NUR 950, 910
Wettelijk depot: D/2015/10.500/65

Universiteit Gent
Faculteit Ingenieurswetenschappen en Architectuur
Vakgroep Elektronica en Informatiesystemen

Promotoren:

Prof. dr. ir. Filip Beunis
Prof. dr. ir. Kristiaan Neyts

Examencommissie:

Prof. dr. ir. Jan Van Campenhout (voorzitter)	Universiteit Gent
Prof. dr. ir. Filip Beunis (promotor)	Universiteit Gent
Prof. dr. ir. Kristiaan Neyts (promotor)	Universiteit Gent
Dr. ir. Filip Strubbe (secretaris)	Universiteit Gent
Prof. dr. ir. Peter Bienstman	Universiteit Gent
Prof. dr. Jérôme Duval	Université de Lorraine
Prof. dr. Jeroen Lammertyn	Katholieke Universiteit Leuven
Prof. dr. Laszlo Vincze	Universiteit Gent

Universiteit Gent
Faculteit Ingenieurswetenschappen en Architectuur

Vakgroep Elektronica en Informatiesystemen
Sint-Pietersnieuwstraat 41, B-9000 Gent, België

Tel: +32-9-264.33.66
Fax: +32-9-264.35.94

Dit werk kwam to stand in het kader van een beurs
van het Agentschap voor Innovatie door
Wetenschap en Technologie (IWT)

Dankwoord

Het werk dat voor je ligt is het resultaat van bijna vijf jaar onderzoek. In al die tijd is me vaak de vraag gesteld wat dat *doctoreren* juist inhoudt. “Wat doe jij toch hele dagen?” – “Onderzoek, hé” – “Maar wat is dat dan juist?” – “Wel, euhm, …”. Echt verhelderend was mijn antwoord niet altijd. Sta me dus toe een finale poging te ondernemen. Doctoreren betekent zich vastbijten in een heel specifiek wetenschappelijk domein, zich van daaruit op onontgonnen gebied begeven en beginnen graven, op zoek naar de antwoorden op de originele onderzoeksvraag. Tijdens dat proces komen alsmaar meer vragen naar boven. Je begrijpt, beste lezer, dat het hele proces eens voldoenend, dan weer frustrerend kan zijn, soms beide tegelijkertijd. Maar bovenal is het leerrijk. Een eigen weg zoeken om obstakels waar niemand een pasklare oplossing voor heeft, daar draait het om. Vergis je niet. Een eigen weg zoeken doe je niet alleen. De voorbije vijf jaar zijn verre van een individuele prestatie geweest. Ik heb dankbaar gebruik gemaakt van de ervaring, inzichten en ideëen van de mensen rondom mij. Ik vul de eerste bladzijden van dit proefschrift dan ook graag met het bedanken van enkele personen zonder wie dit werk er nooit gekomen zou zijn.

In de eerste plaats bedank ik mijn promotor, Filip. Voor het geduld en inzicht waarmee je mijn duizend-en-een vragen, groot en klein, hebt benaderd. Voor de variatie aan onderwerpen waarmee je me in contact hebt gebracht. Maar bovenal voor de vrijheid die je me gegeven hebt tijdens die jaren. Kristiaan (tevens promotor), je was, ondanks je soms heel drukke agenda, altijd te bereiken voor een verhelderend gesprek over de ene of andere meting. Bedankt voor het vertrouwen dat ik kreeg, ook wanneer de output wat uitbleef. Filip S., bedankt voor de ijver en deskundigheid waarmee je mijn werk hebt benaderd. Je kritische blik op de zaken heeft veel in de plooi doen vallen. Woesti, merci voor het me bijbrengen van zowat alles dat ietwat praktisch van

aard is; van de finesses van LabVIEW tot het repareren van de opdamper.

Furthermore I wish to thank the members of the examination commission. Their careful reading and critical remarks on the contents of my manuscript definitely helped shape this dissertation to its current form.

Dan zijn er de vele (ex-)collega's, verantwoordelijk voor de werksfeer in op het gelijkvloers van –T. Mensen waar ik altijd naartoe kon om wat stoom af te blazen als er weer eens een meting in duigen viel. Stijn, je spervuur aan vragen en opmerkingen heeft zijn nut bewezen. Zonder ze was een groot deel van hoofdstuk zes nooit gerealiseerd. Caspar, er rust nu een grote verantwoordelijkheid op je, als operator van de setup. Oh, en stuur je me sporadisch nog de highlights van hln.be? Masoumeh and Oksana, I kind of miss the random outbursts of giggling. The office got a lot quieter with you gone... The office next door: Samira, Varsenik (and a bit of Aimi logging in remotely). Thank you for the willingness to listen to my blabber at any moment of the day and for keeping my sugar level up. John, relentless cleanroom addict, thanks for your eager to include other people's processing in your tight schedule. Inge en Michiel, het was een plezier samen met jullie de oefeningen van Elektrische Netwerken te verzorgen. Oliver, er komt een dag waarop zowel de cleanroom als elk lab in het Technicum er perfect bij ligt. Tot dan vertrouw ik erop dat je de mailinglijsten blijft gebruiken ter verbetering van de algehele werkomstandigheden. Glenn, bedankt voor je hulp, zowel op de werkvloer als ernaast. De *éminence grise* van de fyselek: Alex, Patrick en Jeroen (en Marc); jullie waren zeer aangename tafelgenoten. And all the others, for making the hallway such a pleasant place to work: Pieter, Lieven, Frédérique, Manoj, Pavlo, Mohammad, Koen, Stephane, Yi, Wout, Tigran, Tom.

Also a word of thanks to the thesis students I got to supervise: Stijn (zie boven), Steffen (voor het referentiewerk over HOT) and Chetna (whose measurements helped clarify a whole bunch of mysteries).

Voorts wens ik de mensen te danken zonder wie de dagelijkse werking van een onderzoeksgroep volledig zou falen. Bedankt Nadine voor de goeie cleanroomzorgen; Rita, Marnix en Karen voor de hulp bij allerhande administratie en bestellingen; en Ronny en Michiel voor het welfunctioneren van onze IT.

During my time as a PhD-student I had the opportunity to join in on a variety of research topics. Thank you Eva and Laszlo, Elisa and Kevin, Deborah and Jeroen for the fruitful and pleasant collaboration.

Verder wens ik het Agentschap voor Innovatie door Wetenschap en Technologie te bedanken voor de financiële steun die ik ontvangen heb.

Tenslotte zijn er al die mensen die, hoewel ze niet vetrouwd zijn met de technische details van dit werk, er evenzeer toe hebben bijgedragen. Mensen die me even de kleine en grote obstakels deden vergeten en alles wat in perspectief plaatsten. Merci! Als allerlaatste bedank ik het thuisfront. Voor hun niet-aflatende steun, al lang voor dit doctoraat begon.

Dankjewel allemaal!

Toon Brans

Gent, juli 2015

Contents

List of symbols

Symbol	Units	Description
c	$\mathrm{m\,s^{-1}}$	Speed of light in vacuum
c	$\mathrm{mol\,m^{-3}}$	Concentration
c_s	$\mathrm{mol\,m^{-2}}$	Surface concentration
d	m	Distance
D	$\mathrm{m^2\,s^{-1}}$	Diffusion coefficient
e	C	Elementary charge
E	$\mathrm{V\,m^{-1}}$	Electric field
f	Hz	Frequency
f_c	Hz	Corner frequency
F	N	Force
F_T	N	Thermal force
g	$\mathrm{m\,s^{-2}}$	Gravitational acceleration
ΔG	J	Free energy
I	$\mathrm{W\,m^{-2}}$	Intensity
k	-	Integer
k_B	$\mathrm{J\,K^{-1}}$	Boltzmann constant
k_{trap}	$\mathrm{N\,m^{-1}}$	Trapping stiffness
k_{ads}	$\mathrm{m^3\,mol^{-1}\,s^{-1}}$	Adsorption rate constant
k_{des}	$\mathrm{s^{-1}}$	Desorption rate constant
K	$\mathrm{m^3\,mol^{-1}}$	Equilibrium constant
l	m	Length

l_f	m	Focal length
m	kg	Mass
m_mol	kg mol^{-1}	Molecular mass
n	-	Refractive index
n_i	m^{-3}	Concentration of species i
N	mol	Amount of substance
N_A	mol^{-1}	Avogadro's constant
P	W	Power
P_X	$[X]^2$ Hz^{-1}	Discrete power spectral density of X
Pe	-	Péclet number
q	C	Charge
r	m	Radius
S_X	$[X]^2$ Hz^{-1}	Power spectral density of X
t	s	Time
T	K	Temperature
v	m s^{-1}	velocity
V	m^3	Volume
x,y,z	m	Positional coordinate
z_i	-	Valency of a species i
α	F m^2	Polarizability
β	V m^{-1}	Conversion factor
γ	kg s^{-1}	Stokes drag coefficient
ε	F m^{-1}	$\varepsilon_\mathrm{r}\varepsilon_\mathrm{o}$
ε_o	F m^{-1}	Vacuum permittivity
ε_r	-	Relative permittivity
ζ	V	Zeta-potential

η	Pa s	Dynamic viscosity
θ	K^{-1}	Temperature coefficient
κ	m^{-1}	Reciprocal Debye screening length
λ_η	m	Viscous penetration depth
Λ	$[X]^2\ \mathrm{Hz}^{-1}$	
μ_{EO}	$\mathrm{m}^2\ \mathrm{V}^{-1}\ \mathrm{s}^{-1}$	Particle mobility due to electroosmosis
μ_{EP}	$\mathrm{m}^2\ \mathrm{V}^{-1}\ \mathrm{s}^{-1}$	Electrophoretic mobility
ξ	$\mathrm{Hz}^{-1/2}$	Gaussian noise term
ρ_{f}	$\mathrm{C\ m}^{-3}$	Space charge density
ρ_{m}	$\mathrm{kg\ m}^{-3}$	Mass density
σ	$\mathrm{C\ m}^{-2}$	Surface charge density
σ_X	$[X]$	Standard deviation on X
τ	s	Time constant
ϕ	-	Bound fraction of surface sites
Φ	$\mathrm{mol\ m}^{-2}\ \mathrm{s}^{-1}$	Species flux
ψ	V	Electric potential
$\hat{X}$	$[X]$ s	Fourier transform of X
$\wp$	-	Probability

List of abbreviations

CI	Confidence interval
EM-CCD	Electron multiplying charge-coupled device
EOF	Electroosmotic flow
DPBS	Dulbecco's Phosphate-Buffered Saline
LoC	Lab-on-a-Chip
NA	Numerical aperture
NIR	Near-infrared
OTE	Optical trapping electrophoresis
PMMA	Poly(methyl methacrylate)
PTFE	Polytetrafluoroethylene
PVD	Physical vapor deposition
QPD	Quadrant photo diode
RIU	Refractive index unit
RMS	Root mean square
TEM	Transverse electric magnetic
UV	Ultraviolet

Nederlandstalige samenvatting

Het kwantitatief en markeringvrij detecteren van specifieke biomolecules opent de weg naar point-of-caretesten, vroege diagnose van bepaalde ziektes en gepersonaliseerde therapieën die de prognose van patiënten verbeteren. Hierdoor maakt een voortdurende zoektocht naar nieuwe technologieën die gevoelige en specifieke detectie van deze moleculen toelaten, deel uit van de ontwikkeling van nieuwe biosensoren.

Dit proefschrift onderzoekt optische val-gecontroleerde elektroforese (OVE) als nieuwe technologie voor markeringvrije biodetectie. De techniek maakt gebruik van een transparant polymeermicrodeeltje dat chemisch gemodificeerd is zodat het oppervlak plaatsen bevat die een specifieke binding kunnen aangaan met de te detecteren moleculen. Het deeltje is gesuspendeerd in een waterige vloeistof en wordt vastgehouden door een optische val die bestaat uit een sterk gefocuseerde laserbundel die in staat is om het deeltje aan te trekken en vast te houden. Daarenboven wordt het deeltje onderworpen aan een elektrisch wisselstroomveld. Vanwege van zijn oppervlaktelading oscilleert het deeltje in de optische val. Deze oscillatie wordt gekenmerkt door de elektroforetische mobiliteit van het deeltje die de verhouding tussen de deeltjessnelheid en de amplitude van het elektrisch veld weergeeft. Wanneer een biomolecule bindt op het oppervlak van het deeltje verandert dit zowel de oppervlaktelading als de hydrodynamische straal. De elektroforetische mobiliteit is dus een maat voor de hoeveelheid moleculen gebonden aan het deeltje en zodoende voor de concentratie van deze moleculen in de oplossing.

OVE kan een aantrekkelijk alternatief vormen voor andere biodetectietechnologieën om verschillende redenen. Allereerst heeft

onderzoek aangetoond dat deze methode een resolutie fijner dan de elementaire lading kan bereiken in niet-polaire vloeistoffen. Hoewel deze resultaten niet zonder meer bereikt kunnen worden in waterige oplossingen geven ze aan dat gevoelige metingen mogelijk zijn. In de tweede plaats geeft de technologie vrijheid in de keuze van de samenstelling van de gefunctionaliseerde deeltjes. Vermits transparantie en een voldoende hoge brekingsindex de enige vereisten zijn om een deeltje te vangen in de optische val, opent dit de mogelijkheid om een grote hoeveelheid materiaalsystemen aan te wenden. Hierdoor kan de techniek gebruikt worden om verscheidene biomolecules te detecteren. Ten derde zou OVE relatief kleine biomolecules moeten kunnen detecteren, iets waar huidige biodetectietechnologieën onvoldoende in slagen. Tenslotte levert OVE de mogelijkheid om lokaal de concentratie van biologische stoffen te meten en is het zodoende een techniek die haar nut kan bewijzen in fundamenteel celonderzoek.

Een optische val legt de positie van een transparant deeltje vast door een terugwerkende kracht te leveren aan het deeltje van zodra het zijn evenwichtspositie verlaat. De motivering om een optische val te gebruiken in de meetopstelling is drievoudig. In de eerste plaats wordt door middel van deze val de diffusie van deeltjes door Brownse beweging tegengegaan. Hierdoor kan een enkel deeltje gedurende langere tijd gemeten worden. Verder is het precies controleren van de plaats van het deeltje in het meettoestel nodig om de reproduceerbaarheid van de metingen te garanderen. Ten derde geeft het gebruik van een optische val de mogelijkheid om de driedimensionale positie van het deeltje in de val te bepalen met een resolutie kleiner dan een nanometer en aan een meetsnelheid van tientallen kHz. Door middel van vermogenspectrumanalyse van de Brownse fluctuaties die het deeltje doormaakt in de optische val kunnen de krachten uitgeoefend door deze val en het elektrische veld gekalibreerd worden. Hierdoor wordt de gemeten oscillatie van het deeltje in het wisselsstroomveld gerelateerd aan de elektroforetische mobiliteit van het deeltje.

De Brownse beweging van het deeltje in de optische val geeft informatie over de temperatuur van de omgeving van dit deeltje. Dit laat toe om opwarmingsfenomenen in kaart te brengen die voorkomen tijdens een OVE-experiment. Hiervoor worden de Brownse fluctuaties van eenzelfde deeltje eerst gemeten in een omgeving waarvan de temperatuur gekend is. Vervolgens wordt dezelfde meting uitgevoerd in de omgeving waar opwarming plaatsvindt. Door het vergelijken van het vermogenspectrum van beide positiesignalen kan de verandering in viscositeit van het dispergeermiddel berekend worden. Deze viscositeitsverandering geeft aan wat de temperatuursverandering is tussen de twee metingen. Deze methode wordt gebruikt om de effecten van zowel Joule-opwarming als opwarming door de absorptie van laserlicht te meten. Meer algemeen vindt Joule-opwarming plaats in elk microfluidisch toestel dat elektrische velden gebruikt om waterachtige vloeistoffen te manipuleren. Enkel door de temperatuursverhogingen te meten kunnen de gevolgen van die opwarming op de werking van het toestel ingeschat worden. De hierboven besproken meetmethode wordt uitgevoerd op een microfluidisch kanaal waarover een spanning wordt aangelegd. In dit kanaal bevindt zich een zoutoplossing. Door deze meting toe te passen op oplossingen van verschillende ionsterkte kan de precisie en nauwkeurigheid van de methode worden vastgesteld. Deze bedragen 0.9 K en 15%, respectievelijk. Ook wordt aangetoond dat de meting van tijdsafhankelijke opwarmingseffecten met een tijdsresolutie van 1 s mogelijk is met deze methode. Verder wordt de opwarming door absorptie van laserlicht bekeken. Hiervoor wordt de Brownse beweging van een deeltje geobserveerd bij verschillende vermogens van de inkomende laser. Hieruit blijkt dat de temperatuursverhoging door de absorptie van laserlicht kleiner blijft dan 5 K.

Het voorkomen van elektro-osmotische stroom (EOS) zorgt ook voor moeilijkheden bij het uitvoeren van een OVE-experiment. Doordat de wanden van een microfluidisch kanaal geladen zijn, vormt er zich een wolk van mobiele tegenladingen in hun nabijheid. Wanneer een extern elektrisch veld wordt aangelegd in het kanaal bewegen die ionen en trekken hierbij de omliggende vloeistof mee, waardoor de

EOS ontstaat. Door de microfluidische substraten te benaderen als twee parallelle platen kan een analytische uitdrukking gevonden worden voor de EOS in deze kanaaltjes. Hieruit volgt dat EOS die ontstaat door een wisselveld sterk beïnvloed wordt door de aangelegde frequentie van het veld en de positie in het microfluidisch kanaal. In een OVE-experiment is EOS harmonisch met dezelfde frequentie als het aangelegde veld. Dit bemoeilijkt de meting van de elektroforetische mobiliteit van een deeltje. Om alsnog juiste mobiliteitsmetingen te verkrijgen in een OVE-experiment werd een calibratieprocedure ontwikkeld die in staat is de EOS in het kanaal in kaart te brengen. Hierbij wordt de oscillatie van eenzelfde deeltje bestudeerd bij verschillende aangelegde frequenties en op verschillende locaties in het microfluidische kanaal. Elke variatie in de oscillatie is te wijten aan EOS. Door deze variaties te vergelijken met het analytisch model kan het effect van EOS uit de meting verwijderd worden.

Voor de biodetectie-experimenten worden gebiotinyleerde polystyreendeeltjes gebruikt om de concentratie van avidine in een bufferoplossing te bepalen. Avidine is een glycoproteïne die erom gekend staat specifiek en uitzonderlijk sterk te binden met biotine. Dit maakt het avidine-biotine systeem een modelsysteem dat veelvuldig gebruikt wordt om nieuwe biodetectietechnologieën uit te testen. In een eerste type experimenten worden verschillende mengsels die eenzelfde hoeveelheid deeltjes maar een verschillende hoeveelheid avidine bevatten gebruikt. Uit deze metingen volgt de bindingskarakteristiek van het biosysteem. Er worden twee adsorptiemechanismes vastgesteld. Een eerste is enkel zichtbaar bij gebiotinyleerde deeltjes en doet zich voor bij lage avidineconcentraties (<0.04 μg/ml). Deze adsorptie is een resultaat van de specifieke binding van avidine met de biotinelaag op het deeltje. Het tweede mechanisme wordt vastgesteld bij beide deeltjes aan hogere avidineconcentraties (>1 μg/ml) en is een gevolg van de niet-specifieke interactie van avidine met het oppervlak van de deeltjes. Deze twee mechanismes worden opgenomen in een theoretisch model dat de relatie tussen de gemeten mobiliteit en de avidineconcentratie in het mengsel beschrijft. Dit

model blijkt de mobiliteit van de deeltjes over vier grootte-ordes van avidineconcentratie goed te karakteriseren. In een tweede type experiment wordt een microfluïdisch kanaal gebruikt dat bestaat uit een Y-splitsing met twee ingangen en een uitgang. In elke ingang wordt een mengsel met verschillende avidineconcentratie gespoten. Door het laminaire vloeistofprofiel in het kanaal blijven die twee stromen gescheiden in het uitgangskanaal. Een deeltje wordt met behulp van de optische val van de ene vloeistofstroom naar de andere gebracht. Dit laat tijdsafhankelijke kwantitatieve metingen van de avidineadsorptie en –desorptie toe.

In dit proefschrift werd aangetoond dat OVE inderdaad gebruikt kan worden voor detectie van specifieke biomolecules. Er werd aandacht besteed aan de calibratie voor zowel opwarmingseffecten als EOS. Verder werd de meettechniek uitgetest op een modelsysteem. Verdere ontwikkelingen van de technologie bevinden zich enerzijds in het onderzoeken van biologisch relevantere molecules en anderzijds in de miniaturisatie van de experimentele opstelling, waardoor het gebruik ervan vergemakkelijkt wordt.

English summary

Quantitative and label-free detection of specific biomolecules holds promise for point-of-care testing, early diagnosis of certain diseases and personalized therapy, which improves the patient's prognosis. An ongoing search for new technologies enabling sensitive and specific detection of a target analyte makes up a considerable part of the development of new biosensor devices.

This dissertation explores optical trapping electrophoresis (OTE) as a novel technology for label-free biosensing. The technique uses a transparent polymer microparticle that is chemically modified such that its surface contains sites to which the target analyte can bind specifically. The particle is suspended in an aqueous solution and held by optical tweezers, i.e. a tightly focused laser beam that attracts and traps the particle. Additionally an AC electric field is applied externally, which makes the particle oscillate inside the optical trap. The oscillation is characterized by the electrophoretic mobility, a measureable quantity defined as the ratio between the particle velocity and the electric field amplitude. When the target analyte adsorbs on the particle, parameters such as the particle surface charge and hydrodynamic radius change, which has an influence on the oscillation of the particle. The particle mobility is therefore a measure for the amount of target molecules bound on the particle, and thus for the concentration of analyte present in the solution.

There are a number of arguments that make OTE potentially attractive as a technology for biosensing. Firstly, results in literature have shown charge measurements in nonpolar media with a precision of the elementary charge. Although these results are not straightforwardly reproduced in aqueous solutions, they indicate a potential for highly

sensitive measurements. Secondly, the technology is flexible regarding the composition of the functionalized particles. To achieve optical trapping, the only requirement for the particles is that they are transparent and have a refractive index higher than the continuous medium. This allows for a considerable number of material systems that can be employed to achieve the specific binding with the target molecules. Thirdly, in contrast to most other biosensing technologies, OTE does not require targets of high molecular weight, provided they are sufficiently charged. OTE could therefore offer quantitative detection of certain biomolecules which other biosensing technologies can measure insufficiently. Lastly, the principle of localized concentration measurements of biological agents could be applied in e.g. fundamental cell research.

Optical tweezers fix the position of a transparent particle by providing a Hookean restoring force to the particle when the latter displaces from the equilibrium position. The motivation for the use of optical tweezers in the measurement setup is threefold. Firstly, it counters particle diffusion due to Brownian motion, hence enabling long duration measurements on the same particle. Secondly, optical tweezers allow for accurate positioning of the particle inside the measurement device, which increases the reproducibility of the measurements. Thirdly, by using optical tweezers the particle position can be detected using back focal plane interferometry. This allows to monitor the three-dimensional particle position at a resolution of less than 1 nm and an acquisition rate of 100 kHz. A calibration of the forces inside the optical tweezers is done by power spectrum analysis of the Brownian fluctuations of the particle inside the trap. From this calibration the observed oscillation of the particle in the applied AC electric field can directly be transformed into a value for the electrophoretic mobility.

Furthermore, the Brownian motion of the particle reveals information about the temperature of the medium surrounding the particle. This allows to measure heating effects taking place during an OTE-experiment. To attain these temperature measurements, the Brownian

fluctuations of a single particle are measured first at a known reference temperature and then in the situation where heating effects occur. Through power spectrum analysis of both position signals, the temperature-induced change in viscosity of the continuous medium is established, from which a value for the temperature increase is calculated. Using this method the consequences of both Joule heating and laser-induced heating are examined. Joule heating occurs, more generally, in microfluidic applications that use electric field to manipulate aqueous liquids. Knowledge of these heating effects is crucial to understand their implications on the performance of the device. By performing the previously explained temperature measurements in a microfluidic device containing solutions with different salt concentrations, it is established that the measurement method has a precision of 0.9 K and an accuracy of 15%. Transient heating effects can be monitored as well at a time resolution of approximately 1 s. Furthermore, heating due to absorption of laser light is considered. For this the Brownian fluctuations of the particle are examined at different laser powers. This reveals that the temperature increase due to laser-induced heating is less than 5 K.

An additional complication arising when performing OTE experiments is the appearance of electroosmotic flow (EOF). Because the walls of the microfluidic device are charged, a cloud of mobile counterions forms around them. When applying an electric field, these mobile charges drift and drag along the surrounding fluid, creating EOF. By approximating the used microfluidic devices as parallel plates, an analytical expression for the EOF is derived. This expression shows that the AC-induced EOF amplitude and phase with respect to the electric field depend both on the applied frequency and the position inside the channel. In an OTE experiment, the EOF is harmonic at the same frequency as the applied electric field and thus compromises the mobility measurement of the particle. To allow for accurate mobility measurements with OTE, a calibration method for electroosmotic flow is developed. In this calibration procedure the field-induced oscillation of a single particle is observed at different applied frequencies and different positions inside the microchannel. Any

frequency or position dependent variation in e.g. oscillation amplitude is caused by EOF. By fitting the measured change in mobility to the analytical model describing EOF, a mapping of this flow inside the device is obtained.

The biodetection experiments use biotinylated polystyrene particles to determine the concentration of avidin inside a buffer solution. Avidin is a glycoprotein that is known to bind specifically and exceptionally strongly to biotin. This makes the avidin-biotin system a model system that is often employed to characterize emerging biosensor technologies. In a first type of experiment different mixtures containing a fixed amount of these particles and various avidin concentrations are considered. This allows to determine the steady-state binding characteristics. The same experiment is performed with non-functionalized polystyrene particles. Based on these measurements, two adsorption mechanisms can be identified. The biotinylated particles show specific adsorption, resulting from the binding of avidin molecules with biotin, at low avidin concentrations (below 0.04 μg/ml) while at concentrations of several μg/ml non-specific binding on both type of particles is observed. These two adsorption mechanisms are incorporated in a theoretical model describing the relation between the measured mobility and the avidin concentration in the mixture. This model describes the electrophoretic mobility of these particles accurately for avidin concentrations over four orders of magnitude. In a second type of experiment, a dedicated microfluidic device is used to monitor the dynamic change in particle mobility. The device consists of a Y-junction having two inlets and one outlet and a different avidin concentration is chosen at each inlet. The laminar flow profile inside this device makes that the two liquids in the outlet channel remain separated. A particle is brought from one buffer solution to another by moving it across the boundary between the two liquids. This allows the real-time quantitative monitoring of avidin adsorption onto and desorption from the particle.

From the work described in this dissertation it can be concluded that OTE is indeed an alternative biosensing technology. The work focused firstly on calibration of heating phenomena and EOF occurring during a measurement. Furthermore, the biosensing technique was tested on a model biological system. Further developments would consist in, on the one hand, applying this method on a biologically more relevant biodetection system and, on the other hand, the miniaturization of the experimental setup, which would greatly simplify its operation.

Chapter 1
Background and outline

1.1 Introduction

This dissertation aims at employing optical trapping electrophoresis (OTE) as a measurement technique for biosensing. This introductory chapter provides, concisely, the rationale and general working principle of biosensors. The measurement technique OTE is introduced in a non-technical fashion, together with an overview of results in literature that have employed this technique. Also the motivation behind using this technique as a new biosensor technology is discussed. The chapter concludes with a statement of the objectives of this work and the outline of the following chapters.

1.2 Biosensors

Biosensors are devices built to quantitatively detect a specific biological agent, such as a protein or a pathogen, in a fluid, e.g. blood or saliva [1]. They have become indispensable in modern healthcare practice: ever since their introduction in the early 1960s, biosensors have steadily found their way to the consumer market [2]. The best known application of the technology is, probably, the glucose sensor, which makes up for 85% of the biosensor market nowadays [3]. This portable device, typically not larger than a keychain, allows to accurately determine the sugar level in blood while consuming only a single drop of it. Its invention has proved to be a landmark for patients suffering from diabetes, one of the major causes of death and disability throughout the world: it has lead to a tremendous increase in life expectancy and comfort for those patients.

Most sensitive biosensor technologies today follow a labeling procedure: a fluorescent, magnetic or radioactive marker is bound onto the target analyte and the signal produced by this label is detected [4]. These methods allow for very sensitive detection, on the level of single molecules [5]. Despite this clear asset, there are intrinsic problems associated with label-based detection methods. Firstly, quantitative measurements are difficult to attain with these measurement methods since the number of labels on a single molecule is often difficult to control. Also time-dependent

measurements revealing binding kinetics of the analyte are impossible [6]. Moreover, the attachment of the label can interfere with the analyte and affect its chemical properties such that its function is compromised [7]. Lastly, the labeling procedure is often time-intensive and costly, making these technologies only available in specialized environments [8]. These issues have lead to an increasing interest in label-free biodetection methods.

In its very essence, a label-free biosensor consists of a few standard elements, as is schematically represented in Figure 1-1. The detection of a target analyte happens typically by a specific binding of this agent onto a recognition layer. This recognition layer consists of molecules that show a high affinity for the target. A binding event causes a change in a physical parameter, e.g. the refractive index, electrical impedance or dielectric permittivity, of the substrate. A transducer converts this change into a measurable signal that is then processed by appropriate electronics. The exact working principle of the transducer depends on the technology used. For example, in the case of optical biosensors, often a shift in resonance wavelength resulting from a changing refractive index is monitored [9].

Label-free biosensor technologies hold the promise to deliver point-of-care (PoC) diagnostics, bringing elaborate medical tests to a patient's home or a local health care center without the need for an extensive laboratory infrastructure and highly trained personnel to operate it. In doing so, PoC enables monitoring a patient's progress and allows for personalized therapies by the monitoring of disease-specific biomarkers [10], [11]. Moreover, these technologies aim for the early detection of e.g. cardiovascular diseases and cancer, typical examples in which a rapid diagnosis improves the patient's prognosis considerably [12], [13]. Aside from medical applications, biosensors find their use in the pharmaceutical industry, where they are used to discover and develop new drugs [14], [15]. Also, technologies directed towards pathogen detection deliver solutions for food safety, water quality monitoring and epidemic control [16], [17].

Development of new label-free methods is typically a highly interdisciplinary task and entails numerous facets to be addressed. Firstly, the discovery of potentially interesting biomarkers and the development of recognition layers increase the potential use of these technologies for diagnostics [18], [19]. Additionally, novel transducer technologies are being developed to meet the sensitivity required to achieve biomarker detection of biological importance [20]. These technologies should deliver biosensors that provide a reliable and fast read-out while consuming only little of the reagents involved and, above all, do this in an inexpensive way [21]. These requirements have resulted in a trend towards gathering of the functionalities of a biosensor, e.g. sample injection and transport, biochemical detection, read-out, etc., by integrating sensors, actuators and electronics for signal processing onto a single device [22]. These so-called Lab-on-a-Chip (LoC) devices allow for a straightforward parallelization of and automated control over several detection processes, which adds to their ease-of-use.

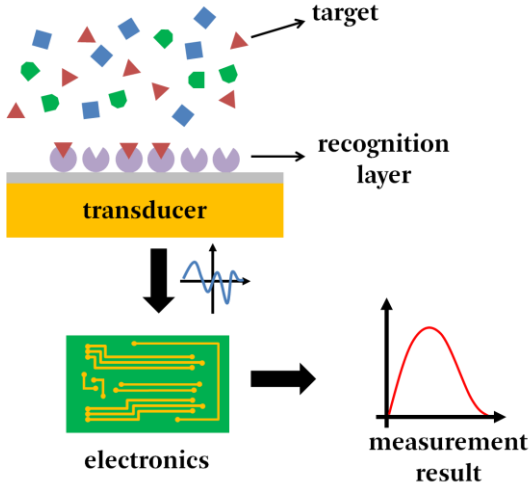

Figure 1-1: Schematic representation of the most important components and the working principle of a biosensor.

1.3 Optical trapping electrophoresis

Optical trapping electrophoresis (OTE) is a novel technique to characterize the electrokinetic properties of a single microparticle suspended in a liquid. The working principle is introduced here (Figure 1-2) and will be elaborated on further in the following chapters. In essence, three major components constitute an OTE-setup:

1. Optical tweezers are created by tightly focusing a laser beam with a high numerical aperture objective. Under the right conditions, a single transparent particle is attracted towards this focus and trapped there.
2. An externally applied sinusoidal electric field causes the trapped particle to oscillate inside the tweezers. The oscillation amplitude depends, among others, on the electrokinetic properties of the particle.
3. With the particle's average position fixed by the optical tweezers, a dedicated detection system to record the particle position is established. It allows recording the particle's three-dimensional position at frame rates in the order of 100 kHz.

From the measured oscillation, the electrokinetic properties of the particle can be derived in a time resolved fashion. More specifically, an OTE experiment measures the electrophoretic mobility of a particle. This property is defined as the ratio between the electric-field-induced velocity of the particle to the electric field amplitude. The value of the electrophoretic mobility depends on a number of parameters, including the surface charge and hydrodynamic radius of the particle and the ionic strength of the continuous medium. The influence of these parameters on the mobility will be discussed in later chapters.

The literature on research performed with this technique is fairly sparse and an overview is given in this paragraph. Foremost the technique has been used to investigate and characterize processes inside colloidal suspensions. Because the electrophoretic mobility of a single particle is measured, OTE offers a way to probe electrokinetic properties of colloids at very low particle volume fractions, an

experimental condition that cannot be examined with other, conventional, methods. This has on the one hand opened the way for research on a fundamental level by which theories from colloid science can be assessed. Palberg and coworkers have used OTE to examine the electrophoretic mobility of microspheres suspended in deionised water at various volume fractions [23]. They found that the electrokinetic behavior of these microspheres shows an unexpected dependency on this volume fraction, a relationship which is unexplained by present theory. The same authors furthermore established in a different study that the electrophoretic mobility of a particle appears independent of its size [24]. Semenov *et al.* have used the technique to, for the first time, observe charge inversion on a single colloidal particle: when suspended in an electrolyte containing ions of high valency, a charged particle can show a reversed mobility as compared to when it is surrounded by low valency ions. Also this effect is largely unexplained by the standard electrokinetic model, but the authors present molecular dynamics simulations to quantitatively explain their experimental results. Furthermore, the understanding of charging mechanisms of colloidal dispersions in nonpolar media has seen a considerable improvement from the use of OTE, where it has delivered charge measurements with previously unseen sensitivity. Roberts and coworkers established an uncertainty of 0.25 electron charges on the measurement of the average charge of a single microparticle in dodecane [25]. Beunis *et al.* have further developed the measurement setup and managed to detect single electron charging events [26]. This opens the way to characterize charging events of dispersions in nonpolar media. The understanding of electrical effects in these systems plays an important role in applications as electronic inks [27]. In nonpolar media with added surfactant, OTE has been used to measure the electrophoretic retardation force, which originates from the friction between the particle and ions adjacent to the particle [28].

Aside from these rather fundamental results, OTE has given insight into certain (bio)chemical processes. Galneder and coworkers have used the technique to investigate the activity of the enzymes that

modify the charge of phospholipid bilayers [29], [30]. They have prepared a silica bead on which a phospholipid bilayer containing phosphatidylinositol 4,5-bisphosphate (PIP2) was coated. PIP2 hydrolyses as a result of the well-characterized enzyme phosphoinositide-specific phospholipase C-δ1 (PLC-δ). As a result of this hydrolysis reaction, the charge of the lipid bilayer changes and OTE enabled a time-resolved measurement of this varying charge, effectively characterizing the enzymatic activity of PLC-δ. A final study in which the combination of a laser trap and electrophoresis is used is by van Heiningen *et al.* They have studied the kinetics of poly(ethylene oxide) adsorption onto and desorption from a silica microsphere [31], [32].

1.3.1 Optical trapping electrophoresis as a biosensor

This dissertation aims at developing OTE as a biosensor technology. For this, functionalized particles are used as transducers. Their surface is chemically modified with a recognition layer that enables specific binding with the target analyte, which is present in the buffer solution. One particle is optically trapped and analyzed by an AC electrophoresis experiment. When the target analyte adsorbs onto this particle, this is reflected in the measured mobility: this can, for example, be due to a change in surface charge of the particle resulting from the nonzero charge of the adsorbed analyte or because of hydrodynamic screening when the analyte is partially permeable for the buffer solution. This makes the mobility a measure for the amount of adsorbed analyte on the particle and hence the concentration of the species in the buffer.

The use of OTE as a label-free biosensor is untried but could potentially provide several advantages. Firstly, the aforementioned sensitivity of a single elementary charge obtained in nonpolar media makes for an attractive asset of this method. One should immediately note, though, that this sensitivity is unlikely to be reached effortlessly in aqueous solutions: the presence of ionic species in these liquids causes screening of the surface charge of a particle and limits the field strength that can be attained during a measurement. Secondly, OTE uses functionalized particles to achieve specific binding with the target

analyte. Since these particles are only required to be transparent and have a refractive index higher than the continuous medium in order to be trapped, there is no restriction regarding their composition. This makes that a large amount of material systems making up for different detection capabilities can be implemented with little effort. Moreover, using particles as a substrate on which the binding occurs makes that the overall device can be made reusable, which is often not the case with other biosensor technologies [1]. Lastly, OTE could provide quantitative measurements of agents of low molecular weight. Most other biosensing technologies require a significant overlap between the biomolecule and the physical signal generated by the transducer, e.g. an optical field. This makes them inapt for sensitive measurements of small molecules [4]. OTE could potentially measure the presence of small, charged molecules which are currently not detectable by other biosensors.

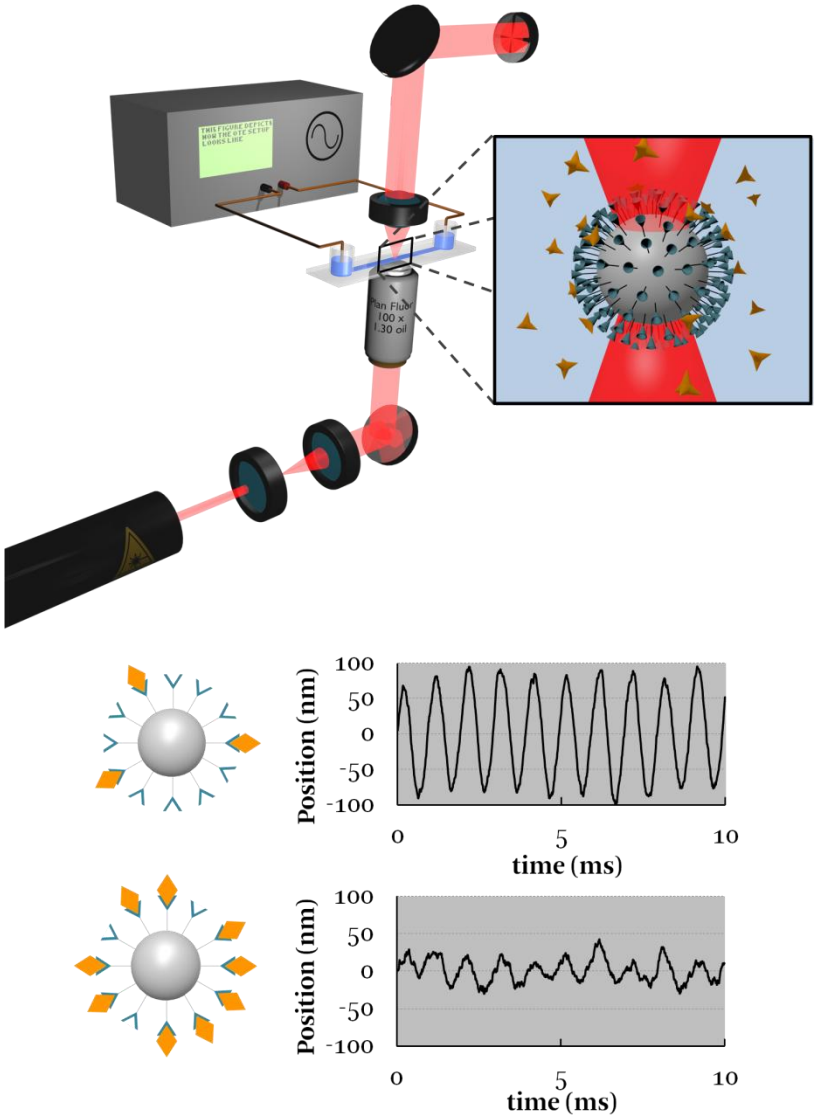

Figure 1-2: Schematic representation of the optical trapping electrophoresis setup for biosensing applications. A functionalized particle is trapped by a tightly focused laser beam and subjected to an AC electric field. Its position is monitored by a dedicated detection system. The particles used in this dissertation are negatively charged and oscillate as a result of the external field. When the target analyte, which in this case is positively charged, binds to the particle, the oscillation amplitude decreases and this is a measure for the amount of analyte in the buffer.

1.4 Outline of the text

Chapter 2 highlights the basic concepts from colloid science that are necessary to adequately describe the movement of a colloidal particle in an electric field.

Chapter 3 consists of two major sections. The first section introduces optical tweezers and provides the reader with the necessary background about their working principle. This section also discusses how the positional data obtained from an OTE measurement is analyzed and the particle mobility is retrieved. The second section presents the practical implementation of these concepts. It gives an elaborate overview of the optical setup that I built and used for the work in this dissertation. Also the used measurement cells and fluid handling technology are discussed.

Chapter 4 discusses the heating effects taking place in a typical OTE experiments. In this chapter, I introduce a measurement method based on the analysis of the Brownian motion of an optically trapped particle to characterize both Joule heating due to the application of the electric field and heating due to laser absorption.

Chapter 5 covers the effect of electric-field-induced flow on an OTE-experiment. After providing an expression for this flow inside the used measurement cells, I discuss how it disturbs the mobility measurements and propose a technique to handle this complication. I assess the performance of this technique in an experiment which can be linked to the theory covered in previous chapters.

Chapter 6 reports on biosensing experiments performed with OTE. I measure the concentration of avidin by monitoring the mobility of a biotinylated particle. By performing two types of experiments, I establish a model which describes the adsorption of avidin on these particles.

Chapter 7 bundles the main conclusions drawn in the previous chapters and presents perspectives for future research.

Chapter 2
Colloids

2.1 Introduction

Colloidal systems are found abundantly in nature and in industrial applications. We encounter them daily under the form of paints, cosmetics, pharmaceuticals, alimentary products etc. In general, colloids are multiphase system in which at least one discrete phase is dispersed in a continuous medium. They differ from a true solution in the fact that the size of the dispersed phase constituents, which are termed particles, exceeds the size of the molecules in the dispersing medium by at least one order of magnitude. In practice this means that the discrete phase is built out of particles with a size ranging from 1 nm to 10 μm in at least one dimension.

A proper characterization of a colloid draws upon several theories from physics, chemistry and biology. Colloid science is a highly interdisciplinary field aimed at fully understanding the behavior of any colloidal system both in a fundamentally theoretical way and via empirical studies. To get a grasp at why such an exhaustive treatment is necessary I point out that particles inside a colloid exhibit a large surface-to-volume ratio. Hence the physical and chemical properties of a colloid are not solely determined by the bulk properties of the materials making up de dispersed and continuous phase. Surface phenomena, i.e. effects taking place at the interface between two phases and which are typically not considered in other branches of science, are far from negligible: molecules close to a surface behave differently than those in bulk and determine the behavior of the system significantly.

In this chapter I describe the behavior of a single particle inside a colloid. I do not intend to provide an all-encompassing introduction to the subject of colloid science; rather this chapter highlights some topics which will be relied on in later chapters. For a more exhaustive treatment of these subjects I refer the interested reader to standard textbooks in the field, on which much of the material in this chapter is based [33]–[37].

2.2 Kinetic properties of colloidal particles

The movement of a particle inside a dispersion results from both macroscopic forces and microscopic, statistical forces. Three fundamental forces can be distinguished. Firstly the mass density of the particle relative to the continuous medium determines the balance between gravity and buoyancy, resulting in a net force on the particle causing sedimentation of the particles. This sedimentation force is written as:

$$F_{\text{sed}} = \left(\rho_{\text{m,part}} - \rho_{\text{m,liq}}\right) V_{\text{part}}\, g\,, \tag{2.1}$$

with $\rho_{\text{m,part}}$ and $\rho_{\text{m,liq}}$ the particle and continuous medium mass density, respectively, V_{part} the volume of the particle and g the gravitational acceleration.

The other two fundamental forces, i.e. the viscous drag force and the thermal force, are discussed more comprehensively in the remainder of this section.

2.2.1 Viscous drag force

A spherical particle moving inside a liquid with a certain velocity v experiences a resistance of the fluid accounting for the viscous drag force. In the case of laminar flow, this drag force is proportional to the instantaneous velocity of the particle and the proportionality factor γ is termed the drag coefficient:

$$F_{\text{drag}} = -\gamma v\,. \tag{2.2}$$

The value of γ is determined by properties of both the fluid, such as its dynamic viscosity η, and the particle, e.g. its radius. Stokes has derived the drag coefficient of a perfect sphere of radius r moving inside an incompressible fluid; an expression known as Stokes' law [38]:

$$\gamma_0 = 6\pi\eta r \,. \tag{2.3}$$

This relation holds only when the medium can be considered as a continuous medium. For small particles, such as macromolecules, or particles with a non-spherical shape Stokes' law can still apply by defining a drag coefficient based on an arbitrary hydrodynamic radius. This radius does not necessarily correlate with the physical dimensions of the particle.

The derivation of equation (2.3) assumes that the particle moves at a constant velocity with respect to the fluid at infinity. Stokes has also derived an expression for the drag coefficient when a spherical particle undergoes harmonic motion with respect to a liquid [38], [39]. This provides an expression for the Stokes coefficient in the frequency domain:

$$\gamma(f) = \gamma_0 \left(1 + (1-\mathrm{i})\sqrt{\frac{f}{f_\eta}} - \mathrm{i}\frac{2f}{9f_\eta} \right) \,, \qquad f_\eta = \frac{\eta}{\pi r^2} \,. \tag{2.4}$$

In this relation f_η is a transition frequency which is of the order of 1 MHz for the particles considered in this thesis. This makes the error of the absolute value of $\gamma(f)$ compared to equation (2.3) less than 5 % for frequencies around 1000 Hz.

Lastly, Stokes' law presumes the liquid medium in which the particle is suspended to extend towards infinity. The presence of container walls near the particle influences the hydrodynamics around the particle and thus the expression for the drag coefficient. In this thesis particle movements parallel to a substrate are considered. Faxén derived a correction factor for the drag coefficient of a spherical particle with radius r with its center separated from a planar substrate by a distance l [40]:

$$\gamma = \frac{\gamma_0}{1 - \frac{9}{16}\frac{r}{l} + \frac{1}{8}\left(\frac{r}{l}\right)^3 - \frac{45}{256}\left(\frac{r}{l}\right)^4 - \frac{1}{16}\left(\frac{r}{l}\right)^5 + \ldots}. \quad (2.5)$$

From this, one calculates the corrected drag coefficient differs from Stokes' law by less than 6 % for $l > 10r$. Figure 2-1 provides a graphical representation of the above equation.

2.2.2 Brownian motion

The equipartition theorem states that the molecules constituting a liquid at temperature $T > 0$ K have an average kinetic energy $k_B T/2$ per degree of freedom. When a particle is suspended in this liquid, part of these molecules collide with and cause a momentum transfer to the particle. Because both the density and the individual speed of the colliding molecules fluctuate, the particle experiences an instantaneous fluctuating net force making the particle move in a random pattern, the so-called Brownian motion.

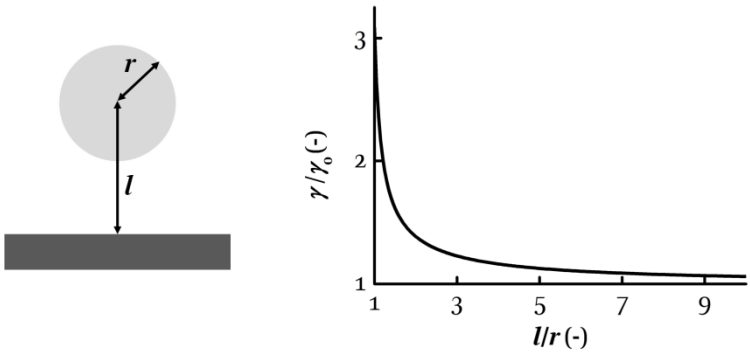

Figure 2-1: Visualization of Faxén's law. When a spherical particle approaches a planar substrate, hydrodynamic coupling makes that its drag coefficient increases compared to the drag coefficient in bulk, given by Stokes' law (equation (2.3)). The drag coefficient considered by Faxén's law is associated to a movement parallel to the substrate.

The movement of a particle driven by the thermal force is well described by the Einstein-Ornstein-Uhlenbeck formalism of Brownian motion [39], [41], [42]. The (one-dimensional) position x of a particle is described by the Langevin equation, relating the acceleration of the particle with the viscous drag force and the thermal force $F_T(t)$:

$$m\frac{\mathrm{d}v}{\mathrm{d}t} = -\gamma v + F_T(t), \quad v = \frac{\mathrm{d}x}{\mathrm{d}t}. \tag{2.6}$$

Due to the large number of molecules interacting with the particle, an explicit expression of the thermal force in which all these molecules are incorporated is impossible to attain. However, statistical properties of $F_T(t)$ can be specified based on physical assumptions [43], [44]. A first assumption involves symmetry of the thermal force. When considering a statistical ensemble, the average force over this ensemble equals zero, i.e. the force is symmetric:

$$\langle F_T(t) \rangle = 0. \tag{2.7}$$

The second assumption states that, in thermodynamic equilibrium, the correlation between the thermal forces at two different times t and t' solely depends on the time difference $t - t'$. The characteristic time scale at which this correlation occurs is in the order of the average time between two collisions and is calculated from the equipartition theorem to be typically in the order of 10^{-13} s. At time scales much larger than this characteristic time the autocorrelation of $F_T(t)$ can be summarized as

$$\langle F_T(t) F_T(t+\tau) \rangle = a\delta(\tau), \tag{2.8}$$

with $\delta(t)$ the Dirac delta distribution. To calculate the constant a, the Wiener-Khinchin theorem can be used. This theorem states that the autocorrelation function of a random process and the power spectral density of this process are Fourier pairs. It is defined as

$$P_x(f) = \lim_{t_{\mathrm{msr}} \to \infty} \frac{\left\langle \left| \hat{x}_t(f) \right|^2 \right\rangle}{t_{\mathrm{msr}}}, \tag{2.9}$$

with f ranging from $-\infty$ to $+\infty$ and $\hat{x}_t(f)$ the Fourier transform of the signal $x(t)$ measured over a time interval $\left[-t_{\mathrm{msr}}/2, t_{\mathrm{msr}}/2\right]$:

$$\hat{x}_t(f) = \int_{-t_{\mathrm{msr}}/2}^{t_{\mathrm{msr}}/2} x(t) \exp(-2\pi i f t) \mathrm{d}t \,. \tag{2.10}$$

The power spectral density of F_{T} thus reads

$$P_{F_{\mathrm{T}}}(f) = a \,. \tag{2.11}$$

From the preceding it follows that F_{T} has the characteristics of white noise.

The Fourier transform of the Langevin equation (2.6) provides a relation between the spectral densities of the particle velocity and the thermal force:

$$P_v(f) = \frac{P_{F_{\mathrm{T}}}(f)}{4\pi^2 f^2 m^2 + \gamma^2} \,. \tag{2.12}$$

From this expression the autocorrelation function of the velocity is retrieved by again applying the Wiener-Khinchin theorem:

$$\left\langle v(t) v(t+\tau) \right\rangle = \frac{a}{2m\gamma} \exp\left(-\frac{\gamma}{m} \tau \right). \tag{2.13}$$

The variance on the velocity is obtained by setting $\tau = 0$. From this value the average kinetic energy can be calculated. The equipartition theorem equates this kinetic energy to the thermal energy and allows retrieving a value of a. One finds

$$a = 2k_B T\gamma \,. \tag{2.14}$$

Furthermore, as F_T is the resultant of a large number of collisions which can be seen as identically distributed random forces, it is generally assumed to be a Gaussian process on account of the central limit theorem. This provides an expression for the thermal force:

$$F_T(t) = \sqrt{2k_B T\gamma}\,\xi(t)\,, \tag{2.15}$$

where $\xi(t)$ is a random Gaussian process with normalized amplitude and a white noise power spectral density. In the case of vanishing particle mass the Langevin equation reduces to

$$\gamma\frac{\mathrm{d}x}{\mathrm{d}t} = \sqrt{2k_B T\gamma}\,\xi(t)\,, \tag{2.16}$$

giving the Einstein description for Brownian motion. Integration of this equation over a time interval $[0,t]$ provides the distance over which the particle has moved:

$$x(t) = x(0) + \sqrt{\frac{2k_B T}{\gamma}}\int_0^t \xi(t')\mathrm{d}t' \,. \tag{2.17}$$

From this equation the expected variance on the position of the particle is easily calculated:

$$\left\langle \left(x(t) - x(0)\right)^2 \right\rangle = \frac{2k_B T}{\gamma}t\,, \tag{2.18}$$

where in the last step the property $\langle \xi(t')\xi(t'')\rangle = \delta(t''-t')$ was used. This expression for the variance of the position leads to the Einstein-Smoluchowski relation for the diffusion coefficient of the particle:

$$D = \frac{k_B T}{\gamma} \,. \tag{2.19}$$

2.3 Particle charging and electrical double layer

Particles suspended in a polar continuous medium often carry a net charge. The origin of this charge depends both on the surface properties of the particle and the characteristics of the dispersing medium. Several mechanisms exist by which a colloidal particle can acquire a net charge. One of these mechanisms is by ionization of a surface group present on the particle. This charging mechanism is often encountered with polymeric particles and generally involves a protonation or deprotonation process. In this case the number of ionized groups depends strongly on the pH of the dispersing medium. For example, particles having a carboxylic end group can carry a negative charge due to deprotonation of this end group: $-\mathrm{COOH} \rightarrow -\mathrm{COO}^- + \mathrm{H}^+$. This deprotonation reaction is affected by the pH of the continuous medium. When this pH exceeds the pK_a of this group by far, all carboxylic end groups are deprotonated. At a pH much lower than this pK_a, the group will not dissociate and the particle will not accumulate any surface charge from the above reaction. For a lot of dispersions there exists a certain pH value at which the net charge of the colloidal particles is zero, either because no surface groups are charged or because differently charged end groups compensate each other. This is called the point of zero charge of the dispersion.

When suspended in an electrolyte solution, the charged surface of a colloidal particle attracts ions with opposite polarity, i.e. counterions, and repels ions with the same polarity, named coions. The combined accumulation of counterions and depletion of coions near the surface together with the surface charge on the colloidal particle is termed the electrical double layer. It is important to note that the distribution of counterions cannot be modeled as a monomolecular layer around the particle surface since the charge accumulation of free counterions is balanced by repulsion between ions of the same polarity and diffusion due to the concentration gradients being formed. This makes that in

equilibrium a certain distribution of co- and counterions will be reached in the vicinity of the charged surface of a colloidal particle.

One fairly basic approach to describe the electrical double layer is to take into account only electrostatic interactions between the free charges present inside the double layer. The equilibrium distribution of ions near the interface is established from the Boltzmann distribution law. The latter provides the probability $\wp$ of finding an ion with free energy ΔG:

$$\wp \propto \exp\left(-\frac{\Delta G}{k_{\mathrm{B}}T}\right), \tag{2.20}$$

where k_{B}=1.38×10^{-23} J K^{-1} is the Boltzmann constant and T gives the absolute temperature. The free energy ΔG corresponds with the work necessary to move an ion of species i with valency z_i from infinity to a place in space with a certain, in this model electrostatic, potential ψ determined by the charged particle and other ions, i.e. $\Delta G = z_i e \psi$. The concentration of ions of species i can thus be written as

$$n_i = n_{i,\infty}\exp\left(-\frac{z_i e \psi}{k_{\mathrm{B}}T}\right), \tag{2.21}$$

where $n_{i,\infty}$ represents the bulk concentration of that species. The electric potential ψ is chosen to be zero far away from the particle surface. Poisson's equation is used to provide an expression for the ion distribution as a function of a spatial coordinate instead of the electric potential. It relates the electric potential with the free space charge distribution ρ_{f} of the ions in the system:

$$\varepsilon \nabla^2 \psi = -\rho_{\mathrm{f}} \tag{2.22}$$

or

$$\varepsilon \nabla^2 \psi = -\sum_i z_i e n_{i,\infty} \exp\left(-\frac{z_i e \psi}{k_B T}\right). \qquad (2.23)$$

This last equation is known as the Poisson-Boltzmann equation. ε represents the dielectric permittivity and is the product of the vacuum permittivity $\varepsilon_r = 8.85 \times 10^{-12}$ F m^{-1} and the relative permittivity ε_r of the continuous medium (for water $\varepsilon_r = 80$ at room temperature).

In general, when solved for a single charged surface, the solution for this equation gives ψ as monotonically decreasing in function of the distance to the surface. Typically the electric potential at the interface is assumed to be known and having a value ψ_S. The ion distribution producing this potential distribution is referred to as the diffuse double layer. Analytical solutions to the Poisson-Boltzmann equation can only be obtained in particular cases, for example when a symmetric z:z electrolyte is in contact with a planar charged surface. In this situation, known as the Gouy-Chapman theory, following relationship can be calculated between the potential distribution inside the double layer and the surface potential:

$$\tanh\left(\frac{ze\psi(x)}{4k_B T}\right) = \exp(-\kappa x)\tanh\left(\frac{ze\psi_S}{4k_B T}\right), \qquad (2.24)$$

where x gives the distance to the surface. The parameter κ is defined as

$$\kappa = \sqrt{\frac{e^2 \sum z_i^2 n_{i,\infty}}{\varepsilon k_B T}}. \qquad (2.25)$$

Its inverse, i.e. κ^{-1}, is known as the Debye screening length and is a measure for the double layer thickness. It is solely determined by the properties of the continuous medium. A plot of the potential distribution inside the double layer described by the Gouy-Chapman analysis is given in Figure 2-2.

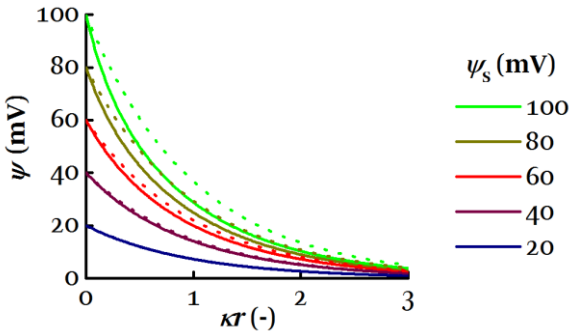

Figure 2-2: Distribution of the electrostatic potential in the double layer near a charged flat surface as a function of the scaled distance to this surface. The solid lines give the exact solution from the Gouy-Chapman analysis (equation (2.24)); the dashed lines present the Debye-Hückel approximation, equation (2.27). The latter gives an error of less than 10% for surface potentials up to 50 mV. This figure also reveals the physical meaning of the Debye length κ^{-1} : it is a measure for the thickness of the electrical double layer.

To obtain analytical solutions to equation (2.23) in more general geometries, e.g. to describe the double layer around a spherical particle, approximations to this equations are made. For surface potentials $\psi_S << k_B T/z_i e = 25\,\mathrm{mV}/z_i$, a first order approximation of the right hand side of equation can be made; this is known as the Debye-Hückel approximation of the Poisson-Boltzmann equation:

$$\nabla^2\psi = \kappa^2\psi \ . \qquad (2.26)$$

When considering a univalent symmetric electrolyte around a planar charged surface, the potential distribution in the Debye-Hückel approximation reads

$$\psi(x) = \psi_S \exp(-\kappa x) \ . \qquad (2.27)$$

A comparison between this approximation and the solution from the Gouy-Chapman analysis is given in Figure 2-2, from which it is seen that the above solution gives a good approximation of the potential distribution for ψ_S up to 50 mV. For a microsphere of radius r one calculates the potential distribution at a distance x from the surface as

$$\psi(x) = \frac{\psi_S}{1 + x/r} \exp(-\kappa x), \tag{2.28}$$

which approaches equation (2.27) for large values of r.

The above expression for the potential distribution around a spherical particle allows for the calculation of the surface charge density on that particle. Because of electroneutrality inside the system, the charge contained in the double layer should balance the surface charge. The charge distribution in the double layer is calculated from equation (2.22). By integrating this charge distribution in the space outside the particle, the total charge of the particle is retrieved. The surface charge density on that particle is found to be

$$\sigma = \varepsilon \kappa \psi_S \left(1 + \frac{1}{\kappa r} \right). \tag{2.29}$$

Some problems arise, however, when the electrical double layer is described as a diffuse cloud of counterions. Firstly, this description assumes that all possible energy states used in the Poisson-Boltzmann distribution can be reached. In practice this means the assumption of infinitesimally small ions is made which leads to inconsistencies in the theory, e.g. for high surface potentials an unreasonable concentration of ions is found close to the charged interface. Furthermore phenomena associated with the nature of the continuous medium, e.g. the formation of a hydration shell at the charged interface inhibiting ions to approach the surface, or non-Coulombic ion-ion interactions are not taken into account. This

limits the physical validity of the diffuse double layer model. These deficiencies are dealt with in more elaborate double layer models.

The Stern model accounts for some of the problems associated with associating an infinitesimal size to the ions, an assumption acceptable for the bulk part of the diffuse double layer but not near the interface. It introduces the concept of a stagnant layer, the so called Helmholtz layer, in between the particle surface and the diffuse double layer. This layer consists of ions and continuous medium molecules in direct contact with the interface and a layer of fully solvated ions. The potential ψ_d at the beginning of the diffuse part of the double layer is different from the surface potential and depends on the nature of the ions in the Helmholtz layer.

When the particle moves inside the fluid, a slipping plane can be defined and the potential at this plane of the particle is termed the ζ-potential. The fluid in between the particle surface and this slipping plane is considered to remain attached to the particle, while outside the plane the fluid can move relative to the particle. The precise location of this slipping plane is somewhat ambiguous. Obviously its position is outside the Stern layer. Many authors assume it to be near the outer Helmholtz layer at a distance of a few tenths of nanometers from the interface, thus effectively equating the ζ-potential with ψ_d [33], [34], [45]. However, some authors report situations in which the slipping plane must lie much further inside the diffuse double layer [46], [47]. In any case, any difference between ζ and ψ_d depends on the ionic strength: a higher ionic strength accounts for a steeper decay in electric potential and thus a larger difference between these two potentials.

The above calculations were made using time-independent differential equations, thus assuming a steady-state condition of the system. To support this, it is necessary to gain insight in the time scale at which a double layer is formed around an interface. An analytical approach involves combining the Poisson equation with the Nernst-

Plank equation, which describes ion fluxes in an electric field [33]. From this analysis a time scale of $1/\kappa^2 D_i$ arises with D_i the diffusion coefficient of the species. This timescale can intuitively be seen as the time needed for a species to move across the double layer thickness by diffusion. This characteristic time depends on κ and thus the ionic strength of the liquid. Typical applications in water involve a symmetric 1-1 electrolyte at concentrations higher than 0.1 mM, which provide a time scale of less than 1 μs for the double layer formation. Perturbations of the double layer at time scales much larger than this characteristic time can be considered to be in local equilibrium.

2.4 Colloidal stability

From a colloidal point of view, a dispersion is regarded as stable if its constituents do not aggregate at a significant rate. If two uncharged smooth particles are brought close together, typically in the order of a few nanometers, molecular dipole-dipole interaction make for an attractive force between them; a force known as the London-Van-der-Waals force. Due to Brownian motion, the separation between individual particles fluctuates in time. This makes that any two particles will eventually approach each other close enough such that their interaction energy compensates the thermal energy. The London-Van-der-Waals force makes that these two particles aggregate. A dispersion of smooth uncharged particles is therefore always unstable.

This aggregation process can be countered in a number of ways. For example, when the particles of a colloidal suspension are charged, an electrical double layer is formed close to their surface. When two of these particles approach each other, at a given point their double layers will overlap and interact, rendering a repulsive force between the particles. For a given separation, the energy associated with this double layer interaction is, among others, a function of the surface potential of the particle and the double layer thickness. Generally, more compact double layers will decrease the interaction distance. This implies that double layer interactions cannot prevent aggregation when they are too thin. The balance between the double layer repulsion and London-Van-der-Waals attraction has been described fully for two interacting spherical particles by Derjaguin, Landau, Verwey and Overbeek and is therefore called DLVO-theory.

A second way to stabilize a colloidal suspension is by steric stabilization. In this case the surface of a particle is provided with long molecular chains, either by grafting polymers on the surface or by adding a surfactant. A stable dispersion is obtained when the interaction energy between particles separated by the chain length is lower than the thermal energy.

2.5 Electrophoresis of a microsphere

Several experimental techniques exist to probe the electrical properties of colloidal particles. One approach is to directly measure the force on a single particle when it interacts with another charged interface. In the colloidal probe technique, the typical sharp tip on the cantilever of an atomic force microscope is replaced by a microsphere [48]. This sphere is brought in the proximity of a substrate or another microsphere and the force resulting from their electrostatic interaction is monitored by observing the displacement of the cantilever. Another way in which electrostatic interactions between two colloidal particles can be evaluated is by bringing two colloids close together with two optical tweezers, releasing them and looking at their trajectories [49]. This technique is called blinking optical tweezers [50].

An alternative approach consists of monitoring the response of colloidal particles to an external perturbation. Again, different methods can be identified, each with their own merits. For example, in electroacoustics the coupling between ultrasound waves and electric fields is used to characterize the electrical properties of colloidal particles [51]. The technique is particularly powerful when highly concentrated colloids are considered.

This dissertation uses electrophoresis to probe the electrokinetic properties of a single colloidal particle. Here, the movement of a colloidal particle in response to an externally applied electric field is considered. This section provides the necessary theoretical framework to interpret electrophoresis experiments.

2.5.1 Rigid spheres

A charged colloidal particle experiences a number of forces resulting from the interaction with an external electric field E. Firstly, the interaction of its bare charge q_s with the field renders an electric force equal to $q_s E$. As the particle moves through the suspending liquid, it also experiences a drag force proportional to its velocity. Thirdly the

electric field interacts with the free ions making up the electrical double layer. This provides additional hydrodynamic friction to the particle and the associated force is known as the retardation force. Also, at high electric fields or with particles having a surface potential higher than the thermal voltage, deformation of the double layer due to the applied electric field can occur. This causes a dipole force acting on the particle in a direction opposite to the electric force; the force is known as the relaxation force.

The balance between these four forces determines the movement of a colloidal particle in an electric field, i.e. electrophoresis. When a net force acts on the particle, for example by a sudden change in electric field strength, the particle accelerates until a velocity is reached such that the resulting drag force balances the other forces. This acceleration happens on a time scale of m/γ ($\approx 10^{-7}$ s for polymeric microspheres) after which the particle moves at a constant velocity. For low field strengths this velocity is proportional to the applied field strength and the proportionality factor is called the electrophoretic mobility μ_{EP} of the particle.

When investigating the electrical properties of a colloidal particle via an electrophoresis experiment, the mobility is often the only physical quantity that can be retrieved. It can, however, be linked to the ζ-potential of that particle based on theoretical grounds. Such an expression for μ_{EP} is typically established by jointly solving Poisson's equation (relating the electric potential with the free charges in the system) with the Navier-Stokes equations (providing the laminar flow profile) and the Nernst-Planck equations (describing the ionic fluxes), in the reference system of the particle. At the particle interface and in the bulk appropriate boundary conditions are applied [1] and the

[1] The boundary condition of the electric potential is defined at the shear plane of the particle. Hence it is the ζ-potential that determines the electrokinetic properties of the particle.

mobility is then retrieved as the opposite of the bulk fluid velocity divided by the applied field.

An analytical solution is found for a single spherical particle of radius r that has a ζ-potential not exceeding the thermal voltage. This last condition allows for linearization of the differential equations involved. One finds following expression for the electrophoretic mobility:

$$\mu_{\mathrm{EP}} = \frac{2\varepsilon\zeta}{3\eta} f(\kappa r), \tag{2.30}$$

in which $f(\kappa r)$ is a strictly monotonically increasing function known as Henry's function. For small values for κr, i.e. when the particle radius is much smaller than the double layer thickness, $f(\kappa r)$ reduces to 1; this is known as the Hückel limit. At large κr-values, the so-called Helmholtz-Smoluchowski limit, its value becomes 3/2. Intermediate values can be calculated using Ohshima's approximation for Henry's function [52]:

$$f(\kappa r) = 1 + \frac{1}{2\left(1 + \dfrac{2.5}{\kappa r\left(1 + 2\exp(-\kappa r)\right)}\right)^3}. \tag{2.31}$$

When the approximation of a small ζ-potential no longer holds, relaxation effects come into play. In this case a polarization force, resulting from an asymmetric electrical double layer, effectively reduces the mobility of the particle. The time scale at which this polarization occurs is in the order of the time that a counterion with diffusion coefficient D_i needs to migrate across the particle surface, i.e. r^2/D_i. It is for a spherical particle of radius 0.5 µm in the order of 0.1 ms. An analytical description of the mobility as a function of the zeta potential that includes these relaxation effects has been offered by Ohshima, Healy and White [53]. The expression is too elaborate to

include in this text, but is presented in various other handbooks, e.g. [54]. The Ohshima-Healy-White approximation is valid for arbitrary ζ-potentials but requires the product κr to be higher than 10. For situations not fulfilling this condition, numerical solutions to the coupled differential equations are the only way to retrieve the relation between the ζ-potential and electrophoretic mobility of a spherical particle. O'Brien and White have provided a numerical method to retrieve the mobility of a spherical particle when its ζ-potential and κr are known [55]. They have shown that, except for infinitely large or small values of κr, there is no linear relationship between ζ and μ_{EP}. Relaxation effects even make that, for a sufficiently high value of ζ and κr in the order of 1, the particle mobility becomes nearly independent of this potential.

2.5.2 Soft spheres

An analytical description of the electrokinetics of particles that do not possess a smooth surface is less established and requires an adapted approach [56]. Typically particles with a solid core and a liquid-penetrable shell are considered, so-called soft particles which are schematically drawn in Figure 2-3. Examples include polymer coated microspheres and biological cells. The presence of a porous shell accounts for hydrodynamic screening: the additional hydrodynamic resistance close to the particle surface effectively shifts the slipping plane outwards and screens charges behind this plane. The ζ-potential of a particle with neutral shell can be linked to the ζ-potential of the bare particle by the Gouy-Chapman theory, i.e. equation (2.24):

$$\tanh\left(\frac{ze\zeta_{coat}}{4k_BT}\right)=\exp(-\kappa l_s)\tanh\left(\frac{ze\zeta_{bare}}{4k_BT}\right). \qquad (2.32)$$

In this equation l_s is the translation of the slipping plane with respect to the slipping plane of the bare particle. It follows that the mobility of a particle with neutral coating will always be closer to 0 than the

mobility of a bare particle, when both have the same potential at the core surface.

This can be exemplified by examining how a non-ionic surfactant affects the mobility of a particle. For this I have considered 1 μm polystyrene particles suspended in either 0.10 g/l KCl solution or in the same solution with a mass fraction 0.2 % of the non-ionic surfactant Tween20 added. I have measured[2] the mobility of eight single particles in each solution under similar condition and found that the mobility of the particles in a solution that contained surfactant ($(-33.5\pm0.2)\times10^{-9}$ $m^2V^{-1}s^{-1}$) was reduced with 30 % compared to the mobility of the particles in the solution with no surfactant present ($(-48.3\pm1.3)\times10^{-9}$ $m^2V^{-1}s^{-1}$). This decrease in mobility results from the non-ionic surfactant attaching to the surface of the particle, thereby effectively increasing the particle's hydrodynamic radius without affecting its surface potential.

More generally the increased hydrodynamic resistance can be accounted for by introducing an additional friction term in the Navier-Stokes equation. This term is a function of the fluid velocity and the layer permeability. The shell may also carry a net charge, which affects the Poisson equation. Ohshima has provided analytical expressions for the mobility of soft particles in situations where relaxation effects can be neglected [54], [57]. Generally, these approximations hold as long as the potentials involved do not exceed the thermal voltage and the shell thickness is much larger than the fluid penetration depth inside the shell [58]. Hill and co-workers extended the work of O'Brien and White to provide numerical solutions of the electrokinetics of soft particles under more general conditions [56], [59].

[2] The measurement procedure will be discussed in depth in the following chapter.

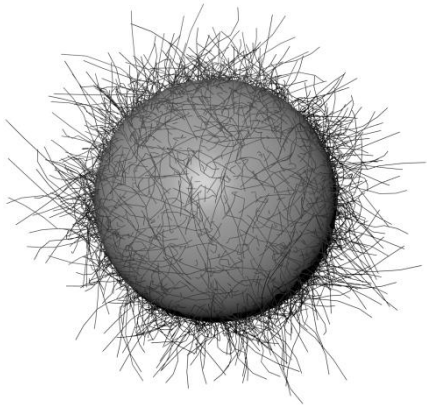

Figure 2-3: Schematic drawing of a soft particle. On the smooth core of the particle, polymer chains have been grafted. The continuous medium is able to enter in between the cavities. However, when the particle starts moving with respect to the continuous medium, the polymer chains attribute to additional hydrodynamic resistance, effectively pushing the slipping plane outwards. This affects the electrophoretic mobility of the particle.

2.6 Conclusions

This chapter has given an overview of the theoretical description of some colloidal phenomena that will play a role in the next chapters. Firstly, the motion of a colloidal particle in a suspension was described by a Langevin equation. It relates the drag force experienced by the particle with the thermal force, which causes Brownian fluctuations of the position. The statistical nature of the latter enabled a description based on the power spectral density of the positional signal.

Furthermore, charging inside colloids was considered. Because of the charges, an electrical double layer of counterions forms at the interface. A description of the potential and ion distribution inside this double layer was given. For a planar charged substrate, an analytical solution was obtained (Gouy-Chapman analysis), while for spherical particles a closed form solution could only be obtained by linearization of the governing differential equations (Debye-Hückel approximation) at low surface potentials. An important parameter emerging from these calculations is the reciprocal Debye length κ. Its inverse provides a measure for the thickness of the electrical double layer.

Also the effect of an external applied electric field on the motion of a particle was discussed. The translation of the particle along this field, electrophoresis, is described by the electrophoretic mobility μ_{EP}, i.e. the ratio of the particle velocity and electric field strength. An expression for the mobility was given in terms of the particle's ζ-potential, i.e. the electrostatic potential of the double layer at the slipping plane, and the reciprocal Debye length. It was furthermore shown, both theoretically and by experiment, that the presence of a soft layer, e.g. molecular chains, on the surface of the particle typically lowers the electrophoretic mobility of a particle due to an increased drag force.

Chapter 3
Experimental setup

3.1 Introduction

This chapter provides a detailed description of the experimental setup and data analysis methods used in the experiments that are discussed in the rest of the work. The first part of this chapter provides the theoretical background behind optical tweezers and a description of the forces and the motion of a particle inside these tweezers. Also the principle of particle detection via back focal plane interferometry is discussed, and how this detection method is used for the calibration of the optical tweezers. Lastly it is discussed how the data in an optical trapping electrophoresis (OTE) experiment is analyzed. The second part of this chapter is devoted to the practical realization of these concepts and additionally provides details about the used measurement chambers.

3.2 Optical tweezers

Light carries momentum. This momentum is changed when the light reflects, deflects or gets absorbed due to interaction with a certain material. Momentum conservation dictates that the interacting material experiences an equal but opposite change in momentum, resulting in a force on this material. The most notable example of this force is perhaps the tail formation of a comet. When a comet approaches the sun, dust and ice particles detach from its surface. These particles absorb and scatter sunlight and are consequently pushed away from the sun, creating the comet tail. This tail is thus always pointing away from the sun, regardless of the direction in which the comet is moving. Typically, the forces exerted by light are small and are hardly observable in a macroscopic environment that is dominated by forces comparable to the gravitational force. This is illustrated by considering the radiation pressure resulting from sunlight. The earth receives sunlight with an average irradiance of 1361 W/m^2 [60]. Absorption of this light by a macroscopic black body exerts a radiation pressure of 4.5 $\mu N/m^2$ and the resulting force would result in an insignificant acceleration. The mass and size of microscopic particles, however, is considerably smaller, which makes

inertial forces considerably smaller and the forces exerted by light comparatively larger.

Optical tweezers employ these forces to spatially confine a single colloidal particle. In essence, as is presented in Figure 3-1, a conventional optical tweezers setup consists of a TEM_{00} laser beam overfilling a high numerical aperture objective lens which creates a tight focus in the object plane of the microscope. The resulting intensity gradient in the focus of the laser is capable of attracting and holding dielectric particles ranging from tens of nanometers to tens of micrometers [61]–[63]. Since their introduction in the 1970-80's by Ashkin [64]–[66], optical tweezers have shown to be an indispensable tool in a variety of domains [67], [68]. Examples as the study of biomolecular properties and interactions at the single-molecule-level [69]–[71], cell manipulation [72], [73] or the experimental demonstration of fundamental thermodynamical theorems [74] provide merely a grasp at the extent to which optical tweezers are used in experimental settings nowadays.

Conventional optical tweezers rely on the forces resulting from the interaction of a tightly focused laser beam with a transparent particle. To make the working principle behind optical tweezers more intuitively clear, Figure 3-2 presents a ray optics description [75], [76]. In this figure, the focused laser beam is represented as a collection of rays that are concentrated in one point. This approximation is valid when the considered particle is considerably larger than the laser wavelength. Because of the refractive index difference between the particle and the surrounding medium, the rays get refracted and change momentum. Fresnel reflections at the interface are not included in this qualitative description. When its index is higher than the surrounding medium, the particle can be considered as a converging ball lens. This makes clear how the individual rays are refracted by the particle. For a particle with its center positioned in the focus of the laser beam (Figure 3-2(a)) the direction of the rays and thus the momentum of the light beam are not changed because of

symmetry considerations. Hence there is no momentum transfer from the light to the particle and the net force on the particle is zero. In Figure 3-2(b) the particle is displaced laterally. The beam is deflected along the direction in which the particle has moved. Momentum conservation calls for a force exerted on the particle in the opposite direction. This force is thus restoring in the sense that it tries to counter the particle movement. A similar restoring force emerges when the particle is displaced axially. When the particle is positioned downstream of the focus of the laser beam, see Figure 3-2(c), it increases the beam's convergence. The outgoing beam thus carries more momentum along the beam propagation axis than the incoming beam. The difference in momentum is transferred to the particle and results in a force towards the beam focus. For a particle placed upstream of the laser focus, as in Figure 3-2(d), a similar reasoning can be made to account for a force that is directed towards the laser focus. The force by the focused laser beam is thus a restoring force towards the focus.

3.2.1 Forces in optical tweezers

To know precisely what the magnitude is of forces involved in optical tweezers, one needs to calculate how the electromagnetic field of the focused TEM_{00} beam is altered after interacting with the particle. A ray optics approach allows for a quantification of the total force on large, i.e. larger than five times the wavelength of the laser light, spherical particles using only Fresnel reflection and Snell's law to calculate the momentum change of individual rays composing the focused beam [75], [77]. It provides an expression for the force of an individual ray on the particle. The force by a single ray can be split up into a component along the direction of the ray, and a component perpendicular to it. These components are conventionally termed the scattering force and gradient force, respectively. The force of the total beam on the particle is found by summing the forces of the individual rays constituting the beam. The gradient force on the particle, i.e. the sum of the gradient forces of the individual rays, is a conservative

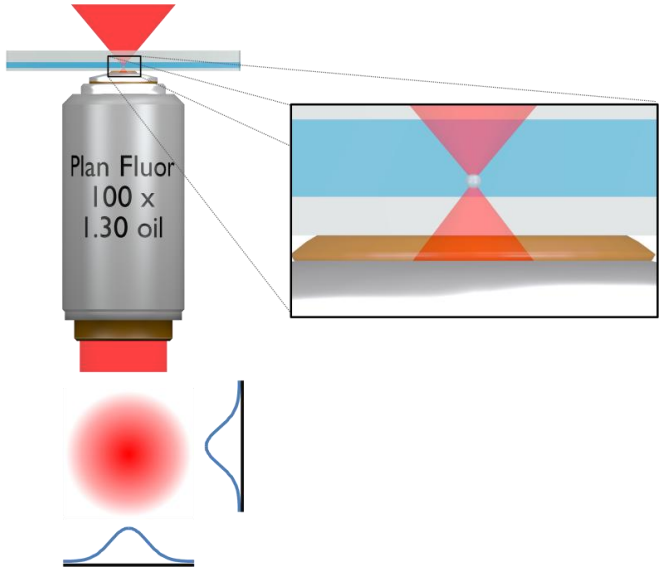

Figure 3-1: Schematic representation of optical tweezers. A TEM_{00} laser beam is tightly focused by a high numerical aperture objective. This creates a trap for transparent particles with a higher refractive index than the surrounding liquid.

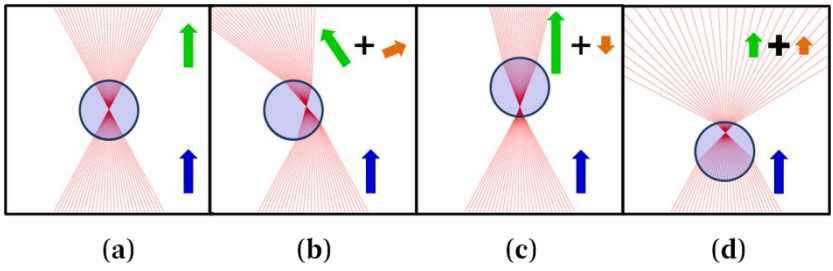

Figure 3-2: Working principle of optical tweezers in the ray optics regime. The particle acts as a converging lens when its refractive index is higher than the surrounding medium. When its center displaces from the laser focus, the particle changes the momentum of the incoming beam (blue arrow). By account of momentum conservation, this momentum equals the momentum of the outgoing beam (green arrow) plus the momentum transfer to the particle (orange arrow). The latter results in a force onto the particle, which is seen to be restoring.

force pulling the particle center to the beam focus. The total scattering force is non-conservative and manifests itself as pushing the particle along the beam axis. When the beam's numerical aperture is large enough, the sum of both forces provides an equilibrium point, i.e. a point where the total force is zero, located on the beam axis in front of the focus of the laser. When the particle displaces from this equilibrium point, it experiences a restoring force which is well approximated as being proportional to the displacement when the latter is smaller than the particle radius. The proportionality factor is referred to as the trap stiffness k_{trap}. This stiffness is not necessarily isotropic as will be discussed later.

Furthermore an analytical description of the forces for very small particles is possible as well; this is typically referred to as the Rayleigh approximation [78]. This approximation assumes the incident beam to be a constant, time-harmonic electric field. The polarizability α of a spherical particle with radius r is given by the Clausius-Mossotti relationship:

$$\alpha = 4\pi\varepsilon_0 r^3 \left(\frac{n_{\mathrm{p}}^2 - n_{\mathrm{m}}^2}{n_{\mathrm{p}}^2 + 2n_{\mathrm{m}}^2} \right). \tag{3.1}$$

The scattered electromagnetic fields can be calculated as the field of an elementary dipole. An integration of Maxwell's stress tensor retrieves the total force. The force can again be split up into a scattering force and gradient force on the particle. The gradient force is calculated as being proportional to the intensity gradient of the beam:

$$\mathbf{F}_{\mathrm{grad}} = \frac{\alpha}{2n_{\mathrm{m}}\varepsilon_0 c} \nabla I \,, \tag{3.2}$$

with c the speed of light in vacuum. The scattering force is directed along the local Poynting vector and its magnitude has the following dependency:

$$F_{\text{scat}} \propto \frac{\alpha^2}{\lambda^4} I(\mathbf{r}). \tag{3.3}$$

Since α is proportional to the volume of the particle, it follows that the scattering force becomes negligible for small particles. Also, a lower limit on the size of the particle emerges: for small enough particles the thermal fluctuations cannot be overcome by the gradient force.

When considering arbitrarily shaped particles, one needs to resort to numerical methods to describe the scattering of the laser beam and the associated forces. For optical tweezers, the T-matrix method often offers satisfactory results [76], [79]. A Matlab program implementing this numerical method has been made available by Nieminen and coworkers [80]. In this method, the internal and scattered fields are decomposed as vector spherical wave functions (VSWF's), the so-called multipole expansion. These VSWF's constitute a discrete basis for any solution to the vector Helmholtz wave equation in spherical coordinates. The scattered field resulting from the interaction of one of these waves with the particle can again be decomposed in VSWF's, thus the whole scattering problem reduces to finding the scatter matrix describing the expansion coefficients of the scattered fields in function of the coefficients of the incoming field. This T-matrix solely depends on the shape and optical properties of the particle involved and routines for calculating this matrix are provided in literature [81]. For spherical particles the T-matrix can be calculated analytically via generalized Lorentz-Mie scattering theory. With the incoming and scattered electromagnetic fields known, the force on the particle can be retrieved.

The aforementioned T-matrix computational toolbox can be used to provide insight into the magnitude of the forces exerted by a focused laser beam on a dielectric microparticle. As a representative example for the rest of this work I have calculated the forces on a polystyrene particle of 1 μm suspended in water when the particle is placed near the focal spot of a linearly polarized TEM_{00} beam of 10 mW with a 975

nm vacuum wavelength and a numerical aperture of 1.3. In Figure 3-3 (a) the particle is displaced laterally through the equilibrium point of the optical tweezers. The graph displays the force the particle experiences in the same direction as this translation. Also presented is a linear approximation of this force near this equilibrium point. Figure 3-3 (b) presents the axial force when the particle moves along the beam axis together with the linear approximation. The equilibrium point is seen to lie on the beam axis at a distance of 0.101 μm from the laser focus. The graphs also indicate the linearity of the trap hold over several hundreds of nanometers, which is typical for optical tweezers [82]. A value of the trap stiffness in both directions is also retrieved: $k_{trap,x} = 19.3$ pN μm^{-1} and $k_{trap,z} = 16.0$ pN μm^{-1}.

Furthermore, these numerical calculations provide a way to investigate the influence of specific properties of either the particle, medium or laser beam on the performance of the optical tweezers. In Figure 3-4 I present, as an example, how the trapping stiffness in the three spatial directions is affected as a function of the particle radius while all other properties, such as beam shape and the refractive index of the particle and the medium, are left unaltered. The laser beam has the same properties as described in Figure 3-3 and the x-direction corresponds with its linear polarization. From the graph it is seen that the trap stiffness is highly dependent on the particle size. For small particles, i.e. with a radius less than 0.25 μm, the stiffness is seen to increase with the radius r. The plotted lines reveal the r^3-dependence of the trapping stiffness, agreeing with the expression for the force provided by the Rayleigh approximation (equation (3.2)). For large particles the trap stiffness appears inversely proportional to the particle radius. This can be understood by, as discussed above, considering a particle as a converging ball lens. The change in momentum of the beam is determined by the focal length l_f of this lens. For small particle displacements from the equilibrium position, a paraxial approach can be used for every ray, which gives a change in angle proportional to $1/l_f$. Since the focal length of a ball lens is

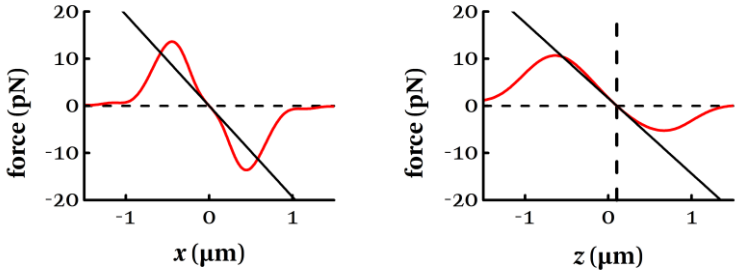

Figure 3-3: The forces experienced by a 1 μm polystyrene particle in water when interacting with a focused laser beam (λ=975 nm; NA = 1.3; *x*-polarized; power = 10 mW). The laser focus is at position (0,0). In (a) the force in the positive *x*-direction is plotted when the particle moves along the *x*-axis, i.e. one of the lateral directions, from the equilibrium point; in (b) the axial force is plotted for an axial movement of the particle. The equilibrium point is the point where both forces are zero. The black solid lines give a linear approximation of the force near the equilibrium point.

proportional to the radius of this lens, an r^{-1}–dependence of the trap stiffness is indeed expected for large particles. The figure also reveals that the trap stiffness reaches a maximum for particles having approximately the same diameter as the wavelength of the laser beam.

Secondly it is observed that in general the trap stiffness proves to be asymmetric in the three spatial dimensions. This is especially noticeable for small particles. The gradient force described in the Rayleigh approximation can only show directional dependence if the intensity gradient of the focused laser shows an asymmetry, as given by expression (3.2). The difference between the lateral and axial trapping stiffness is intuitively understood: the focused laser spreads out over a larger distance in the axial direction than in the lateral directions, contributing to a smaller intensity gradient and thus a smaller trap stiffness. The difference between the two lateral trap stiffnesses is explained by a polarization dependent intensity profile

in the focus spot of the laser. This polarization-dependent intensity profile does not occur in the typical paraxial description of Gaussian beams. However, this description does not adequately describe a strongly focused laser beam. The multipole expansion of a focused TEM_{00} beam, used in the numerical calculations of Figure 3-4, does show a polarization-dependent intensity asymmetry in the laser focus [83]: for an x-polarized laser beam, the waist in the y-direction is narrower than in the x-direction. This explains why the numerical calculations provide a higher trap stiffness in the y-direction. For particle radii larger than the half wavelength of the laser light, the lateral trapping stiffness shows oscillations as a function of the particle radius. This is a result of interference effects caused by multiple reflections of light inside the particle, much like with a Fabry-Pérot etalon [84].

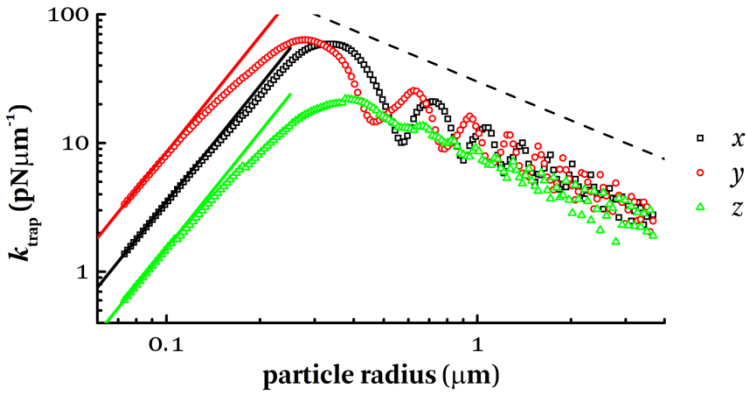

Figure 3-4: Variation of the trap stiffness k_{trap} as a function of the particle radius as calculated by a T-matrix numerical method [80]. The trap stiffness proves to be asymmetric and polarization dependent. For small particles the stiffness increases with an r^3-dependence (represented by the solid lines), as is predicted by the Rayleigh approximation. For large particles the stiffness decreases inversely proportional to the particle radius, agreeing with the ray optics description (the black dashed line has a r^{-1}-dependence)

3.2.2 Particle movement inside optical tweezers: Brownian motion in a harmonic potential

The previous section has shown that optical tweezers exert a Hookean force on the particle when displaced from its equilibrium position in the trap. Because of this trapping force, the Langevin equation describing the movement of the particle (see section 2.2.2) transforms into

$$\gamma \frac{\mathrm{d}x}{\mathrm{d}t} + k_{\mathrm{trap}} x = \sqrt{2k_{\mathrm{B}}T\gamma}\,\xi(t)\,. \tag{3.4}$$

The inertial term is neglected, assuming time scales much larger than the characteristic acceleration time of the particle $\tau_{\mathrm{accel}} = m/\gamma \approx 50$ ns. The equation of the particle movement resembles that of a heavily overdamped oscillator driven by the thermal force.

When considering an ensemble of identical optically trapped particles at a certain time or, equivalently, making a large number of independent observations of the position of the particle in the harmonic potential well, Boltzmann-statistics provides the probability of finding a particle in an infinitesimal interval around a certain displacement x from the equilibrium position:

$$\wp(x) \propto \exp\left(-\frac{k_{\mathrm{trap}} x^2}{2k_{\mathrm{B}}T}\right). \tag{3.5}$$

The particle position, when observed for a sufficiently long time interval, thus follows a Gaussian statistic with mean zero, i.e. the equilibrium position, and standard deviation equaling

$$\left\langle x^2 \right\rangle = \frac{k_{\mathrm{B}}T}{k_{\mathrm{trap}}}\,. \tag{3.6}$$

But what is a sufficiently long time interval? To answer this, first the power spectral density of the position is calculated from the Fourier

transform of equation (3.4). By applying Wiener-Khinchin theorem, the autocorrelation of the particle position is retrieved from this power spectral density:

$$\langle x(t)x(t+\tau)\rangle = \frac{k_B T}{k_{trap}} \exp\left(-\frac{k_{trap}}{\gamma}\tau\right). \quad (3.7)$$

This expression provides a characteristic time equal to γ/k_{trap}. Position measurements at time scales longer than this characteristic time can be considered uncorrelated. At time scales much shorter than this characteristic time, corresponding to the limit of vanishing trap stiffness, the particle behaves as if it is freely diffusing.

3.2.3 Back focal plane interferometry

Microscopy techniques are widely used to characterize colloidal dispersions. Traditional microscope systems typically visualize a sample by imaging onto a CCD camera. The resulting large field of view is often a prerequisite for measurements over longer time, since the position of individual particles changes due to Brownian motion. Moreover, the large field of view enables a multi-parameter characterization of several particles at once [85], [86]. With the aid of advanced image analysis, the location of individual particles can be determined at a resolution much below the diffraction limit, with a minimal achievable localization accuracy of a few nanometers in the focal plane [50], [87]. However, these systems are typically limited to frame rates of 30-100 Hz. High-speed cameras do achieve bandwidths of several kHz [88], but are, aside from being very expensive, burdened with complicated data handling and increased shot noise due to a limited exposure time [89], [90].

Optical tweezers reduce the Brownian motion of a trapped particle significantly. This allows for other position detection techniques achieving much higher bandwidths and precision than traditional video imaging [91]. One of these techniques is based on imaging the interference pattern of the light coming from a laser beam focused on

a particle, formed at the back focal plane of the condenser lens of the microscope onto a detector and is therefore called back focal plane interferometry. The technique can provide three-dimensional position measurements at acquisition rates up to several MHz without giving in on accuracy or making data management problematic [92], [93]. The bandwidth of the system is often limited to tens of kHz, however, due to laser power fluctuations, the diode or amplifying electronics bandwidth or shot noise resulting from the limited number of photons detected per time interval [94], [95].

Typically a quadrant detector, consisting of four photodiodes arranged in a square, is used for back focal plane interferometry. It is placed in a plane conjugate to the back focal plane of the condenser lens, as is represented in Figure 3-5. The front focal plane of the condenser coincides with the object plane of the microscope. One advantage of this arrangement is that the intensity impinging on the detector is independent of the lateral position of the laser focus in this object plane. The intensity profile in the condenser's back focal plane represents the angular spectrum intensity of the focused laser after interacting with the particle. The intensity profile reaching the quadrant photo diode can be calculated explicitly. Analytical expressions for this profile in a paraxial approximation and for a small scatterer compared to the wavelength are available [95], [96], as are expressions using Mie scattering theory, hence relieving the restriction of small particles [97]. These results indicate the variation in intensity difference between two halves of the quadrant photodiode can be considered proportional to the lateral displacement of the particle from its equilibrium position for displacements that are well below the particle size. The axial displacement of the particle is found to be proportional to the variation of the total intensity impinging on all four quadrants, again for small enough displacements. Rohrbach *et al.* have calculated the linear range and the detection sensitivity in the axial direction is increased with a low-NA condenser [97]. Lateral detection is optimized by using a condenser with a high NA.

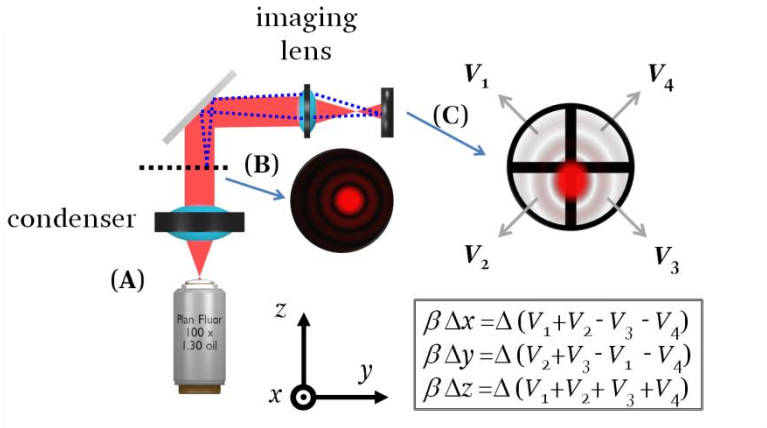

Figure 3-5: Schematic representation of the working principle of back focal plane interferometry. The particle is trapped in the focus of the laser (A). The laser light scattered by the particle is collected by a condenser lens. The resulting interference pattern (B) at the back focal plane of the condenser (dashed black line) is imaged onto a quadrant detector (C). The lateral displacement of the particle from its equilibrium position is determined by the difference in intensity impinging on two halves of the quadrant detector; the axial particle displacement is considered proportional to the variation of total intensity on the QPD. β (unit: Volt per meter) represents the conversion factor between the output of the QPD (unit: Volt) and particle displacement (unit:meter)

Alternatively, the linear range of detection via back focal plane interferometry can be increased by reducing the beam waist of the detection beam, as has been demonstrated by Martinez and coworkers [98].

Optical tweezers calibration

Back focal plane interferometry provides three voltage signals, each proportional to the particle position in one of the three spatial dimensions. These signals are however uncalibrated and a conversion factor β (unit: Volt per meter) between the output of the QPD (unit: Volt) to the spatial coordinates (unit: meter) is needed. Moreover, to

fully calibrate the optically tweezed particle and perform quantitative measurement with the optical tweezers, a value of the trap stiffness is needed. There exist different methods to achieve this calibration [99]. In this work, calibration of optical tweezers is done by power spectrum analysis, which will be explained and exemplified in this section.

The calibration procedure makes use of the spectral information of the positional signal obtained by back focal plane interferometry [100], [101]. To account for finite sampling in the frequency domain, the discrete Fourier transform $\hat{x}$ of the continuous positional signal x measured over a time interval t_{msr} is considered:

$$\hat{x}(k) = \int_{-\frac{t_{\mathrm{msr}}}{2}}^{\frac{t_{\mathrm{msr}}}{2}} x(t)\exp(-2\pi i f_k t)\,\mathrm{d}t\,. \tag{3.8}$$

In this expression the discrete frequencies are defined as $f_k = k/t_{\mathrm{msr}}$ with k an integer. By applying the Fourier transform on the Langevin-equation (3.4) the experimental power spectrum of the QPD signal $\beta\, x(t)$ can be calculated:

$$P_x^{(\mathrm{ex})}(k) = \frac{|\beta\hat{x}(k)|^2}{t_{\mathrm{msr}}} = \frac{\beta^2 D\left|\hat{\xi}(k)\right|^2}{2\pi^2 t_{\mathrm{msr}}\left(f_c^2 + f_k^2\right)}\,. \tag{3.9}$$

The corner frequency of the optical trap is defined as

$$f_{\mathrm{c}} = \frac{k_{\mathrm{trap}}}{2\pi\gamma}\,. \tag{3.10}$$

Since both the real and imaginary part of $\hat{\xi}(k)$ have a Gaussian distribution, $\left|\hat{\xi}(k)\right|^2$ is exponentially distributed and thus the individual data points of the experimental power spectrum as well. Its

expected value can be calculated considering the property $\left\langle \hat{\xi}(k)\hat{\xi}^*(l)\right\rangle = t_{\mathrm{msr}}\delta_{k,l}$:

$$P_x(k) = \left\langle P_x^{(\mathrm{ex})}(k)\right\rangle = \frac{\beta^2 D}{2\pi^2\left(f_c^2 + f_k^2\right)}, \tag{3.11}$$

which takes the form of a Lorentzian. The individual points of the experimental power spectrum are exponentially distributed around this expected value with a variance equaling

$$\sigma^2 = \left\langle \left(P_x^{(\mathrm{ex})}(k) - P_x(k)\right)^2 \right\rangle = P_x^2(k). \tag{3.12}$$

Values for the corner frequency f_c and conversion factor β can now be found by fitting (3.11) to the power spectrum of the QPD output signal. However, the exponential distribution of these data points makes a fit troublesome, since least-square fitting requires the individual data points to be normally distributed around their expected value. By binning, i.e. averaging a number of neighboring data points into a single point, this normal distribution is achieved by account of the central limit theorem and a statistically correct fit can be made.

The above derivation assumes a continuous-time position signal. In practice, the signal retrieved from the QPD is sampled in time at a frequency f_S. This introduces errors due to aliasing. In the power spectrum only frequency components in the range $[-f_{\mathrm{Nyq}}, f_{\mathrm{Nyq}}]$ are considered, with $f_{\mathrm{Nyq}} = f_S/2$ the Nyquist frequency. However, frequency components outside this range also carry power. Aliasing makes that this power falling outside the Nyquist range is translated inside this range, hence falsely increasing the power spectrum. For frequencies much below the Nyquist frequency, the error due to aliasing is negligible. This is why the position signal is always largely oversampled compared to the frequency range of interest. Moreover,

aliasing can be accounted for easily by the use of an anti-aliasing filter.

Fitting the Lorentzian to the experimental power spectrum is done based on a Matlab-routine, which implements the above considerations, made available by Tolić-Nørrelykke and co-workers [102]. The routine provides an estimate for the corner frequency (in Hz) and the diffusion coefficient D_{fit} (unit: $\text{V}^2\,\text{s}^{-1}$). Furthermore, values for the standard deviation on these estimates, as derived in [100], are also provided.

The trap stiffness is retrieved from the estimate of the corner frequency since the Stokes coefficient γ (equation (2.3)) is known. The value of the conversion coefficient follows trivially form the fitted diffusion coefficient because the diffusion coefficient D of the particle, given by equation (2.19), is known:

$$\beta^2 = \frac{D_{\text{fit}}}{D} \,. \tag{3.13}$$

Experiments in this dissertation use calibrated particles of which the standard deviation on the radius is less than 5 %. The mean radius, as provided by the manufacturer, is always used to calculate the Stokes coefficient and the diffusion coefficient.

Figure 3-6 demonstrates power spectrum analysis of the position of an optically tweezed particle of 1 µm diameter suspended in a 30 g/l KCl solution without added surfactant. Its position is measured for 15 seconds at a rate of 50 kHz. From the QPD voltage signal corresponding with one of the lateral spatial dimensions, a power spectrum is calculated, binned and fitted to equation (3.11). This fit estimates f_c to be 1435±15 Hz, allowing to retrieve the trap stiffness from equation (3.10) as $k_{\text{trap}} = 81\ \text{pN}\ \mu\text{m}^{-1}$. In this calculation the value for the Stokes coefficient $\gamma = 8.93\times10^{-9}\ \text{kg}\ \text{s}^{-1}$ is used. The fitted diffusion coefficient in voltage units equals $(126.4\pm1.7)\times10^{-3}\ \text{V}^2\ \text{s}^{-1}$. Considering the particle radius, the diffusion coefficient is calculated

as $D = 4.48\times10^{-13}$ m^2 s^{-1}. From equation (3.13) the value for the conversion factor is determined as $\beta = 0.53$ V μm^{-1}. Note that this conversion factor is sensitive to the alignment of the detection laser beam with respect to the trapped particle, and is therefore determined for every experiment separately.

The power spectrum takes on the typical shape of a Lorentzian: it is frequency independent for frequencies much below the corner frequency and has a roll-off proportional to f^{-2} at frequencies much above it. This roll-off is characteristic for the power spectrum of a freely diffusing particle, i.e. when the trap stiffness and thus the corner frequency are zero. Two regimes can thus be identified: at frequencies much above the corner frequency of the optical trap, the particle behaves as if it were freely diffusing. At frequencies much below the corner frequency the power spectrum resembles a white noise spectrum and accounts for uncorrelated positional information in time. Note that the expression for the corner frequency agrees with the time constant given for the autocorrelation time of the particle position in the trap, i.e. equation (3.7). Anti-aliasing makes that the f^{-2} dependency does not hold at frequencies near the Nyquist frequency.

Based on the above calibration, it is now possible to convert the recorded voltage signals into units of length. As an example Figure 3-7 presents a histogram of the positional data used in figure Figure 3-6, both in a linear scale as in a semi-logarithmic scale. From equation (3.5) it follows that the particle position probability distribution is Gaussian around its equilibrium position. Both graphs show the best fit of this distribution to the histogram. The fit provides a standard deviation of the position of 11.3 nm around the equilibrium position. The graphs provide a way to verify the assumptions made allowing the particle position to be described by the Langevin equation (3.4). More specific, since the Gaussian distribution approximation of the particle position in the optical trap holds up to several decades, the potential well created by the optical tweezers is indeed quadratic and the

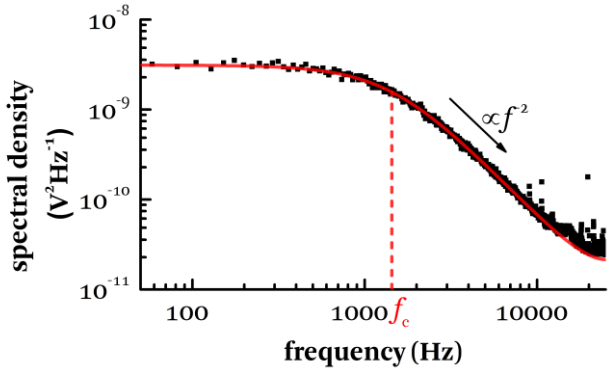

Figure 3-6: The experimental power spectrum of a particle inside optical tweezers recorded by back focal plane interferometry is given by the black squares. The red curve gives the anti-aliased Lorentzian fit to this spectrum. Hence a calibration of the optical tweezers is obtained: the corner frequency f_c provides a measure for the trap stiffness.

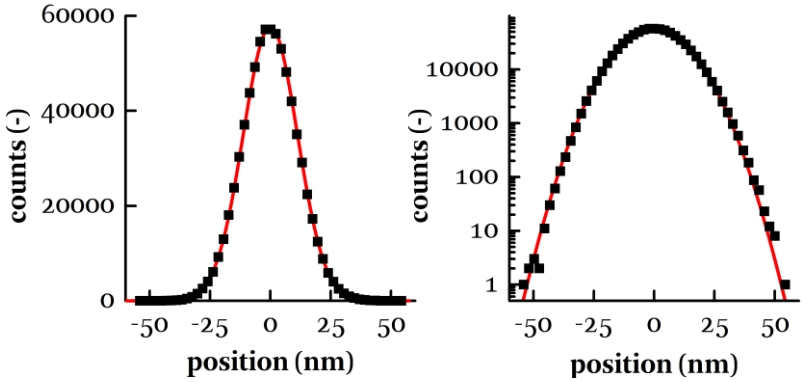

Figure 3-7: The position of a trapped particle follows a Gaussian distribution around the equilibrium position. Both graphs provide the same data: the black squares give the histogram of the lateral position of a 1 µm particle held by optical tweezers as measured by back focal plane interferometry; the red curve represents the best-fit to a Gaussian. From the semi-logarithmic graph on the right it follows the assumed linearity of the trapping force with the particle displacement and the proportionality of the QPD-signal with the particle position holds.

associated force is Hookean for the considered particle displacements. Moreover, it confirms that QPD-signals obtained by back focal plane interferometry are indeed linear with the particle position.

Throughout this dissertation, the optical tweezers are always calibrated using power spectrum analysis. From the positional signal, recorded at 50 kHz, an experimental power spectrum is calculated. Bins containing 350 neighboring data points are used to obtain the power spectrum to which the fitting is done, effectively reducing the number of points to which is fitted by a factor 350. Fitting is done over the frequency range of 100 Hz to 2000 Hz. Lower and higher frequencies are excluded since they are often found to contain noisy components, either from mechanical disturbances or from power fluctuations of the detection laser. Note that in some experiments described in this thesis a sinusoidal electric field at a certain frequency is applied to probe the electrical properties of the trapped colloidal particle (see section 3.2.4). This electric field induces an oscillation of the particle at the same frequency as the electric field which manifests itself as a peak in the power spectrum (see also subsection 3.2.4). This impairs the fitting procedure. For this reason the measurement point of the power spectrum corresponding with this applied frequency is always removed when fitting the Lorentzian to the measured spectrum.

3.2.4 Optical trapping electrophoresis

The electrical properties of a colloidal particle are often probed by observing how this particle moves in an applied electric field. Most conventional techniques employing electrophoresis as a characterization tool, for example by laser Doppler velocimetry or dynamic light scattering [103], perform a measurement on relatively concentrated suspensions and deliver the average electrokinetic properties over a large number of particles. Despite their high accuracy and reproducibility, the measurements done with these conventional techniques have some drawbacks. For example, the

monitoring of time-dependent changes in electrokinetic properties, for example by a changing medium, proves often difficult to realize in these experimental setups. Moreover, observing the electrophoretic movement of a single particle can reveal electrokinetic properties that cannot be assessed with conventional measurements. This is demonstrated in an experiment by Strubbe *et. al.* in which they have resolved time-dependent charging of a silica particle in a nonpolar medium with the precision of the elementary charge [104]. Their technique uses micro-electrophoresis, in which the electrophoretic movement of individual particles is observed with a microscope.

Optical trapping electrophoresis (OTE) combines this micro-electrophoresis technique with optical tweezers. Aside from the increased precision and time resolution at which the position fluctuations of a particle are determined, this combination offers other advantages. Because of the tweezers, the mean particle position is fixed, such that sedimentation and diffusion of particles are easily overcome. Moreover, fixing the particle in a measurement cell increases the reproducibility of the measurements. As will be seen in Chapter 5, position-dependent flow arises when performing an electrophoretic experiment in a microchamber. By knowing the position of the particle, this flow can be accounted for. Finally, when combined with adapted microfluidics, optical tweezers offer a way to easily change the surrounding medium in which the particle resides and to monitor the effects of this change on the electrokinetic properties of a single particle in a time-resolved fashion.

Data analysis

In a typical optical trapping electrophoresis experiment, a single optically trapped particle is subjected to a harmonic electric field $E(t) = E_0 \cos(2\pi f_E t)$ at a frequency f_E. The electric field yields a force on the particle equal to $\gamma \mu_{EP} E$, with μ_{EP} the electrophoretic mobility of the particle. When the particle's inertia can be ignored, i.e. at applied frequencies much below $\gamma/(2\pi m)$, the Langevin equation (3.4) is adapted to

$$\gamma \frac{\mathrm{d}x}{\mathrm{d}t}(t) + k_{\mathrm{trap}} x(t) = \sqrt{2k_{\mathrm{B}}T\gamma}\,\xi(t) + \gamma\mu_{\mathrm{EP}}E_{\mathrm{o}}\cos\left(2\pi f_{\mathrm{E}}t\right). \qquad (3.14)$$

When performing an electrophoresis experiment, one aims at retrieving the electrophoretic mobility of a particle from the recorded position $x(t)$. Often this is done by power spectrum analysis [29], [31]. By a similar reasoning as in subsection 3.2.3, the expected value of the experimental power spectrum of the position signal governed by the above equation can be calculated. Assuming f_{E} to be a multiple of $1/t_{\mathrm{msr}}$ and calibrated tweezers, i.e. the power spectrum has units $\mathrm{m^2 s}$, one retrieves:

$$P_x(k) = \frac{D}{2\pi^2\left(f_k^2 + f_{\mathrm{c}}^2\right)} + \frac{\mu_{\mathrm{EP}}^2 E_{\mathrm{o}}^2 t_{\mathrm{msr}}}{16\pi^2\left(f_k^2 + f_{\mathrm{c}}^2\right)}\left(\delta_{k,\mathrm{E}} + \delta_{-k,\mathrm{E}}\right), \qquad (3.15)$$

where $\delta_{k,\mathrm{E}}$ equals one if $f_k = f_{\mathrm{E}}$ and zero if this condition is not fulfilled. The experimental power spectrum of a harmonically driven particle is thus a Lorentzian apart from a peak at the drive frequency. This is demonstrated in Figure 3-8, which gives the binned[3] experimental power spectrum of a 1 µm polystyrene particle suspended in a 0.10 g/l KCl solution. The particle is subjected to an electric field (amplitude E_{o} = 3.14 kV $\mathrm{m^{-1}}$ and frequency f_{E} = 1000 Hz) and its position is recorded for 15 seconds. The spectrum is calibrated as described in the previous section, hereby omitting the point at f_{E} to properly fit equation (3.11) to the experimental power spectrum. The mobility can be retrieved by calculating the distance $\Lambda_{f_{\mathrm{E}}}$ between the Lorentzian fit and the point in the experimental power spectrum at f_{E}. More rigorously, one calculates that

[3] The value at f_{E} was taken from the unbinned spectrum, since binning would reduce the peak height with a factor approximately equal to the number of points per block.

$$\left\langle \Lambda_{f_E} \right\rangle = \left\langle P_x^{(ex)}(f_E) - P_{x,Br}(f_E) \right\rangle = \frac{\mu_{EP}^2 E_o^2 t_{msr}}{16\pi^2 \left(f_E^2 + f_c^2 \right)}. \qquad (3.16)$$

In this expression $P_x^{(ex)}$ represents the experimental power spectrum and $P_{x,Br}$ is the Lorentzian fit given by equation (3.11), i.e. the expected value of the power spectrum when no field is applied. The expected value of the quantity Λ_{f_E} is thus proportional to the square of the electrophoretic mobility.

From equation (3.15) the amplitude of the harmonic oscillation of the particle at f_E directly follows:

$$|\Delta x|^2 = 4 \left\langle \Lambda_{f_E} \right\rangle t_{msr}. \qquad (3.17)$$

Note, however, that this calculation of the oscillation amplitude does not assume any phase dependence of the oscillation with respect to the driving force. The lack of knowledge of the phase difference between the electric field and the particle displacement implies that the sign o1f μ_{EP} cannot be retrieved using the above analysis method.

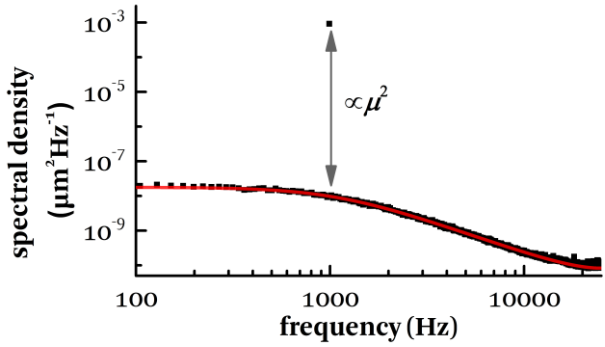

Figure 3-8: Calibrated power spectrum of an optically tweezed 1 µm polystyrene particle driven by a sinusoidal electric field. The resulting oscillation manifests itself as a peak in the spectrum of which the height is approximately proportional to the square of the electrophoretic mobility of the particle.

Moreover, if the particle mobility approaches zero, the above method becomes less suitable due to the appearance of negative values of Λ_{f_E} and a wrongful estimate of μ_{EP}. To overcome these problems, an alternative way to estimate μ_{EP} is presented [26]. When considering the Fourier transform of the position signal

$$\hat{x}^{(ex)}(k) = \frac{\sqrt{2D}\hat{\xi}(k)}{2\pi(f_c + \mathrm{i}f_k)} + \frac{\mu_{EP}E_0 t_{msr}}{4\pi(f_c + \mathrm{i}f_k)}\left(\delta_{k,E} + \delta_{-k,E}\right), \tag{3.18}$$

it is easily seen that an estimate of the mobility is obtained via

$$\left\langle f_c \,\mathrm{Re}\left[\hat{x}^{(ex)}(f_E)\right] - f_E \,\mathrm{Im}\left[\hat{x}^{(ex)}(f_E)\right]\right\rangle = \frac{\mu_{EP}E_0 t_{msr}}{4\pi}. \tag{3.19}$$

The theoretical variance on this estimate of the mobility equals

$$\sigma_\mu^2 = \frac{4D}{E_0^2 t_{msr}}. \tag{3.20}$$

Note, however, that equation (3.19) assumes μ_{EP} to be real-valued. This is the case when the harmonic movement of the particle is due to a driving force in phase with the electric field, as is the case with electrophoresis. As will be seen in Chapter 5, the oscillation of the particle in an OTE-experiment can also be governed by other harmonic forces that are not necessarily in phase with the applied field. This oscillation is then described by introducing a complex mobility. However, equation (3.19) will not retrieve the oscillation amplitude in this case, but rather the amplitude of the oscillation corresponding with the real part of the mobility, i.e. generated by the force terms in phase with the applied field.

3.3 Practical implementation

3.3.1 Optical setup

To realize single-beam gradient optical tweezers, a laser beam is manipulated such that it overfills the back aperture of a high numerical objective. Literature offers extensively reviews and schemes on how to build an optical setup offering tweezers capability and easy beam steering [105], [106]. The optical setup used in this thesis differs slightly from conventional optical tweezing setups, mainly because beam steering is done with lenses instead of, as is often the case, with mirrors.

Figure 3-9 gives a schematic representation of the most important components of the optical setup providing the optical tweezers. The setup is built around an inverted microscope (Nikon Ti-E) and mounted on an anti-vibration optical table. The experiments are done using an infinity-corrected 100x magnification oil immersion objective lens with 1.3 numerical aperture (Nikon CFI Plan Fluor 100XOil) to achieve a diffraction limited laser spot near the object plane of the microscope. A translation stage enables moving this objective lens axially with a resolution of 25 nm.

Two lasers are coupled in simultaneously in the objective. A near-infrared (NIR) laser beam (Thorlabs PL980P330J), operating at 975 nm wavelength and achieving a maximal output power of 330 mW, traps the particle. A red laser beam (Lasos RLD-638-150), used for back focal plane interferometry, emits at a wavelength of 638 nm and is operated at 30 mW. Both laser beams follow a separate but similar path before being merged. Firstly both beams pass a pinhole, which acts as a spatial filter to improve the beam quality. Next, both beams are linearly polarized with the aid of a quarter wave plate followed by a half wave plate. After this the beams pass individual beam steering optics, discussed below, enabling control of the focused laser beam in the object plane of the microscope. A dichroic mirror merges the two beams, and a beam expander provides the correct beam diameter to

overfill the back aperture of the objective. After having interacted with the particle, the scattered light of both beams is collected by a condenser lens (Nikon Ti-C-CLWD, NA 0.72) and the red light is directed towards the quadrant photodiode (Thorlabs, PDQ80A) by a dichroic mirror. Additionally, a microscopic image is provided by imaging the Kohler-illuminated sample onto an EM-CCD camera (Andor, iXon+).

The multifarious optical setup does however result in a power loss of the laser beam. Firstly, the pinhole reduces the beam power by half, after which the beam steering and telescope lenses contribute to an additional loss of 50 %. Overfilling the objective accounts for an additional 20 % loss. The objective is specified by the manufacturer to transmit 70 % of the NIR laserlight. The total power loss is estimated to be approximately 90 %. A similar loss is obtained for the detection laser beam.

a. Beam steering

The beam steering section of the optical setup allows for three independent transformations of the laser focus:

1. An orthogonal movement of the laser focus with respect to the object plane of the microscope
2. A lateral movement of the focus in the object plane
3. A tilt of the laser beam with respect to the axis of the microscope objective

These beam manipulations are achieved by altering the incoming beam at the back focal plane of the microscope objective, as is illustrated in Figure 3-10. By generating conjugate planes to the back focal plane and thus essentially repeating this plane along the optical train, the individual manipulations can be separated. A conjugate plane is obtained by inserting a telescope of two lenses. If the respective focal lengths of the lenses are $l_{f,1}$ and $l_{f,2}$ and they are separated at a distance $l_{f,1}+ l_{f,2}$, one finds the conjugate plane

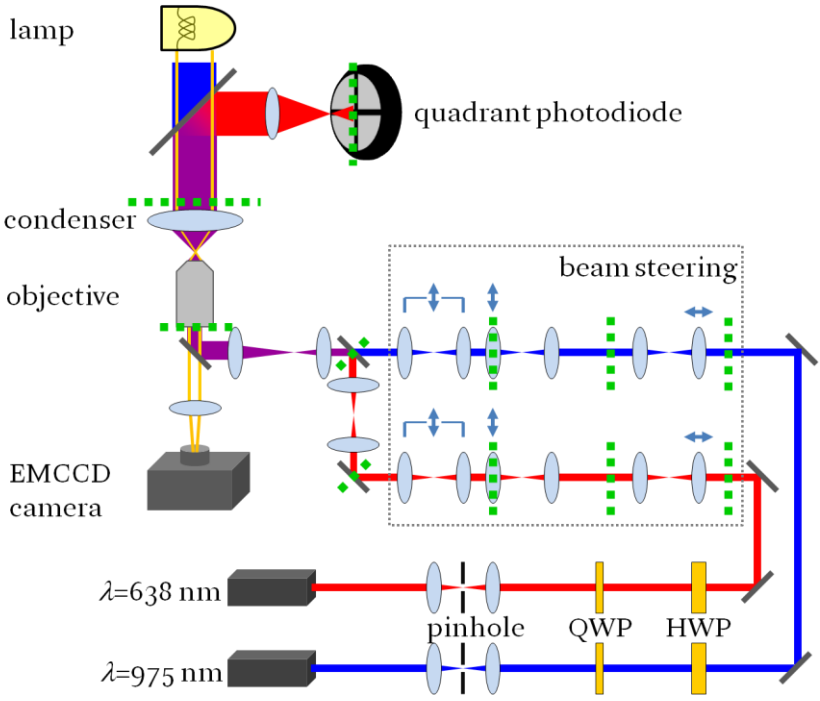

Figure 3-9: Schematic representation of the optical tweezers setup. Two laser beams, a trapping and detection laser, are focused by a microscope objective. Green dotted lines give conjugate planes to the back focal plane of the objective, which are used for beam steering and back focal plane interferometry. The sample is additionally imaged on a EM-CCD camera.

separated at a distance $2l_{f,1}+2l_{f,2}$ from the back focal plane. The exact position of the lens pair is not crucial, as long as they both are in between the two conjugate planes. By inserting multiple telescopes, additional conjugate planes are accomplished.

Figure 3-10 also presents the practical realization of the beam manipulation. Each transformation is obtained by moving one or two lenses of a telescope. The two lenses are chosen to have the same focal length l_f. When using a telescope for beam manipulation, its position with respect to the conjugate planes is of importance.

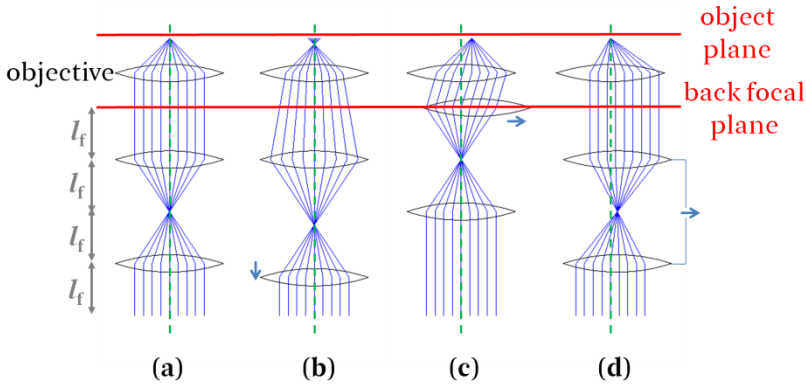

Figure 3-10: Beam steering using a telescope consisting of two lenses with the same focal length. Depending on the position of the telescope with respect to the back focal plane of the objective (or a plane conjugate to it), different beam manipulations can be realized. An axial movement of the laser focus with respect to the microscope object plane (b) is obtained by an axial translation of one of the telescope lenses. A lateral translation of one of the telescope lenses causes a lateral movement of the laser focus in the object plane (c). The focused laser beam can be tilted with respect to the objective axis (d) by a simultaneous lateral translation of the two telescope lenses.

1. Axial movement of the laser focus is realized by placing the telescope lenses in the middle between the two conjugate planes. By moving the rearmost lens towards the back focal plane over a distance d_{ax}, the beam collimation at the back focal plane is altered and the laser focus shifts away from the objective lens over a distance $nl_{f,obj}^2 d_{ax} / l_f^2$ with n the refractive index of the immersion oil and $l_{f,obj}$ the objective focal length.
2. By positioning the telescope lenses such that the lens closest to the objective lens coincides with the back focal plane of this objective and moving this lens laterally over a distance d_{lat}, a tilt of the laser beam is created at the back focal plane of the microscope objective. This makes for a lateral shift of the laser focus a distance $l_{f,obj} d_{lat} / l_f$ in the object plane.
3. By again positioning the telescope in the middle between the objective's back focal plane and its conjugate plane and moving both lenses laterally over a distance d_{lat}, the incoming beam is parallel but off-axis at the back focal plane of the objective. This makes that the beam is rotated over a (paraxial) angle of $2d_{lat} / \left(n_{oil} l_{f,obj} \right)$ in the plane of the lateral lens movement.

As can be seen in Figure 3-9, these beam steering functionalities are integrated sequentially in the optical setup by realizing multiple conjugates to the back focal plane.

b. EM-CCD image: particle position control

The microscope image obtained by the CCD camera is used in two ways. Firstly, based on the image one can ensure only one particle is confined within the optical tweezers. If during the course of an experiment a second particle or an impurity in the liquid is seen to be trapped by the tweezers, the experiment is aborted.

Secondly, the microscope image is used to precisely know and control the position of a particle with respect to the bottom substrate of the

cell it is measured in. Controlling a particle's position inside the measurement chamber is necessary to achieve reproducible results with an OTE-setup. For example, in section 2.2.1 it was shown that a large enough separation between the particle and the bottom substrate is needed to make hydrodynamic coupling between the two negligible. Furthermore it will be shown in the following subsection and in the next chapters that the particle position also determines the properties of the optical trap it is confined in or should be taken into account when determining the particle's electrical properties.

The microscope image is used to control the particle since it is very sensitive to the position of the laser trap and particle with respect to the bottom substrate. Firstly, the reflection of both the trapping and detection laser from this substrate depends on where the substrate is located in the laser beam. Secondly, the laser light back-scattered by the particle interferes with this reflected light, which provides a measure for the particle-substrate separation. As a reference, three images of the same optically trapped particle at different positions with respect to the bottom substrate are given in Figure 3-11.

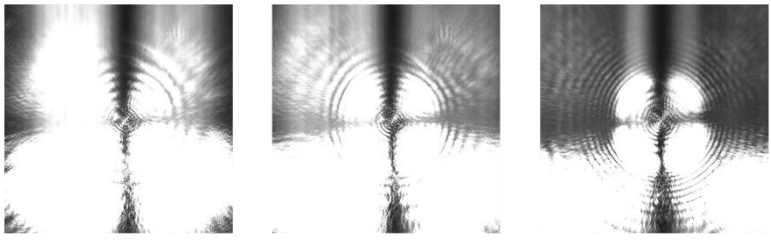

Figure 3-11: Microscope image of a single optically tweezed particle separated 2.1 µm (a), 7.3 µm (b) and 11.3 µm (c) from the bottom substrate. The image consists of an interference pattern generated by the laser light that is reflected at the bottom substrate and laser light that is backscattered from the particle. The resulting pattern depends strongly on the separation between the particle and bottom substrate.

The particle position is controlled by setting the axial position of the microscope objective based on a comparison of the live image with a set of reference images. Before an experiment this reference set is built by recording the back-scatter pattern of the particle at different positions of the objective, which is typically translated in steps of 100 nm along its axis. From these images the intensity of about 2000 pixels is extracted and these values form a reference set against which the particle-substrate separation can be compared. During the experiment an intensity profile is obtained by extracting the same pixels from the live image. The actual position of the particle is then determined by finding the least square error between the extracted pixels and the reference set. From this position estimate the microscope objective is translated such that the aimed separation between the particle and bottom substrate is obtained.

c. Spherical aberration of the laser focus

The experiments described in this dissertation are carried out with an oil-immersion objective. This immersion fluid is necessary to achieve a large numerical aperture of the laser beam, and thus a narrow focus that can act as an optical trap. The substrate can be considered index-matched to the immersion oil which has a refractive index $n_{oil} = n_{substrate} = 1.545$. The continuous medium, i.e. an aqueous solution with refractive index $n_{water} = 1.33$, is not index-matched. This causes refraction of the laser beam at the interface. This has several implications on the performance of the optical tweezers. Firstly, the refraction at the interface implies that the (paraxial) focus plane lies closer to the substrate compared to when an index-matched solution is used (see Figure 3-12). This makes that a translation of the objective over a distance d_{trans} results in a translation of the object plane by a distance $d_{trans} n_{water}/n_{oil} \approx 0.86 d_{trans}$.

Secondly, the difference in refractive index between the immersion oil and the aqueous solution results in spherical aberration of the laser focus. This spherical aberration is a direct result of the refraction of the laser beam at the substrate-water interface. Oil-immersion

objectives create an aberration-free laser focus in an index-matched medium. From a ray optics point-of-view this implies all rays of the light beam are concentrated in the focal point of the microscope objective, as is depicted in Figure 3-12 (a). When a medium with lower refractive index is introduced, all rays will refract according to Snell's law: the ratio of the sine of the angles of incidence and refraction equals the ratio of the refractive index of the second and first medium. This makes that marginal rays are focused below the paraxial focus plane, as indicated in Figure 3-12 (b). This makes for an aberrated focus which decreases the performance of the optical tweezers: the laser focus is spread out mainly in the axial direction, which lowers the axial trapping stiffness.

The spherical aberration of the laser focus gets larger when more distance is traveled by the laser beam in the lower index medium. This is demonstrated in Figure 3-13 which presents the axial trapping stiffness of a 1 μm polystyrene particle as a function of the distance from the bottom substrate. The stiffness decreases significantly from a certain separation onwards and approaches zero at a distance of 22 μm. When, from this point, the particle-substrate separation is further increased, the tweezers are not able to hold the particle and it is pushed outside the laser focus due to radiation pressure. The working range of the previously described optical tweezers holding a 1 μm particle is thus in the range of 20 μm above the bottom substrate.

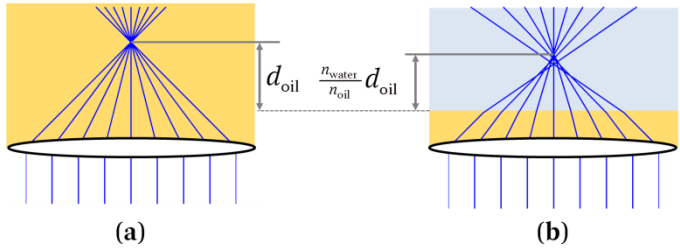

Figure 3-12: The effect of using an aqueous medium in combination with an oil immersion objective. When an index matched medium is used (yellow, figure (a)), the laser is perfectly focused. The aqueous medium (blue, figure (b)) causes refraction of the laser beam, resulting in an axial shift of the laser focus. Moreover, spherical aberration of the beam focus occurs because marginal rays are refracted over a larger angle than rays close to the beam axis.

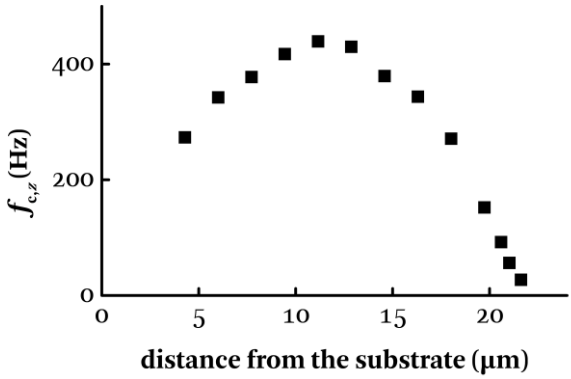

Figure 3-13: The change in corner frequency along the axial direction as a function of the distance to the bottom substrate. Because of spherical aberrations introduced by the refraction of the laser beam at the substrate-liquid interface, the trap stiffness and hence the corner frequency decreases from a certain separation onwards. The spherical aberration limits the trapping distance to about 22 µm above the substrate for 1 µm polystyrene particles.

3.3.2 Microfluidics

Two types of mobility measurements are discussed in this dissertation. Firstly, steady-state mobility measurements provide a single value for the electrophoretic mobility of one or more particles. These particles have been incubated for some time in order to equilibrate all physicochemical processes at the particle surface. A second type of experiments consists of measuring how the mobility of a single particle varies in function of time when e.g. the chemical composition of the suspending liquid is changed. This allows for the monitoring of chemical or physical processes at the particle-liquid interface that influence the particle mobility. Each of these experiments uses dedicated microfluidics to which the necessary functionalities, such as electric field generation and fluid pumping, are added. This subsection provides a detailed overview of the used devices.

a. Steady-state measurements

Steady-state measurements are performed using commercially available IBIDI-slides [107]. The bottom substrate of 180 µm thickness is built out of a hydrophobic polymer with optimized optical properties to allow for advanced microscopy techniques. One slide, as is schematically presented in Figure 3-14, contains six identical microchannels with a height of 400 µm and width of 3.8 mm. The inlet and outlet consist of cylindrical wells of 4 mm diameter and are separated by 17 mm.

An electric field is generated inside these channels by applying a voltage difference across platinum wires inserted in both the inlet and outlet. To characterize the electric field inside the microchannel, a finite element simulation of the electric fields and currents inside the above described geometry is obtained with COMSOL making use of the *Electric Currents* package. The stationary 3D-simulation considers the water inside the microchannel as a conductor and the polymer forming the microchannel as an electrical insulator. The wires are defined as equipotential lines at the axis of the cylinder that makes up

the inlet or outlet. Figure 3-15 gives the electric field magnitude along an *xy*-cross section at 200 µm from the bottom substrate when a DC potential difference of 1 V is applied between the electrodes. It is seen that the electric field magnitude can be considered constant far enough from the inlet and outlet. The calculated field magnitude corresponds with the electric field magnitude between two parallel plates at a potential difference of 1 V placed 15.6 mm apart. Figure 3-15 also indicates the direction of the electric field in this cross section. From this figure and from the numerical simulation it is seen the electric field is homogeneous near the middle of the channel and is oriented along the channel direction.

b. Dynamic mobility measurements

In order to change the chemical composition of the suspending buffer, a flow cell is fabricated consisting of a Y-junction that has two inlet channels that merge into one outlet channel (Figure 3-16). The top substrate consists of a conventional microscopy slide of 1.1 mm thickness in which two inlet and one outlet openings have been drilled. To generate an electric field inside the channel, two thin-film chromium electrodes are deposited by e-beam physical vapor deposition (PVD). The flow cell is fabricated by patterning UV curable glue (Norland NOA 68), containing spacers of 75 µm, with a computer controlled glue dispenser onto the microscope slide and sealed with a No 1.5 microscopy cover slip.

The maximal flow rate in the microfluidic device is inherently limited by the strength of the optical tweezers holding a particle: the fluid velocity results in a drag force on the particle, which can push the particle outside the linear range of the optical tweezers. For a maximal displacement of 100 nm, a 1 µm particle can be subjected to a fluid velocity up to 500 µm/s. The associated flow rate of 0.1 mm^3/s is difficult to achieve with conventional pumping systems such as a syringe pump. Instead, a pumping mechanism based on the principle of communicating vessels is used. For this system PTFE-tubing is

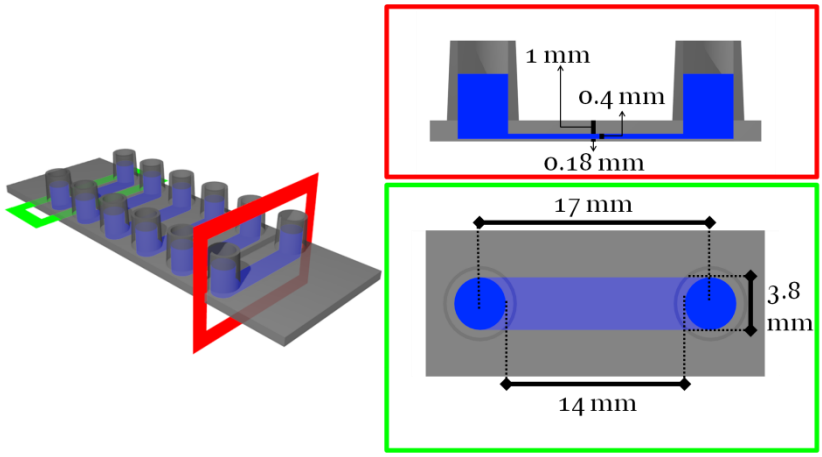

Figure 3-14: Schematic representation of the IBIDI-microchannels used for steady-state measurements. The two cross sections (red and green) provide the dimensions of the channel. For an OTE experiments, a platinum wire is inserted in both the inlet and outlet, which functions as an electrode.

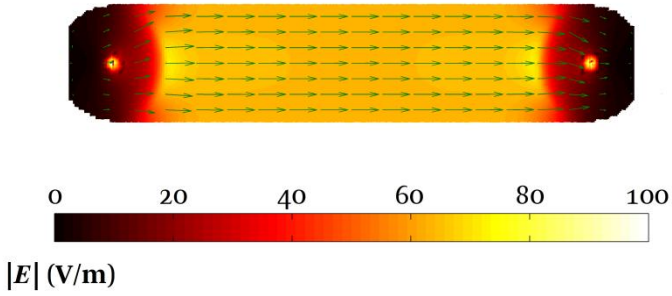

Figure 3-15: Finite element simulation of the electric field inside an IBIDI microchannel. A potential difference of 1 V is applied across two wires inserted in the inlet and outlet of the channel. Presented is a cross section along the *xy*-plane in the middle of the channel. The arrows represent the electric field vector and the colors indicate the field magnitude. Far enough from the inlet and outlet, the electric field can be considered homogeneous and directed along *x*.

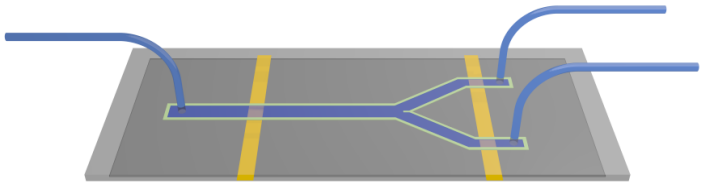

Figure 3-16: Schematic representation of the flow cell which is defined by a glue pattern on top of a substrate on which two chromium electrodes (yellow) have been evaporated by PVD. PTFE tubing inserts liquid at the two inlets of the device (right). The channels merge, and due to the laminar flow characteristics the two liquid streams remain separated. This allows to bring a particle from one buffer to another. The liquids exit the device via an outlet tubing (right).

attached to the openings of the microfluidic device. The other end of each tube is submerged in liquid contained by a vial. Depending on the level inside the three vials, a pressure difference across the channel can be obtained. To obtain a unidirectional flow from inlet to outlet, the levels of both inlet solutions are chosen equal, ensuring the same flow rate in both inlet channels, and the level of the outlet solution is chosen to be lower. The flow rate and thus the fluid velocity can be regulated by adjusting the level difference between the inlet and outlet liquid level. Through each inlet opening a different solution is pumped into the flow cell. Because the flow inside the microfluidic cell is laminar, the two liquids are not mixed at the junction and therefore flow next to each other, creating a boundary through which a particle can move from one medium to another. The sharpness of this boundary is limited: when there exists a concentration difference of certain species between the two liquids, diffusion of this species occurs and this broadens the boundary. Obviously, the boundary is broader further downstream of the junction. For typical flow rates (100 µm/s) and small ions (e.g. K^+), the boundary width is in the order of 1 mm at the outlet.

3.4 Conclusions

In this chapter the working principle behind optical tweezers was explained. This was done in an analytical way for very large or very small particles compared to the laser wavelength; these are the geometric optics and Rayleigh approximation, respectively. To quantify forces for particles of arbitrary size, a numerical calculation based on generalized Lorentz-Mie scattering theory was performed, showing qualitative agreement with the approximations in their respective regimes. It was seen, both from this calculation as from experiments, that the particle inside optical tweezers can be considered to be confined in a harmonic potential well, providing a Hookean restoring force of the tweezers determined by the trap stiffness k_{trap} which is, in general, anisotropic. To quantify this stiffness, power spectrum analysis of the Brownian fluctuation of the particle inside the trap is used throughout this dissertation. These fluctuations are recorded via back focal plane interferometry and their power spectrum is described by a Lorentzian governed by two parameters: the corner frequency f_c, which is proportional to k_{trap}, and a conversion factor β relating the detector output signal to the physical displacement of the particle. By using the size of the particle as a given numerical values for both k_{trap} and β can be obtained. It was furthermore shown that the knowledge of these two parameters allows determining the electrophoretic mobility of a particle moving inside an AC electric field. Two ways to retrieve this parameter from the positional signal were presented. Firstly, by power spectrum analysis the oscillation amplitude is determined by establishing the distance between the data point in the experimental power spectrum at the applied frequency and the Lorentzian fit to the Brownian spectrum. The second method uses phase information of the oscillation to obtain the oscillation amplitude for the harmonic forces on the particle that are in phase with the applied field. Since the electrophoretic force is in phase with the applied field, also this method retrieves the oscillation amplitude, provided no other harmonic forces that are out-of-phase are present.

The second part of the chapter elaborated on the practical implementation of the previously discussed concepts. The optical setup was described in detail, including the steering optics used to provide manipulation of the focused laser beam that makes up the optical tweezers. Also a position control algorithm based on the microscope image containing the back-scattered and reflected laser light was explained, which allows to maintain the same particle-substrate separation throughout an experiment. Finally details were provided about the two types of microfluidic devices used in the experiments discussed in the following chapters.

Chapter 4
Temperature monitoring

4.1 Introduction

Microfluidic devices find applications in a variety of fields, including diagnostics, drug discovery and water quality monitoring. Typically, additional functionalities besides fluid handling are integrated in these devices to increase their performance. Examples include sample injection, sorting of species, fluid mixing and detection of certain targets. The combination of these functionalities results in completely integrated systems called Lab-on-a-chip (LoC) devices that can perform a chemical, biochemical or biological analysis on a sample in an automated fashion. Compared to traditional laboratory techniques, these LoC systems promise fast read-out with increased sensitivity at a lower cost [22], [108], [109].

The performance of these LoC systems may be seriously affected by heating effects taking place inside the device because of the integration of these functionalities. For example, microfluidic devices that use pumping by electric fields often suffer from reduced performance due to Joule heating [110]. Also, when thermosensitive species are used, local heating effects may be detrimental for the envisioned application of the device [111]. On the other hand, induced heating may deliver new functionalities to a microfluidic device without overcomplicating its design and operation [112]. An example includes the realization of on-chip DNA-amplification via polymerase chain reaction, a biochemical process requiring a precisely controlled thermal cycling [113]. Also species separation and concentration by temperature gradient focusing resulting from Joule heating of an ionic liquid has been reported [114].

Thorough knowledge of the temperature profile inside microfluidic systems is crucial to understand the implication of heating processes on the functionality of these devices. There exist different experimental techniques to determine the temperature in a microfluidic device [115]. Often epi-fluorescence thermography is employed to visualize temperature differences along a microfluidic channel [116], [117]. In this technique, a thermosensitive dye is mixed

with the solution and the local temperature of the microfluidic device is assessed from the fluorescence intensity of this dye. Although it provides sensitive temperature measurements, the technique is difficult to use when the channel depth of the microfluidic device changes since the limited spatial resolution along the axis of the used microscope objective only allows for a an integration of the fluorescence intensity along the channel depth to retrieve the temperature profile. Total-internal-reflection fluorescence increases this axial resolution, but limits the measurement range to a few 100 nm from the bottom substrate of the microfluidic cell [118].

In this chapter I show how an optically tweezed particle can be used to probe the temperature inside a microfluidic device. Besides offering the capability of accurately positioning the temperature probe anywhere in the channel, this technique is also less invasive than dye-based techniques since only a single inert particle is used. Moreover, it offers a trivial way to monitor Joule heating in applications that combine optical tweezers with electrophoresis.

The aim of this chapter is to evaluate heating phenomena occurring in a typical OTE experiment. Both Joule heating, resulting from the application of the external electric field, and heating due to laser light absorption are discussed. Parts of this chapter, mainly the above introduction and the sections on measurement procedure and Joule heating, are based on [119].

4.2 Measurement procedure

The calibration of optical tweezers uses two parameters to fit a Lorentzian to the power spectrum of the QPD output voltages: the corner frequency f_c of the trapped particle, which is proportional to the ratio of the trap stiffness k_{trap} and the drag coefficient γ of the particle, and the particle's diffusion coefficient in units of V^2/s. Both parameters are temperature dependent. This is mainly due to the temperature dependence of the viscosity of the suspending liquid: at higher temperatures the viscosity of aqueous solutions decreases significantly. A decreased viscosity results in a smaller drag coefficient of the particle. Hence the corner frequency of the trap is expected to increase when the temperature of the surrounding medium rises. The diffusion coefficient is also expected to increase as can be seen from its temperature dependence in equation (2.19).

The temperature dependence of these parameters provides a method to quantitatively determine the temperature increase inside a microfluidic device compared to a reference measurement. More precisely, when the same particle is measured under the same conditions except for the temperature of the surrounding liquid, the ratio between the two corner frequencies $f_{c,1}$ and $f_{c,2}$ is a function solely of liquid viscosity at both temperatures:

$$\frac{f_{c,1}}{f_{c,2}} = \frac{\eta_2}{\eta_1}. \tag{4.1}$$

A similar relation can be obtained by taking the ratio of the two diffusion coefficients:

$$\frac{D_1}{D_2} = \frac{T_1\eta_2}{T_2\eta_1}. \tag{4.2}$$

These ratios can be converted to expressions which are function of only the temperature by considering the temperature dependence of the viscosity. For this the empirical equation obtained by Kestin *et al.*

that approximates the viscosity of water in function of the temperature can be used [120]. The equation, altered to comply with the Kelvin-scale and room temperature conditions η = 1.002 mPa s at T = 293.2 K, reads

$$\log_{10}\left(\frac{\eta}{1.002\,\text{mPa s}}\right)=-\frac{\left(T+549.6\,\text{K}\right)}{\left(T-177.2\,\text{K}\right)}\frac{\left(T-293.2\,\text{K}\right)}{681.7\,\text{K}}. \qquad (4.3)$$

From this expression, equations (4.1) or (4.2) can be expressed as a function of the temperatures T_1 and T_2. When one of these two temperatures is known, e.g. if one measurement is done with the liquid at room temperature, the temperature difference is obtained explicitly via these equations.

It should be noted that relation (4.1) holds under the assumption of temperature-independent trapping stiffness of the tweezed particle. A change in temperate does however affect the refractive index of both the liquid and the particle. Since the trapping stiffness depends on the refractive index difference of both materials, it cannot be considered temperature-independent *a priori*. The temperature-induced refractive index change of water is approximately -10×10^{-5} RIU/K at wavelengths around 1000 nm [121]. Values for the refractive index change of polystyrene vary according to the consulted sources, but are typically between -5×10^{-5} and -15×10^{-5} RIU/K (e.g. [122]). This makes that the index difference between the two materials changes in the order of 10^{-3} RIU, or 0.5 %, over a temperature range of 20 K. A similar relative change is expected in the trap stiffness. This change in trap stiffness is however insignificant compared to the viscosity change of water over the temperature interval from 294.2 K (room temperature) to 314.2 K, i.e. 42 %. The presumption of constant trapping stiffness is therefore reasonable.

The power spectrum analysis program used to estimate f_c and D also provides values for the standard deviation on the estimates of these

parameters, i.e. σ_{f_c} and σ_D, respectively. Linear error propagation provides expressions for the error on the estimate of the temperature, assuming the temperature T_1 and thus the viscosity η_1 are known exactly. For equation (4.1) and (4.2) one respectively calculates:

$$\sigma_{T_2}^2 = \left(\frac{\partial T}{\partial f_{c,1}} \right)^2 \sigma_{f_{c,1}}^2 + \left(\frac{\partial T}{\partial f_{c,2}} \right)^2 \sigma_{f_{c,2}}^2 , \tag{4.4}$$

$$\sigma_{T_2}^2 = \left(\frac{\partial T}{\partial D_1} \right)^2 \sigma_{D_1}^2 + \left(\frac{\partial T}{\partial D_2} \right)^2 \sigma_{D_2}^2 . \tag{4.5}$$

The partial derivatives in equation (4.4) can be calculated directly from a closed expression for the temperature as a function of the two corner frequencies, obtained by combining equations (4.1) and (4.3). The same approach is not possible for the derivatives in (4.5) since equation (4.2) cannot be solved for T_2 in closed form. Instead the partial derivatives are obtained by differentiating both sides of equation (4.2) with respect to D_1 and D_2 and solving the resulting equations for $\partial T/\partial D_1$ and $\partial T/\partial D_2$, respectively.

4.3 Joule heating

Microfluidic systems often use electric fields in combination with electrolyte solutions. Electrophoresis, for example, is used as a technique to separate chemical species based on their charge [123]. Other devices make use of electric field gradients to separate, trap or transport micro-and nano-objects based on their polarizability properties, a physical phenomenon known as dielectrophoresis [124]. The presence of an electric field in an electrolyte solution generates currents, resulting in power dissipation under the form of Joule heating.

In this subsection power spectrum analysis of an optically tweezed particle is employed to quantify the temperature increase due to Joule heating inside a microfluidic device. The power dissipation is generated by applying a homogeneous alternating electric field inside the microchannel. After a detailed discussion of the measurement procedure and the temperature effects on the test cell, this subsection continues with the discussion of two types of experiments: steady-state and time resolved temperature measurements.

4.3.1 Measurement procedure

Polystyrene microspheres of 1 μm diameter are suspended at a mass fraction of 5 μg/l in an aqueous solution containing KCl concentrations ranging from 5 g/l to 35 g/l. The addition of KCl to the solution at these concentrations does not influence the viscosity of the liquid significantly [125]. A single particle is optically trapped and its thermal fluctuations inside the optical tweezers are measured at room temperature T_o = 294.2 K for 15 seconds. From this measurement the reference corner frequency $f_{c,o}$ and diffusion coefficient D_o at room temperature are obtained. To induce Joule heating, a sinusoidal voltage (frequency 1000 Hz) is applied across the channel. Again, the particle position is recorded and from the position power spectrum new values for the corner frequency f_c and

the diffusion coefficient D are obtained. The temperature increase is determined using equation (4.1) and (4.2), respectively.

For the steady-state measurements the thermal fluctuations of the particle are measured several minutes after turning on the potential difference across the channel to allow transient heating effects to decay. The particle is then measured for 15 seconds. The time-resolved measurements on the other hand are used to measure the transient heating. In this case the particle position is measured at room temperature to establish the reference values $f_{c,0}$ and D_0. After this a voltage step across the channel is applied and the Brownian fluctuations of the particle in the optical trap are continuously measured and f_c and D are calculated as a function of time, from which the temperature is retrieved as described above.

4.3.2 Microfluidic device

In all measurements IBIDI-slides, described in section 3.3.2a. , containing 6 individual microchannels are used. The electric field is generated by applying a sinusoidal potential difference across two platinum wires inserted in the inlet and outlet of the channel. The electrical resistance of these microchannels is a function of both the salt concentration and the temperature of the solution. The electrical resistance R_0 at room temperature T_0 = 294.2 K is measured for all concentrations by means of an impedance measurement (Hewlett Packard 4274A Multi-Frequency LCR Meter). R_0 is inversely proportional to the salt concentration of the solution, as can be seen from the data presented in Figure 4-1. When the temperature of the solution rises, the viscosity of water goes down. This makes that the mobility of the dissolved ions increases and the conductivity of the solution increases as well. For most electrolytes the conductivity can be considered to increase approximately proportional to the temperature in a range of 20 K [126]. This makes that the temperature dependence of the electrical resistance of the microchannel may be written as

$$R(T) = \frac{R_0}{1 + \theta\left(T - T_0\right)}, \tag{4.6}$$

where the temperature coefficient θ of the electrolyte solution is approximately 0.020 K^{-1}, as provided in literature [127]. Knowing the applied voltage and the electrical resistance of the microchannel, the dissipated power is given by

$$P = \frac{V_{RMS}^2}{R}. \tag{4.7}$$

When large powers are dissipated in the IBIDI channel, a deformation of this channel occurs. More precisely, when applying an AC voltage step, the bottom substrate of the cell is observed to move with respect to the objective. This observation is done via the reflection of a focused laser on the interface of this substrate with the liquid inside the channel. Since the reflection pattern depends strongly on the exact position of the substrate in the laser beam, the substrate movement can be quantified: by first recording a set of reference reflection patterns at different axial positions of the objective (see also paragraph 3.3.1b.) the change in separation between the objective and the bottom substrate due to the applied voltage step can be evaluated. Figure 4-2 (a) and (b) depict the axial displacement of the bottom substrate in the middle of the microfluidic channel when turning on and off, respectively, an AC voltage across an IBIDI channel containing a solution of 30 g/l KCl. When applying the voltage step, the substrate is observed to firstly move towards the objective during a time interval of about 10 seconds, after which it relaxes back during 100 seconds to an equilibrium position which almost coincides with the original position of the substrate. The maximal displacement increases significantly with the applied RMS-voltage. When removing the voltage the opposite channel deformation is observed: the substrate first moves away from the

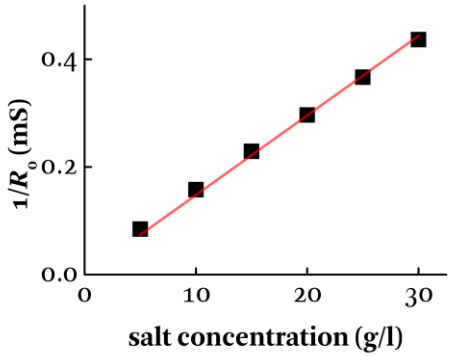

Figure 4-1: The electrical resistance of a microchannel at room temperature is inversely proportional to the salt concentration of the liquid it contains (R-squared equals 0.9962)

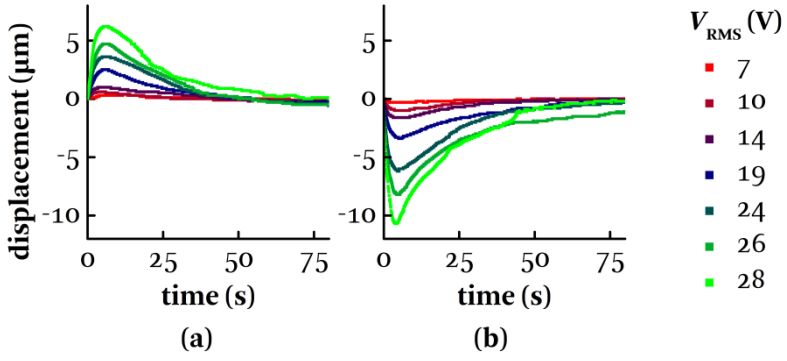

Figure 4-2: The displacement of the bottom substrate when an AC voltage is (a) applied and (b) removed across the channel. A negative displacement corresponds with the substrate moving towards the objective.

objective and then relaxes back to its original location. The time scale at which this process happens is comparable with the time scale of Figure 4-2 (a).

This deformation is attributed to the thermal expansion of the polymer substrate. When applying the voltage step, Joule heating in the liquid causes the temperature of the substrate to increase as a function of time. An asymmetric thermal expansion causes strain and leads to the bending of the slide, which moves the bottom substrate towards the objective. When the top substrate reaches an equilibrium temperature, its thermal expansion relieves the thermal strain after which the bottom substrate relaxes back to its original position, explaining the behavior seen in Figure 4-2.

4.3.3 Steady-state measurements

Figure 4-3 shows two representative power spectra of the position signal of the same optically trapped particle recorded both with and without an RMS voltage of 25 V applied across the microfluidic channel. The particle is suspended in an aqueous medium with a KCl concentration of 30 g/l and is held 6 μm above the bottom substrate of the microchamber to minimize the hydrodynamic coupling with this substrate. The application of a potential difference across the electrodes in the inlet and outlet of the device results in power dissipation inside the microchannel. This dissipation causes an increase of the temperature of the liquid and hence affects the recorded power spectrum. The change of both corner frequency and diffusion coefficient can be readily observed from the presented plot. From the graph it is seen that the corner frequency increases when Joule heating occurs inside the microfluidic channel. This agrees with equation (4.1): the corner frequency is inversely proportional to the viscosity. Since the viscosity decreases at higher temperatures, the corner frequency is expected to increase. The spectra presented in Figure 4-3 furthermore indicate that the diffusion coefficient increases when the temperature of the surrounding medium increases due to power dissipation: as can be seen from equation

(3.11), at frequencies much higher than the corner frequency the Lorentzian fit to the power spectrum is approximated by $2\beta D/(2\pi f)^2$. The shift of the Lorentzian at these frequencies thus indicates an increase in diffusion coefficient, provided that the conversion factor β between voltage output of the QPD and position of the particle remains unaltered. The increase of the diffusion coefficient at higher temperatures is in accordance with the temperature dependence given in equation (4.2). Furthermore, at frequencies much below the corner frequency, the power spectrum is approximated by $2\beta k_B T\gamma / k_{trap}^2$. The product γT is expected to decrease at higher temperatures, since the relative change in viscosity is higher than the change in absolute temperature. This explains why the power spectrum of a particle in a heated environment decreases at these frequencies compared to the power spectrum at room temperature.

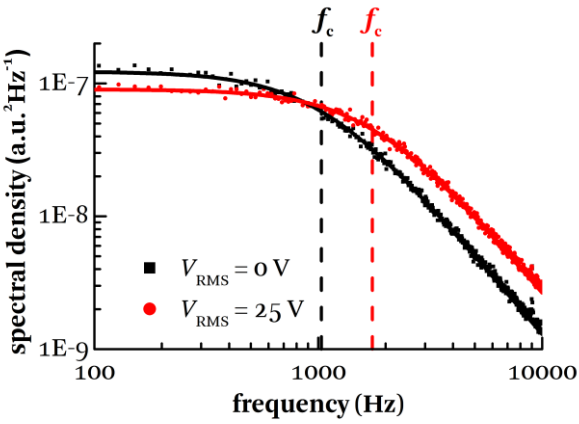

Figure 4-3: The power spectrum of a 1 µm polystyrene particle changes when power is dissipated inside the microfluidic channel. Both the corner frequency and the diffusion coefficient are observed to increase. This is due to Joule heating lowering increasing the temperature and decreasing the viscosity of the liquid.

Figure 4-4 (a) and (b) present the ratios $f_c/f_{c,0}$ and D/D_0, respectively, for a single particle, suspended in water containing 30 g/l KCl, as a function of the applied RMS-voltage. These data are presented for the two lateral (x,y) and the axial (z) spatial directions. In each of these directions both $f_c/f_{c,0}$ and $D/D_0$is observed to increase with the applied RMS voltage. However, there is a considerable mismatch between the values obtained from the separate spatial directions. The relative standard deviation on $f_c/f_{c,0}$ and D/D_0 between the three directions is measured to be 15% and 30%, respectively. This deviation is considerably higher than the expected errors obtained from equations (4.4) and (4.5): for all data points displayed on Figure 4-4 (a) and (b) σ_T is calculated to be between 0.5 % and 2 %.

Two causes can be proposed to explain this discrepancy. Firstly, as discussed before, a temperature increase changes the refractive index of both the liquid and the polymer of the microfluidic channel. When assuming that the polymer of the IBIDI-cell behaves similarly as most polymers, such as PMMA, polystyrene or polycarbonate, its refractive index will decrease at higher temperatures, similarly to water. A lower refractive index results in a collimation of a focused laser beam, an effect referred to as thermal lensing. This lensing is especially important for the detection beam which travels over more than 1 mm inside the device. The change in collimation may result in a significant change of the signal received by the QPD.

A second effect explaining the variation seen in these figures may be channel deformation due to thermal expansion of the polymer making up the microchannel, as discussed in the previous paragraph. As a result of this deformation, a slight displacement of the detection laser beam with regard to the particle can occur. This displacement is observed firstly by means of image analysis of the EM-CCD image as presented in section 3.3.1b. : the microscope image consists of the back-scattered light of both the detection and trapping laser from the particle and the light reflected at the substrate-liquid interface of both lasers. The resulting interference pattern is sensitive to any

displacement of either the laser beams or the particle with respect to the substrate. During a measurement, the real-time image is compared against a stack of reference images taken before the voltage was applied by calculating the square error on the intensity of selected pixels. The minimal error obtained by this method is observed to increase when large power dissipation, associated with channel deformation, occurs. This indicates that the detection beam is indeed displaced with regard to the particle due to channel deformation. Secondly, the mean intensity of the detection laser light impinging on the QPD is also observed to increase with the applied RMS-voltage, as is presented on Figure 4-5: an increase of the mean intensity of 16 % is measured over the voltage range. This change in intensity is the result of the defocusing of the detection beam focus compared to the situation at room temperature due to the abovementioned thermal lensing and of the channel deformation. The estimate of the diffusion coefficient is directly dependent on the voltage output of the QPD and thus on the mean intensity incident on the detector. A varying mean intensity thus creates a systematic error, of which the effect is best seen in Figure 4-4 (b): it explains the large difference in the diffusion coefficient measured in the axial direction Z compared to the lateral directions X and Y. The estimate of the corner frequency on the other hand is not sensitive to changes in the light intensity on the QPD, since this frequency is solely determined by the time scale at which the particle moves inside the trap. The beam displacement may however contribute to cross-correlation between the three channels, which can result in an error up to 10% in the estimate of the corner frequency [101]. A temperature estimation using equation (4.1) thus proves to be more reliable than using relationship (4.2). Figure 4-4 (c) presents the temperature increase due to Joule heating corresponding with the data in Figure 4-4 (a).

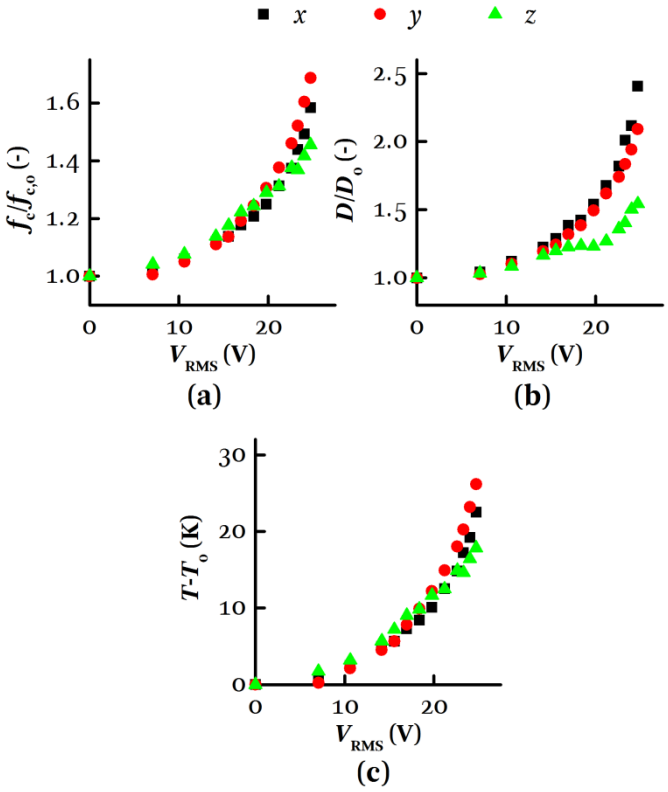

Figure 4-4: Power spectrum analysis is performed on the position data of an optically tweezed particle in a 30 g/l KCl solution for different applied RMS-voltages. The ratios $f_c/f_{c,o}$ (a) and D/D_o (b) are observed to increase for higher dissipated powers inside the channel in the two lateral (x,y) and axial (z) direction. The discrepancy on the values between the spatial directions is attributed to channel deformation. The ratio $f_c/f_{c,o}$ proves to be the best parameter to estimate the temperature increase inside the microchannel compared to room temperature T_o . The estimate of the temperature obtained with equation (4.1) is presented in (c).

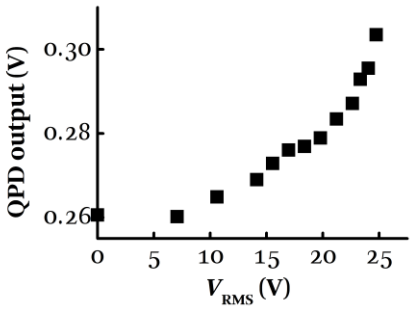

Figure 4-5: The mean total intensity impinging on the QPD increases as a function of dissipated power inside the channel. Plotted is the average signal for the z-position, i.e. the sum of the intensities on all four quadrants of the QPD. This increase in intensity is attributed to a displacement of the detection laser beam with respect to the particle as a result of thermal deformation of the microfluidic channel.

The dissipated power can be varied by either changing the applied voltage or altering the ionic strength of the solution in the microfluidic channel. Figure 4-6 presents the estimated temperature increase at a distance of 6 μm above the bottom substrate as a function of the dissipated power for mixtures containing a KCl concentration from 5 g/l up to 35 g/l and for various applied RMS-voltages. The power spectrum is recorded for one particle per solution and, for simplicity, only one of the lateral spatial dimensions is chosen for the analysis. The dissipated power is estimated from equation (4.7) taking into account the temperature dependency of the resistance as given by equation (4.6). From the figure it is observed that a linear relationship exists between the temperature and the dissipated power, as is expected in a thermal system in steady-state where cooling is mainly due to convection and conduction. A linear fit (R-squared equals 0.988) to the data points indicates the thermal resistance of the whole system to be 45 K/W. Moreover, the standard deviation of 0.9 K of the data to this fit provides an indication for the precision that is reached by measuring the temperature with this

method. This value is comparable with the accuracy reported with epi-fluorescence techniques [116]. However, due to the aforementioned channel deformation, a systematic error up to 15% can occur in the estimation of the temperature, limiting the accuracy of the method to 4 K at the highest dissipated powers presented in Figure 4-6.

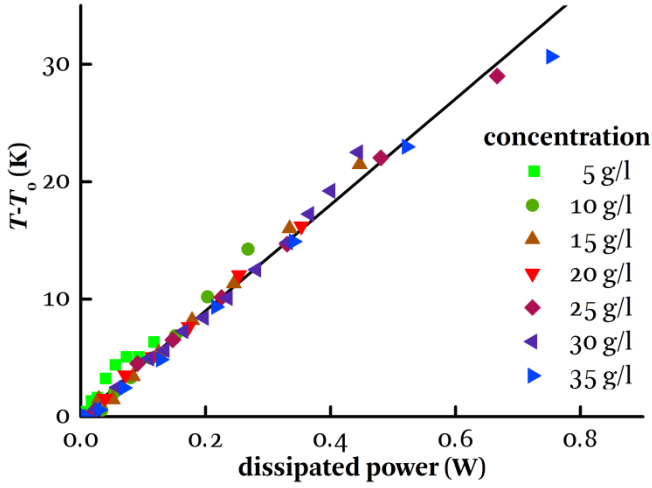

Figure 4-6: The temperature increase in a microfluidic device is observed to be proportional to the dissipated power in the channel. The dissipated power is varied by changing both the KCl concentration of the solution and the RMS-voltage applied across the channel. To calculate the dissipated power, the temperature dependence of the channel resistivity, as given by equation (4.6), is taken into account. The thermal resistance of the whole system is given by the slope of the linear fit to the data and is calculated as 45 K/W.

4.3.4 Time-resolved measurements

Observing the Brownian fluctuations of an optically tweezed particle furthermore allows for a characterization of transient heating phenomena occurring in the microfluidic device. For this, the position signal of the particle is split up in intervals of 1 s. Power spectrum analysis on each of these intervals establishes a value for the corner frequency at a 1 s time resolution. Reducing the time interval of a separate measurement, and thus the number of points for the power spectrum analysis, increases the error on the estimate of the corner frequency significantly. Therefore the corner frequency at room temperature is retrieved by averaging the corner frequencies retrieved over 50 intervals before the voltage step is applied, hence reducing the standard error on the estimate of $f_{c,0}$ to less than 1%. An estimate for the temperature in each interval is obtained by comparing the corner frequency of that interval with the corner frequency at room temperature, as presented in equation (4.1). Figure 4-7 shows the estimated temperature over 220 s inside the microfluidic channel containing 30 g/l KCl for three different voltage steps, each applied at time 0 s. The temperature variations are fitted to exponential functions $T(t) = T_{\Delta}\left(1 - \exp\left(t/\tau\right)\right)$. The best-fit values for the temperature increase T_{Δ} and the time constant τ are summarized in Table 4-1 and the fits are presented as solid lines in Figure 4-7. The expected spread for an individual measurement, i.e. the value $\pm\ \sigma_T$ calculated from equation (4.4) is represented by dashed lines. The time resolution that can be reached with this method is inherently limited by the error on the estimate of the corner frequency since σ_{f_c} increases as the measurement time t_{msr} decreases: $\sigma_{f_c} \propto 1/\sqrt{t_{msr}}$ [100].

Table 4-1: Best-fit values for the exponential fits to the time-resolved temperature increase presented in Figure 4-7.

V_{RMS} (V)	T_Δ (K)	τ (s)
21	10.8	13.3
25	16.9	15.8
28	25.5	16.8

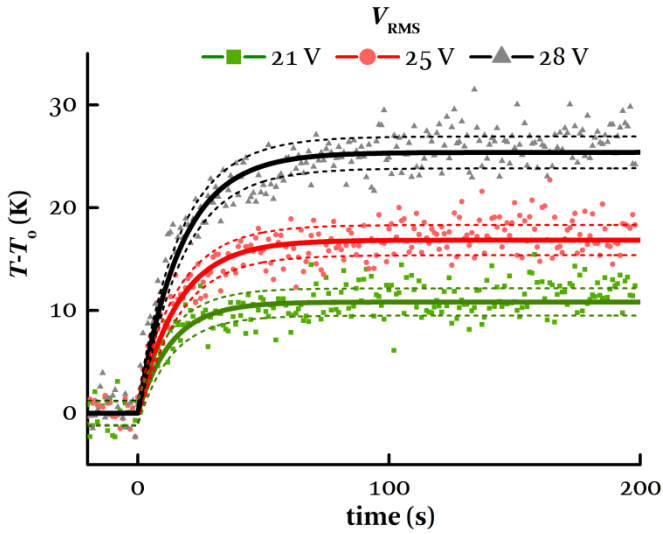

Figure 4-7: Transient heating is monitored by power spectrum analysis of the positional data on 1 s intervals. The temperature increase is fitted to an exponential function (solid lines). The spread of the individual temperature estimates around this fit results from the error on the estimate of the corner frequency and is seen to follow the theoretical spread (the dashed lines represent the $\pm\ \sigma_T$-band)

4.4 Photothermal effects

Experiments using optical tweezers are often prone to heating due to absorption of the laser light. The tight laser focus created by the high NA microscope objective can result in intensities of the order of 10 MW/cm². This can create a strong local heat source even when the material absorption is relatively low. Significant heating due to laser light absorption is especially detrimental in optical tweezers applications using biological samples such as cells or thermosensitive biomolecules. The subject of laser-induced heating caused by optical tweezers has therefore been mainly studied in the framework of these applications [128], [129].

A proper choice of laser wavelength is paramount to minimize heating due to light absorption. Figure 4-8 plots the electromagnetic absorption spectrum of liquid water for wavelengths spanning the UV until the IR. It is observed that a window of minimal absorption is present for visible wavelengths. However, many cellular organisms show strong absorption in this region, leading to sample damage when studied by optical tweezers [130]. This is why optical tweezers are typically equipped with NIR lasers, which do show increased absorption for water ($\alpha \approx 10-100\ \mathrm{m}^{-1}$) but allow for cell handling with limited photodamage [131].

Various studies exist that quantify the laser-induced heating by optical tweezers. Liu and coworkers have trapped sperm cells, ovary cells and liposomes in water and have measured the surrounding temperature by means of observing a shift in fluorescence spectrum of a thermosensitive dye, hence establishing a temperature increase of 10-15 K per watt of laser power at a wavelength of 1064 nm [128], [129]. Ebert *et al.* have used epi-fluorescence thermometry to monitor heating in a dual-beam optical trap. They found the heating in the center of the trap to reach 13 K/W [132]. Peterman and others have used power spectrum analysis of the Brownian fluctuations of

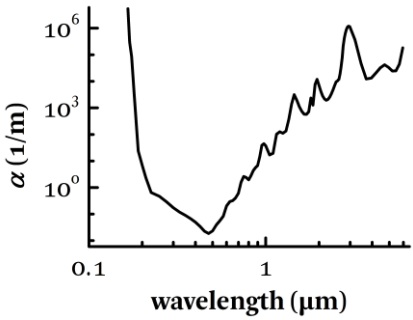

Figure 4-8: The absorption coefficient α of liquid water as a function of the wavelength of the electromagnetic radiation. Data retrieved from[133] .

optically trapped polystyrene and silica microspheres to monitor laser-induced heating in both water and glycerol [134]. Their experimental results indicate the heating results mainly from absorption by the liquid medium. In water they found a temperature increase of 8 K/W at 1064 nm wavelength. Moreover, their article reports on a theoretical model in support of their findings.

This section continues with a similar experiment as carried out by Peterman et al. to monitor any photothermal effects in the optical tweezers setup presented in Chapter 3.

4.4.1 Experimental procedure

A single polystyrene microparticle, suspended in a 1X DPBS buffer solution containing 0.2 wt% Tween20, is held by optical tweezers. The laser-induced temperature variations are observed by varying the power of the laser beam. Aside from the temperature increase due to absorption, also the trapping stiffness is changed by this variation in laser power. The corner frequency can be written as

$$f_c = f_{c,o} + \Delta f_c \,, \tag{4.8}$$

in which $f_{c,o}$ gives the corner frequency when no heating takes place

due to laser light absorption and Δf_c gives the increase in corner frequency due to a temperature increase. $f_{c,o}$ is considered proportional to the laser power P. The temperature increase due to light absorption changes the viscosity of the surrounding liquid. By again using relation (4.1), one writes

$$\frac{f_c}{P} = \frac{f_{c,o}}{P} \cdot \frac{\eta_o}{\eta(T)} . \tag{4.9}$$

In this equation $f_{c,o}/P$ is a constant which makes the variable f_c/P a function of only the changing viscosity due to laser-induced heating. A value for the viscosity at a specific temperature is obtained from equation (4.3).

4.4.2 Results

The black squares in Figure 4-9 represent the scaled corner frequency f_c/P measured for different laser powers. Note that the laser power is measured before the optical train, and a reduction of the total beam power of about 90 % is expected at the laser focus (see section 3.3.1). The measurement values can be considered constant within the margin of error on the estimate of the corner frequency. There is thus no significant increase of the scaled corner frequency to be observed, as would be expected in the case of laser-induced heating. As a reference, the figure also plots the expected increase in scaled corner frequency when the temperature of the liquid surrounding the particle would increase with 5 K over the laser power range. The measurements do not reflect such a trend, from which it is concluded that no significant heating occurs due to laser absorption. This is supported by the aforementioned values from literature for the laser-induced temperature increase. Taking into account the loss in beam power by the optical train, indeed a negligible heating is expected, i.e. less than 1 K at maximal beam power.

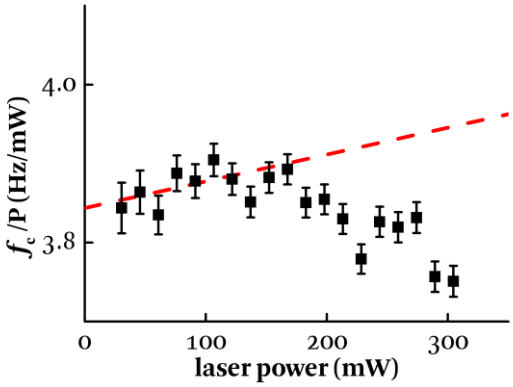

Figure 4-9: The variation of the scaled corner frequency f_c/P as a function of the laser power before the optical train of the optical tweezers setup. f_c/P appears constant within the margin of error. The red dashed line indicates the variation of f_c/P corresponding to a temperature increase of 5 K over the whole range.

4.5 Conclusions

In this chapter, I have investigated the heating effects that can appear during an OTE measurement. First a temperature measurement method was introduced. The method compares the Brownian motion of an optically trapped particle at a reference temperature with the Brownian motion of the same particle at a different temperature. From either of the two parameters determining the power spectrum of this position signal, i.e. the corner frequency and the particle's diffusion coefficient, the temperature can be calculated. The calculation based on the corner frequency appears to be most reliable, mainly as a result of the change in temperature directly influencing the detection laser and thereby the conversion factor which calibrates the output signal of the quadrant photo diode.

With this measurement method, the effect of Joule heating as a result of the applied AC electric field was examined. It was shown that at salt concentrations exceeding 1 g/l, significant heating (i.e. several Kelvins) is observed in an IBIDI-channel at applied RMS-voltages of a few 10 V. Moreover, with the method the time scale at which the heating in these devices occurs could be retrieved: transient heating was in the order of 20 seconds.

Secondly, the effect of heating due to laser absorption was considered. Measurements in which the laser power was altered did not reveal a significant temperature increase, even at the maximal laser power. This is in accordance with values for heating due to laser light absorption found in literature.

In this chapter it was furthermore discussed that this measurement method is potentially useful outside the scope of OTE experiments. Many Lab-on-a-Chip-devices use electric fields for fluid pumping or species separation. The use of these electric fields yields power dissipation under the form of Joule heating, which can affect the performance of the device. Alternatively, heat sources are often integrated in LoC systems to add specific functionalities. The

proposed method enables to monitor, locally and on a time-resolved manner, the heating taking place inside the device; a prerequisite to understand how heating phenomena influence the overall operation of the LoC-system.

Chapter 5
Electroosmosis

5.1 Introduction

Electroosmosis obtained its name from one of the early experiments in the field of colloid sciences [135]. In his 1809 paper, F.F. Reuss described an experiment in which a plug of clay was inserted into a U-shaped tube which he then filled with water. He observed that by applying a potential difference across electrodes put in both tube ends, the water level became imbalanced. Without the proper knowledge of how double layers form inside electrolytes in contact with charged surfaces, this observation was long unexplained and became known as electroosmosis. Now we know this imbalance is due to an electric-field-induced flow in the charged clay material but, despite having nothing to do with osmosis as such, the name stuck.

As a polar liquid comes into contact with a solid material, for example the clay in the above example or the wall of a microfluidic device in experiments described in this dissertation, the solid material typically acquires a net surface charge. As was described in section 2.3, a cloud of mobile ions, the electrical double layer, forms around this charged interface. Whenever an externally applied electric field has a component parallel to this charged interface it will cause the ions in the electrical double layer to move parallel to the surface. Because of viscous forces, the surrounding liquid is dragged along with these ions. This flow, the electroosmotic flow, extends well beyond the dimension of the electrical double layer, which typically extends over a few nanometers. The process is schematically represented in Figure 5-1.

Only an electric field is required to induce liquid flow by electroosmosis. Since electrodes are easily integrated in microfluidic systems, EOF is widely used for various aspects of on-chip fluid manipulation. For example, when a DC electric field is applied across a microchannel the resulting EOF flow profile is plug-like, i.e. the flow velocity is constant across the cross section of the channel. This makes EOF an attractive pumping mechanism in Lab-on-a-Chip devices [136]. When AC electric fields are used instead, on-chip micro

mixers can be established [137]. Besides applications in microfluidics, electroosmosis is exploited extensively for dewatering sludge and soils [138] and even promises a next generation of electrokinetic displays [139].

In this chapter it is investigated how electrically induced fluid flow, known as electroosmotic flow (EOF), affects the mobility measurements of particles in a typical optical trapping electrophoresis experiment and how these effects can be compensated for. I continue this chapter with a quantitative description of EOF in a microchannel induced by a time-dependent electric field. These theoretical results are then used to obtain a calibration method which compensates for EOF-effects when performing mobility measurements with optical trapping electrophoresis. The chapter concludes by showing how this calibration method can be employed as a probe for the electrical properties of the surfaces of a microfluidic device.

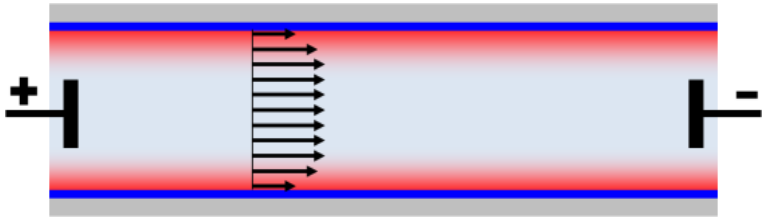

Figure 5-1: Electroosmotic flow (black arrows) results when an electric field is applied parallel to a solid-liquid interface carrying a net negative charge (blue). A cloud of mobile positive counterions (red), the electrical double layer, forms adjacent to this charged interface. These ions drift parallel to the surface as a result of the applied electric field and drag along the fluid well beyond the dimensions of the electrical double layer.

5.2 Electroosmotic flow in a microchannel

The description of electroosmotic flow induced by a DC electric field is well established [33], [36]. On the other hand, the literature on AC induced EOF is scarcer and therefore it is covered in this section. More specifically, after introducing the differential equations governing the physics behind EOF, this section describes AC induced EOF between two parallel plates. This parallel-plate geometry approximates the used microfluidic devices in this dissertation and allows for a closed form solution to the differential equations. Other authors have considered different geometries, e.g. cylindrical capillaries [140], or have provided semi-analytical solutions of AC-EOF in rectangular channels [141]–[143] or solution methods for the description in channels with an arbitrary cross section [144].

5.2.1 Governing equations

The flow of a continuous medium inside a channel is described by the Navier-Stokes equations. By using continuum mechanics, it relates the change in momentum of an infinitesimal fluid element to the forces acting on this element. These forces consist of the force resulting from a pressure gradient across the fluid element, friction forces, associated with the viscosity of the fluid, and external forces. In general, the fluid velocity is expressed by the Navier-Stokes equation by a non-linear time-dependent differential equation. In microfluidic channels some approximations can be made. Most importantly, convection is neglected, which implies linearization of the differential equation. In this simplified form, the equation reads:

$$\rho_{\mathrm{m}} \frac{\partial}{\partial t}\mathbf{v} = -\nabla p + \eta \nabla^2 \mathbf{v} + \mathbf{f}_{\mathrm{ext}} . \tag{5.1}$$

In the case of electroosmosis, the external force on the liquid results from the interaction of the external electric field $\mathbf{E}$ with the free ions in the electrical double layer. Using the Poisson equation to relate the

ion distribution with the electric potential ψ inside the double layer, the force is expressed as:

$$\mathbf{f}_{ext} = -\varepsilon \nabla^2 \psi \mathbf{E} \,. \tag{5.2}$$

In section 2.3 the properties of the electrical double layer were described and an expression for $\nabla^2\psi$ was retrieved. In the case of small enough surface potentials, i.e. $|\psi| < k_B T/e$, the Debye-Hückel approximation of the Poisson-Boltzmann equation provides a linear differential equation describing ψ (duplication of equation (2.26)):

$$\nabla^2 \psi = \kappa^2 \psi \,. \tag{5.3}$$

A solution for ψ can be found from this equation by considering the channel geometry and the boundary conditions, i.e. the ζ-potentials at the slipping planes of the channel walls. For the fluid velocity, a no-slip boundary condition is considered at these walls.

5.2.2 EOF between two parallel plates

A solution to equation (5.1) is only possible in particular geometries. As discussed in section 3.3.2, the microfluidic devices used in this work consist of rectangular microchambers. Because of their aspect ratio the devices can be approximated by a parallel-plate geometry, allowing for an analytical expression of the EOF. This approximation makes that the flow can be described as a function of a single spatial coordinate z. The coordinate is defined as the distance from the middle plane in between the two plates as seen in Figure 5-2. Assuming the surface potential at the interface of both plates equals ζ_{surf}, the potential distribution inside the microchannel is found by solving equation (5.3):

$$\psi(z) = \zeta_{surf} \frac{\cosh(\kappa z)}{\cosh\left(\kappa \frac{d}{2}\right)} \,, \tag{5.4}$$

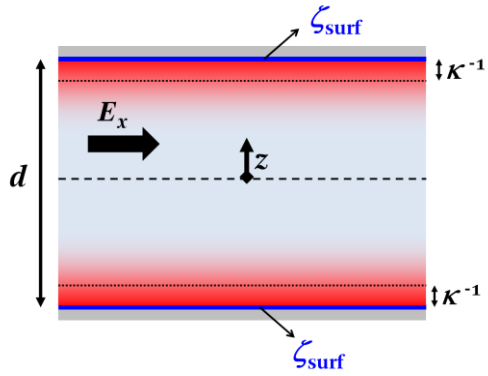

Figure 5-2: Definitions of the coordinates and parameters used in the derivation for EOF between two parallel plates with equal surface potential.

with d the distance between the two plates. When furthermore considering a uniform electric field oriented in the x-direction, the resulting flow is unidirectional along the field. Equation (5.1) then reduces to:

$$\rho_{\mathrm{m}} \frac{\partial}{\partial t} v_x(z,t) = -\frac{\partial}{\partial x} p + \eta \frac{\partial^2}{\partial z^2} v_x(z,t) - \varepsilon \zeta_{\mathrm{surf}} \kappa^2 \frac{\cosh(\kappa z)}{\cosh\left(\kappa \frac{d}{2}\right)} E_x(t) \,. \quad (5.5)$$

The presence of the pressure gradient in this equation relates to how the boundary conditions for the total flow rate at the channel ends are chosen. Typically two situations can occur. In one case the channel ends are open and the flow induced by the electric field can enter and leave the channel. In this case the pressure gradient along x in the channel is zero. Alternatively, one or both channel ends are closed and the total flow rate across the channel ends is zero. The EOF therefore needs to be compensated by a back flow to achieve this boundary condition. In this case there is a pressure gradient in the direction of the flow and it causes a Poiseuille flow in the opposite

direction of the EOF to ensure a zero net flow rate. Note that the field-induced pressure gradient along the spatial directions perpendicular to the electric field is zero. Since the microfluidic devices in this work have open-ended channels, it will be assumed that the pressure gradient equals zero in the following discussion.

a. DC-induced EOF

The case of electroosmotic flow induced by a DC field is solved by setting the time derivative in the left-hand side of equation (5.5) to zero. In the case of open channel ends one retrieves

$$v_x(z) = \left(\frac{\cosh(\kappa z)}{\cosh\left(\kappa \frac{d}{2}\right)} - 1 \right) \frac{\varepsilon \zeta_{\text{surf}}}{\eta} E_x \,. \tag{5.6}$$

In practical applications involving microfluidics, the Debye length κ^{-1} is several orders of magnitude smaller than the separation between the two plates. The velocity of the fluid far enough from the electrical double layer can then be approximated as

$$v_x = -\frac{\varepsilon \zeta_{\text{surf}}}{\eta} E_x \,, \tag{5.7}$$

i.e. one obtains a constant flow profile across the channel. This agrees with the aforementioned plug-like EOF which makes electroosmosis an attractive pumping mechanism for microfluidic devices.

b. AC-induced EOF

When driven by a harmonic electric field at frequency f_E, the steady-state flow profile in the frequency domain can be obtained by Fourier transforming differential equation (5.5). As a result of the linearity of this differential equation, the EOF is also harmonic at the electric field frequency. By defining a complex viscous penetration depth

$$\lambda_\eta = \sqrt{\frac{\mathrm{i}\eta}{2\pi f_\mathrm{E}\rho_\mathrm{m}}}\,, \tag{5.8}$$

the Fourier transformed equation (5.5) is written as

$$\frac{\partial^2}{\partial z^2}\hat{v}_x(z) + \frac{1}{\lambda_\eta^2}\hat{v}_x(z) = \frac{\varepsilon\zeta_\mathrm{surf}\kappa^2}{\eta}\frac{\cosh(\kappa z)}{\cosh\left(\kappa\frac{d}{2}\right)}\hat{E}_x\,, \tag{5.9}$$

of which the solution is found to be

$$\hat{v}_x(z) = \left(\frac{\cosh(\kappa z)}{\cosh\left(\kappa\frac{d}{2}\right)} - \frac{\cos\left(\frac{z}{\lambda_\eta}\right)}{\cos\left(\frac{d}{2\lambda_\eta}\right)}\right)\frac{\lambda_\eta^2\kappa^2}{1+\lambda_\eta^2\kappa^2}\frac{\varepsilon\zeta_\mathrm{surf}}{\eta}\hat{E}_x\,. \tag{5.10}$$

When considering small double layers compared to both the viscous penetration depth and the distance between the plates, as is typically the case, one can approximate the above equation by

$$\hat{v}_x(z) = -\frac{\cos\left(\frac{z}{\lambda_\eta}\right)}{\cos\left(\frac{d}{2\lambda_\eta}\right)}\frac{\varepsilon\zeta_\mathrm{surf}}{\eta}\hat{E}_x\,. \tag{5.11}$$

This equation reveals that AC-induced EOF manifests itself as an amplitude and phase modulation of DC-EOF as a function of both the frequency and position inside the channel. Figure 5-3 provides plots of this modulation at three different electric field frequencies. The solid lines in graph (a) show the modulation of the flow amplitude for a separation of 50 μm between the two plates. Plotted as dashed lines is the modulation at the same frequency of EOF at a single surface, i.e. for the right plate positioned at infinity. From these plots the physical interpretation of the viscous penetration depth becomes clear. It is seen that for distances close to the surface, compared to the viscous

penetration depth, but far enough from the electrical double layer, i.e. $\kappa^{-1} << d/2 - z << |\lambda_\eta|$, the AC-induced EOF approaches the value as calculated for a DC field. For distances from the surfaces in the order of $|\lambda_\eta|$, inertia of the fluid starts playing a role, resulting in damping of the flow amplitude as the distance to the interface increases. For distances much larger than $|\lambda_\eta|$ the EOF amplitude eventually becomes negligible. From the graph it is also clear that $|\lambda_\eta|$, indicated by the dotted vertical lines, corresponds with the distance at which the flow amplitude resulting from the interaction with a single surface is damped by a factor 1/2. Furthermore, as can be seen from Figure 5-3(b), also the phase of the flow with respect to the applied field is position and frequency dependent and determined by the viscous penetration depth.

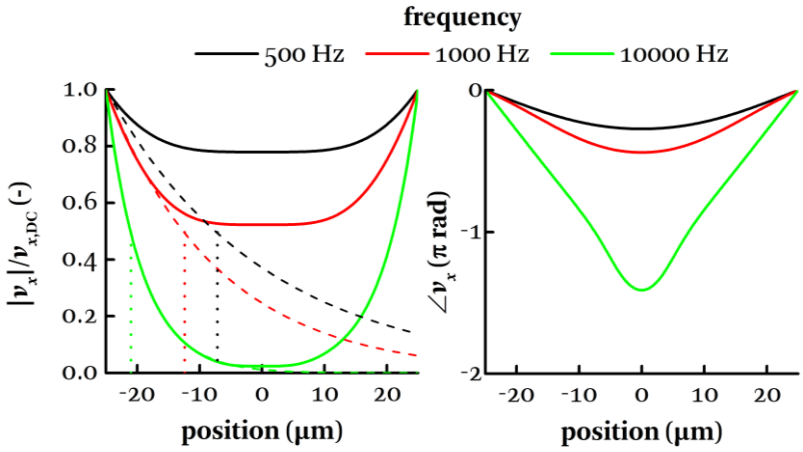

Figure 5-3: Modulation of the EOF amplitude (a) and phase (b) compared to the DC-induced EOF as a function of the position between two parallel plates separated by 50 μm (solid lines). The dashed lines in (a) represent the EOF contribution from the left surface, i.e. if the right plate is positioned at infinity. This visualizes the physical meaning of the viscous penetration depth, indicated by the dotted vertical lines: at this location the EOF-amplitude is damped by a factor 1/2.

5.3 Electroosmosis in OTE experiments

In the previous section it was established that the application of an AC electric field in a microfluidic channel results in EOF. The amplitude and phase of this flow with respect to the field depend on the applied frequency and the location inside the device. When performing an OTE-experiment, one is typically interested in retrieving the electrophoretic mobility of the particle by characterizing the oscillation due to electrophoresis at the field frequency. As a result of the EOF, however, the particle held by optical tweezers experiences an additional drag force. Since the field-induced flow is harmonic at the frequency of the electric field, the resulting drag force is harmonic as well. The oscillation of the particle at this frequency contains thus contributions from both electrophoresis and electroosmosis. By comparing equations (2.30) and (5.11), one establishes that, when the surface potential of both the substrate and particle are comparable, both effects are of the same order of magnitude. This makes that the EOF-contribution results in a false estimate of the electrophoretic mobility in a typical OTE experiment which cannot be corrected with a single measurement of the particle.

There are a number of ways to discard the electroosmotic contribution from an OTE measurement. Since fluid inertia causes damping of the EOF amplitude at high applied frequencies and at distances far from a microfluidic wall, one could obviously choose to measure the particle at conditions at which the EOF becomes negligible. However, often it is not possible to perform OTE-experiments far away from the bottom substrate: either the separation between top and bottom substrate of the microfluidic channel is too small such that EOF can never be avoided or optical tweezing at large distances is impossible due to spherical aberrations of the laser beam, as described in section 3.3.1c. Furthermore, the frequency of the applied electric field cannot be chosen arbitrarily high. Firstly because of practical limitations in the used measurement setup: laser noise and restrictions on the electronics allow only for reliable

measurements up to field frequencies of 5000 Hz in the setup used in this work. A second reason is more fundamental and has been pointed out in section 2.3: the characteristic time for a double layer to form is of the order of $1/(\kappa^2 D_i)$, with D_i the diffusion coefficient of the ionic species making up the double layer. For the double layer around the oscillating particle to be in equilibrium, the time scale at which the electric field perturbation happens should be several orders of magnitude higher than this characteristic time, hence limiting the maximal frequency that can be applied in the experiments to the order of MHz.

Instead, OTE-experiments typically use a different method to retrieve the electrophoretic mobility from the measured oscillation of a particle in an AC electric field. Semenov and coworkers have used a dedicated microfluidic device in which the electric field is only applied across half of the microfluidic channel [145]. They retrieve the oscillation due to electroosmosis by observing the oscillation of a particle in the section of the channel where no electric field is present. This information is used to retrieve the electrophoretic mobility of a particle when the latter is measured in the section of the channel with electric field. Van Heiningen *et al.* have presented a calibration method based on the oscillation measurement of a single optically trapped particle at different applied frequencies and channel heights [146]. The results of these measurements are then fitted to a model resulting from a similar derivation as presented in section 5.2.2b. that quantifies EOF in a microfluidic channel. This calibration method is also used in this dissertation to distinguish between the electroosmotic and electrophoretic contribution to the particle oscillation and will be discussed in more detail in the following paragraphs.

5.3.1 Calibration procedure

In Chapter 3 two analysis methods were presented to characterize the oscillation of an optically trapped particle at a frequency f_E. Power spectrum analysis, equation (3.17), retrieves the amplitude of the

particle oscillation. This method is independent of the phase of the oscillation with respect to the electric field. The phase information is on the other hand employed in equation (3.18), where the oscillation amplitude of the component in phase with the electrophoretic movement is calculated. To establish the contribution of electroosmosis to the results of these analysis methods, the movement of the particle is again described by using the Langevin equation. Because of the additional drag force resulting from the presence of electroosmotic flow with flow velocity v_{EO}, the Langevin equation (3.14), describing the movement of an optically trapped particle, is modified to

$$\gamma\left(\frac{\mathrm{d}x}{\mathrm{d}t}(t)-v_{\mathrm{EO}}(t)\right)+k_{\mathrm{trap}}x(t)=\sqrt{2k_{\mathrm{B}}T\gamma}\xi(t)+\gamma\mu_{\mathrm{EP}}E(t)\,. \qquad (5.12)$$

Both the applied electric field and the EOF are harmonic and a phase difference can exist between the two. Following a similar reasoning as in Chapter 3, the spectral information of the positional signal is used to quantify the particle movement. Equation (5.11) gives the Fourier transform of the EOF fluid velocity. It is seen that $\hat{v}_{\mathrm{EO}}$ is proportional to the applied field, which allows to define a complex mobility as a result of electroosmosis:

$$\mu_{\mathrm{EO}}=-\frac{\cos\left(\dfrac{z}{\lambda_\eta}\right)}{\cos\left(\dfrac{d}{2\lambda_\eta}\right)}\frac{\varepsilon\zeta_{\mathrm{surf}}}{\eta}\,. \qquad (5.13)$$

The Fourier transform of the experimental signal can then be written as

$$\hat{x}^{(\mathrm{ex})}(k)=\frac{\sqrt{2D}\hat{\xi}(k)}{2\pi\left(f_{\mathrm{c}}+\mathrm{i}f_k\right)}+\frac{\left(\mu_{\mathrm{EP}}+\mu_{\mathrm{EO}}\right)E_0t_{\mathrm{msr}}}{4\pi\left(f_{\mathrm{c}}+\mathrm{i}f_k\right)}\left(\delta_{k,E}+\delta_{-k,E}\right)\,. \qquad (5.14)$$

Applying equation (3.19) to this Fourier transformed positional data yields an estimate of the real part of the total mobility:

$$\mu_{\mathrm{EP}} + \mathrm{Re}\left[\mu_{\mathrm{EO}}\right] = \frac{4\pi}{E_0 t_{\mathrm{msr}}} \left\langle f_{\mathrm{c}} \,\mathrm{Re}\left[\hat{x}^{(\mathrm{ex})}\left(f_{\mathrm{E}}\right)\right] - f_{\mathrm{E}} \,\mathrm{Im}\left[\hat{x}^{(\mathrm{ex})}\left(f_{\mathrm{E}}\right)\right]\right\rangle . \quad (5.15)$$

Power spectrum analysis allows to retrieve the absolute value of this total mobility, similarly as in equation (3.16):

$$\left|\mu_{\mathrm{EP}} + \mu_{\mathrm{EO}}\right|^2 = \frac{16\pi^2\left(f_E^2 + f_{\mathrm{c}}^2\right)}{E_0^2 t_{\mathrm{msr}}} \left\langle P_x^{(\mathrm{ex})}\left(f_E\right) - P_{x,\mathrm{Br}}\left(f_E\right)\right\rangle . \quad (5.16)$$

The left-hand side of the two above equations can be written as a function of the applied frequency and the position in the channel, provided that all other parameters of equation (5.13) are known, from which the electrophoretic mobility can then be retrieved. In practice, however, the ζ-potential of the walls of the microfluidic device is not a given, since it varies depending on the properties of liquid, e.g. its ionic strength, inside the device. One can circumvent this issue by performing multiple measurements in which one or more parameters of equation (5.13) are varied in a known fashion while other parameters remain constant. Two parameters that are varied straightforwardly are the applied frequency and the position of the particle inside the channel. By performing these multiple measurements on a single particle, one ensures μ_{EP} does not change.

Optimal values for both the surface ζ-potential of the bottom substrate and μ_{EP} are obtained by performing a best fit for the right-hand side of equations (5.15) and (5.16), obtained from the measurements, to the analytical expression given by the left-hand side of the respective equations. In practice a third fitting parameter is introduced: an initial separation between the particle and the bottom substrate z_0 to which all other separations are referred. The reason for this third parameter is purely practical: due to slight variations in the bottom substrate thickness and because of the spherical

aberration present in the laser beam, it is often not easy to know the exact separation between the particle and bottom substrate. However, an axial translation of the microscope objective and the translation of the particle are very precise. This makes that the addition of the reference z_0 as a single fitting parameter for all the measurements done during one calibration is sufficient.

5.3.2 Example

The above described calibration procedure is performed in an IBIDI-microchamber containing a 12.4 mg/l aqueous NaCl solution. A polystyrene microsphere of 1 μm diameter is optically trapped near the middle in between the inlet and outlet and subjected to an AC electric field with amplitude 3.14 kV/m. Its oscillation is measured at frequencies ranging from 200 Hz to 7500 Hz and at different z-positions. Figure 5-4 plots the measured absolute value of the total mobility (a) and the real part of the total mobility (b). Also presented is a fit of these data points to equations (5.16) and (5.15), respectively. The best-fit parameters are determined as provided in Table 5-1 and Table 5-2, where it is seen that the estimates for the fitting parameters μ_{EP} and ζ_{surf} agree within 1 % for the two fits. The R-squared values for both fits are calculated as 0.9987 and 0.9983 for (a) and (b), respectively. This indicates the proposed model describes the physical reality well. Note however that the value of the calculated surface potential exceeds the thermal voltage significantly and thus the condition for the Debye-Hückel approximation to describe the electrostatic potential inside the double layer and to derive the expression for EOF in the channel is not satisfied. This makes that the numerical value estimated by the fits may not reflect the actual surface zeta potential. This has no repercussions on the calibration procedure, however. The actual potential distribution inside the double layer only affects the electroosmotic flow near the surface, at distances in the order of the Debye length, i.e. several nanometers. When considering distances much larger than the Debye length, the electroosmotic flow in the double layer can be seen as a flow at the

surface, i.e. a slip boundary condition with a flow speed $\varepsilon\tilde{\zeta}E/\eta$ with $\tilde{\zeta}$ the estimated ζ-potential from the fit. This makes that the description of the mobility by equations (5.15) and (5.16) is still correct, even without the condition for the Debye-Hückel approximation being fulfilled. Extending the model such that physically meaningful surface potentials are estimated in situations in which surface ζ-potentials can exceed the thermal voltage would be possible by incorporating the Gouy-Chapman solution to the Poisson-Boltzmann equation instead of the Debye-Hückel approximation. This, however, results in a differential equation which has no closed form solution.

These measurements now allow for a mapping of the electroosmotic flow inside the microchannel. From the fitting procedure to the observed mobility, a value for the surface potential of the bottom substrate is retrieved. The EOF is described by equation (5.11), which only uses the surface potential as input parameter.

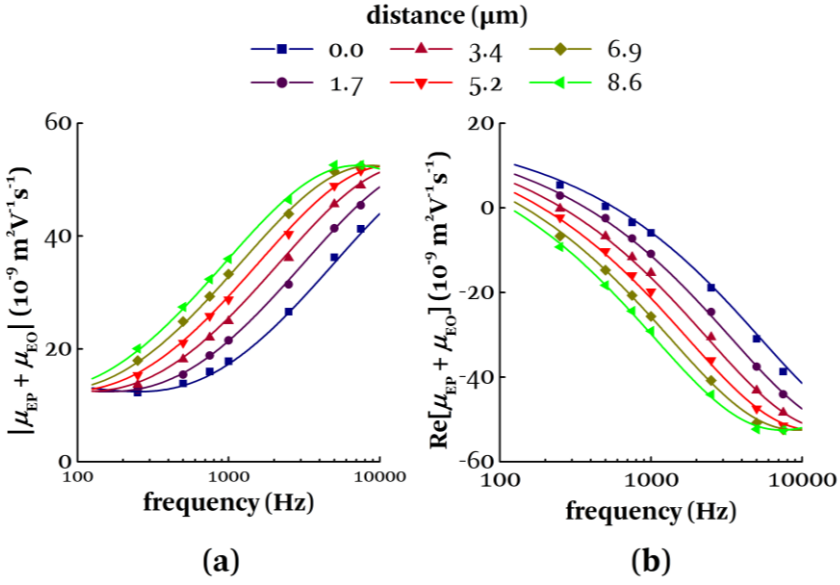

Figure 5-4: Calibration for EOF in a microchamber affecting the mobility measurements. The mobility of the particle is measured at different frequencies and different positions with respect to a reference position z_0 from the substrate. These measurements are fitted to (a) equations (5.16) and (b) equation (5.15), from which the particle's electrophoretic mobility, the surface ζ-potential of the substrate and z_0 are retrieved.

Table 5-1: Best fit values from which the solid lines in Figure 5-4(a) are constructed, together with the 95% confidence interval.

Parameter (unit)	value	95%-CI
μ_{EP} (10^{-9} $m^2V^{-1}s^{-1}$)	-48.8	[-48.0, -49.4]
ζ_{surf} (mV)	-98.0	[-100.8, -95.2]
z_o (µm)	6.65	[6.44, 6.89]

Table 5-2: Best fit values from which the solid lines in Figure 5-4(b) are constructed, together with the 95% confidence interval.

Parameter (unit)	value	95%-CI
μ_{EP} (10^{-9} $m^2V^{-1}s^{-1}$)	-50.0	[-50.8, -49.3]
ζ_{surf} (mV)	-98.8	[-100.2, -97.4]
z_o (µm)	6.74	[6.50, 6.99]

5.4 Microfluidic wall ζ-potential measurements

The calibration method for EOF in a microchannel described in the previous section retrieves the ζ-potential of the microfluidic wall by fitting a theoretical model to mobility measurements taken at different applied frequencies and different axial positions in the microchamber. This allows separating the contributions to the motion resulting from electroosmosis and from electrophoresis of the particle. This section will show that these calibration measurements also offer a reliable way to characterize the electrical properties of the microfluidic wall.

The electrical properties of a microfluidic wall are determined much like the electrical properties of colloidal particles. The charging of these walls results from dissociation of surface groups, adsorption of ionic species or other mechanisms. This surface charge results in the formation of an electrical double layer, with similar properties as described in section 2.3. Again, the electrostatic potential at the slipping plane is defined as the ζ-potential ζ_{surf}. This potential determines the electrokinetic behavior of the fluid around it (electroosmosis) and the interaction with colloidal particles inside the chamber. Knowledge of this potential is crucial when applications involving EOF are used or specific chemical treatments of the channel walls is required [147], [148]. The proposed method gives the advantage of doing this characterization *in situ*.

To demonstrate the working principle of measuring the ζ-potential of microfluidic walls, an experiment is set up in which the electrical properties of the walls are changed by varying the ionic strength of an aqueous NaCl solution inside the device. It can be intuitively understood how a changing ionic strength affects these properties. The surface charge of a wall is not expected to change significantly by a varying ionic strength up to NaCl concentrations of 100 mmol/m^3 [149]. The change in ζ-potential results instead from a varying double

layer thickness: as given by equation (2.25), increasing the concentration of ions in a solution accounts for thinner double layers. The slipping plane is typically located away from the solid-liquid interface inside the electrical double layer. Its position is not expected to change by altering the ionic strength of the liquid surrounding the microfluidic wall. This makes that, if the double layer thickness decreases, the absolute value of the potential at this slipping plane is expected to decrease as well. Varying the ionic strength of the liquid thus allows changing the ζ-potential of the walls of the microfluidic device.

In the experiment eight solutions containing NaCl concentrations c_{NaCl} ranging from 49.8 mg/l to 0.377 mg/l are considered. A solution is brought into an IBIDI device and a polystyrene particle with radius r = 0.5 μm, suspended in this solution, is optically trapped. The concentration of particles is very low (a weight percentage below 10^{-5} wt%) to avoid a second particle entering the optical tweezers during the course of an experiment. The mobility of this particle is measured at different applied frequencies and different distances from the bottom substrate. Fits to these measurements, similar as the ones presented in Figure 5-4, provide an estimate for both the particle's electrophoretic mobility and ζ_{surf} of the bottom substrate. Figure 5-5 plots the obtained estimates for these fitting parameters as a function of the concentration of NaCl.

It is observed firstly that both the particle electrophoretic mobility and the bottom substrate ζ-potential are negative. This results from a negative charge present on the surface of the particle and the substrate, respectively. For the polystyrene particle this negative surface charge can be explained. Styrene by itself does not have a functional group that is expected to dissociate at neutral pH and would explain this negative charge. Instead, the origin of the negative charge on the polystyrene particle results from the fabrication process of these particles: initiator fragments, e.g. SO_4^{2-} , are frequently

present at the polymer chain ends resulting in negatively charged sulfonate groups [150]. The nature of the negative charge on the IBIDI substrate cannot be acknowledged for since the material is not specified by the manufacturer.

Furthermore, both graphs show that a varying ionic strength of the aqueous solution affects both parameters. It is seen that the absolute value of the ζ-potential of the bottom substrate decreases monotonically with increasing ionic strength of the solution. This agrees with the reasoning presented above in which ζ_{surf} is reduced due to a thinner double layer. The electrophoretic mobility of the particle does not show a monotonic trend. Its absolute value first shows an increase for increasing NaCl concentration up to a maximum at a concentration of 3 mg/l, after which it also decreases. Semenov *et al.* have observed a qualitatively similar behavior of the electrophoretic mobility of polystyrene particles as a function of the ionic strength [151]. This trend can be explained by considering equation (2.30) which shows how the electrophoretic mobility of a particle is affected by a varying double layer thickness κ^{-1}. Aside from the changing zeta potential, the electrophoretic mobility depends directly on κ in the form of a proportionality factor given by Henry's equation (the retardation force). Also relaxation effects can play a role when the ζ-potential exceeds 25 mV. In this case the Ohshima-Healy-White equation, as presented in section 2.5.1, can be used. It should be noted that this approximation assumes an electric field that varies slowly compared to the characteristic time scale at which the double layer polarization occurs. This condition is not fulfilled in the presented experiments: the period of the electric field is in the order of this time scale. When applying the Ohshima-Healy-White equation to retrieve the ζ-potential of the particle from the data in Figure 5-5(a), some of the experimental results prove to be inconsistent: at low salt concentrations the observed electrophoretic mobility yields no solution for ζ-potential. This discrepancy between standard electrokinetic theory and experiment by OTE at low salt

concentrations has been encountered multiple times in literature [23], [151]. I therefore opt for an analysis solely based on Henry's equation for the mobility, in which polarization of the double layer is ignored to convert the measured particle mobility to a value for its ζ-potential. The obtained ζ-potentials are plotted as a function of the ionic strength of the solution in Figure 5-5(b) and are seen to follow a qualitatively similar trend as observed for ζ_{surf} . The occurrence of particle ζ-potentials exceeding 50 mV does however imply the analysis with Henry's equation is not valid. The potentials retrieved from this analysis do therefore not necessarily correspond with the physical values of these parameters.

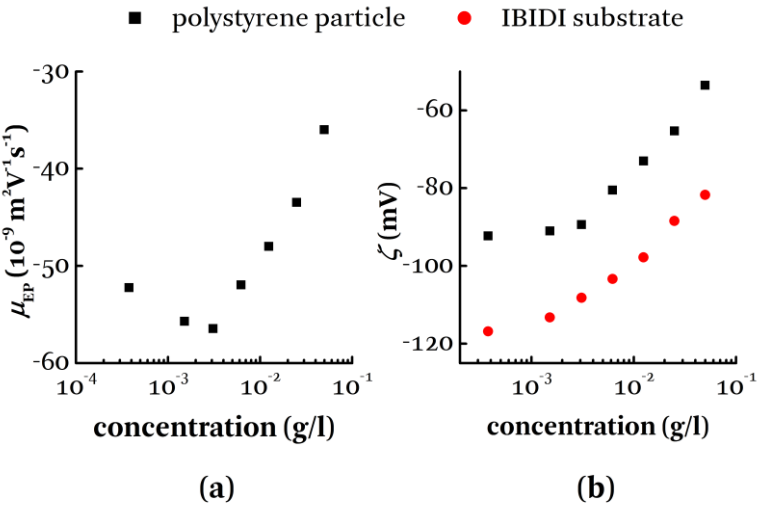

Figure 5-5: The electrophoretic mobility of a 1 µm polystyrene particle, plotted in figure (a) as a function of the NaCl concentration of the continuous medium, is transformed to a ζ-potential by means of equation (2.30). This potential, together with the ζ-potential of the bottom substrate is plotted in (b) as a function of the concentration NaCl in the solution. The values are obtained by the calibration procedure for EOF in the device, as described in section 5.3.

5.5 Conclusions

Electroosmosis and its effect on OTE-measurements were discussed. By approximating the microfluidic devices used in the experiments as two parallel plates, it was shown that an analytical description of both DC- and AC-induced EOF can be obtained. Especially the AC-induced EOF has an influence on an OTE-measurement: it accounts for an additional drag force. This additional drag is harmonic at the applied electric field frequency. It influences the oscillation of a particle in this field and thus interferes with the mobility measurement. To resolve this interference, a calibration method was proposed. The calibration makes use of the fluid inertia on the EOF: its amplitude and phase relation with respect to the applied electric field is seriously affected by the applied frequency and position inside the channel. By measuring the influence of these two parameters on the particle oscillation in the electric field, a map of the electroosmotic flow is obtained and the electrophoretic mobility is retrieved by subtracting the EOF contribution from a mobility measurement.

From this mapping, the ζ-potential of the microfluidic substrates can be calculated. The calibration procedure thus offers a way to probe the surface properties of the microfluidic channel. This was demonstrated in an experiment in which the electrical properties of the substrate were determined by measuring a mobility of a particle at different salt concentration of the continuous medium. A higher salt concentration accounts for thinner double layers, reducing the ζ-potential of both the particle and the substrate. This change was indeed observed. The measured values proved, however, to be inconsistent with electrokinetic theory in which double layer polarization is taken into account. An analysis based on Henry's formula did give a comparable trend between the ζ-potential of both the particle and the substrate, although these values cannot be straightforwardly interpreted as physical meaningful values.

Chapter 6
Biosensing applications

6.1 Introduction

In this chapter optical trapping electrophoresis is used to investigate the relationship between the electrophoretic mobility of a single colloidal particle and the concentration of a target protein in the buffer. More specifically, this chapter examines how the mobility of a bare polystyrene particle and a biotin-coated polystyrene particle is influenced by the presence of the avidin, which is known to bind specifically to biotin. Avidin is a relatively large glycoprotein: it has a molecular weight of about 67 000 g/mol and a hydrodynamic radius of 3-4 nm [152], [153]. With an isoelectric point of 10.5, avidin is positively charged at physiological pH. Biotin is considerably smaller (m_{mol} = 244 g/mol) and has a negative charge at neutral pH (pKa=4.5) [154]. The avidin-biotin binding is considered as a receptor/ligand model system because of its strong affinity: it has a dissociation constant of approximately 10^{-15} M. For this reason it is often used to indicate the feasibility of a biodetection technique [155], [156].

This chapter aims at understanding the adsorption mechanisms taking place when a biotinylated particle is immersed in a buffer containing avidin. Two types of experiments are devised for this, each discussed in a separate section. The next section describes steady-state measurements of the mobility of biotinylated and non-functionalized polystyrene particles as a function of the avidin concentration. The second type of experiments monitors the time-dependent mobility change of a biotinylated particle when a sudden change in avidin concentration occurs. Part of this work has been published as an original research article [157].

6.2 Affinity measurement of avidin with OTE

OTE is used to measure the mobility of biotinylated and non-functionalized (bare) particles in a buffer solution as a function of the avidin concentration inside this solution. Based on these measurements, a model for the avidin adsorption on these particles is established.

6.2.1 Sample preparation

The non-functionalized polystyrene particles of diameter 1 μm come as a 1 wt% suspension in water. Similarly sized polystyrene microspheres with biotin coating are purchased from Life Technologies as a 1 wt% suspension in a sodium phosphate solution containing 50 mmol/l NaCl, 0.02 % Tween20 and 5 mM azide. Stock solutions of both particle types are prepared by diluting the aforementioned suspensions with a 1X Dulbecco's phosphate buffered saline (DPBS) with 0.1 % Tween20, down to a particle concentration of 9.6 μg/ml. Lyophylized avidin is reconstituted with the aforementioned DPBS+Tween20 solution after which stock solutions containing 6.1 mmol/m^3, 0.61 mmol/m^3, and 61 μmol/m^3 avidin in the DPBS+Tween20 solution are prepared. An experimental sample is prepared by mixing a certain amount of one of the avidin stock solutions with the DPBS-Tween20 solution until a volume of 1.0 ml is attained. To this vial 1.0 ml of either the uncoated or biotinylated particle stock solution is added and mixed, resulting in a particle concentration of 4.8 μg/ml. The sample is then stored at 4 °C for at least two days after which these solutions are further diluted one in five prior to the experiment. A sample volume of 130 μl is inserted into an IBIDI microchamber after which a single colloidal particle is optically trapped and its electrophoretic mobility measured as described in Chapter 3. Per concentration the electrophoretic mobility of at least seven particles is measured.

6.2.2 Calibration for electroosmosis

As discussed in the previous chapter, applying an electric field inside a microfluidic device results in electroosmotic flow. A calibration procedure was introduced to assess and eliminate the effect of this flow on the measurement of the electrophoretic mobility of a colloidal particle. This calibration retrieves a value for the ζ-potential of the bottom substrate of the microchamber, from which the EOF in the channel can be mapped. The procedure is performed with a biotinylated particle in four mixtures with an avidin concentration of 0 mol/m^3, 61 µmol/m^3, 0.61 mmol/m^3 and 6.1 mmol/m^3. The respective ζ-potentials are plotted in Figure 6-1. It is seen that an increasing concentration of avidin inside the solution increases the ζ-potential of the microfluidic surface. This can be explained as a result of avidin adsorption onto the microfluidic wall. The influence of avidin adsorption on the ζ-potential is twofold. Firstly, avidin is a positively charged molecule at physiological pH and therefore increases the surface potential of the interface it adsorbs on. Secondly, the size of the avidin molecules is in the order of several nanometers. When they adsorb onto an initially smooth surface, avidin molecules increase the drag force experienced by the liquid near that surface. This effectively shifts the slipping plane outwards and lowers the absolute value of the ζ-potential.

From these calibration measurements it is established that the difference between the measured mobility and the electrophoretic mobility is between -0.91×10^{-9} m^{2}V^{-1} s^{-1} and -2.3×10^{-9} m^{2}V^{-1} s^{-1}, for high and zero avidin concentration in the buffer solution, respectively. The expected ζ-potential for any other avidin concentration is calculated by a piecewise monotone cubic interpolation of the data points given in Figure 6-1. This allows to calculate μ_{EO} from equation (5.13), by which the EOF-contribution can be eliminated.

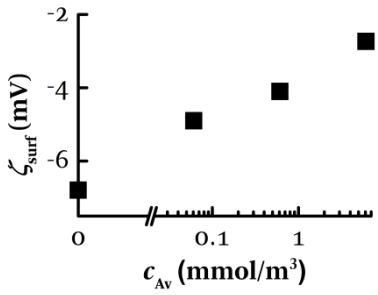

Figure 6-1: ζ-potential of the bottom substrate of an IBIDI microchannel as a function of the concentration of avidin inside the solution. For higher bulk concentrations, avidin adsorbs more onto the microfluidic walls, which increases the surface potential.

6.2.3 Adsorption experiments with OTE

a. Avidin concentrations under 2.5 µmol/m^3 (165 ng/ml)

Figure 6-2 plots the electrophoretic mobility of both biotinylated and uncoated polystyrene particles as a function of the avidin concentration in the buffer solutions for concentrations up to 2.3 µmol/m^3. Each point in the plot gives the average mobility over seven different particles and the error bars indicate the standard deviation over these measurements. It is firstly observed that at zero avidin concentration the electrophoretic mobility of the biotinylated particles (-2×10^{-8} m^2 V^{-1} s^{-1}) is lower than the mobility of the bare particles (-1×10^{-8} m^2 V^{-1} s^{-1}). The origin of the negative charge on the bare polystyrene particles has been discussed in section 0. The additional negative charge on the biotinylated particles results from the functionalization. As mentioned before, biotin is negatively charged at physiological pH. Furthermore, the biotinylation of the particles involves a carboxylation step of the polystyrene which, when these carboxylic groups are not bound to a biotin molecule, introduces additional negatively charged groups onto the particle surface at neutral pH, as discussed in section 2.3.

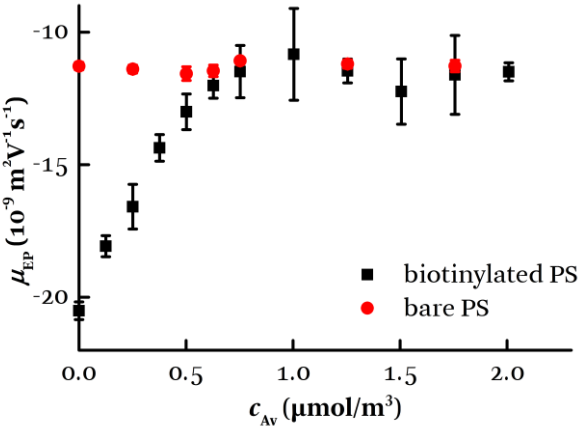

Figure 6-2: The mobility dependence of single biotinylated and non-functionalized polystyrene particles on the avidin concentrations. The error bars indicate the standard deviation of the measurements of at least seven particles. At these avidin concentrations, only the mobility of the biotinylated particles is affected by the presence of avidin. The increase can be explained by specific adsorption of the latter onto the particle surface.

From Figure 6-2 is can also be seen that the electrophoretic mobility of bare polystyrene appears unaffected by the presence of a small amount of avidin in the buffer. On the other hand, the mobility of the biotinylated polystyrene microparticles is clearly affected by adding a small amount of avidin to the solution. More specifically it is observed that the electrophoretic mobility increases with increasing avidin concentration. Furthermore, the figure suggests a linear increase at concentrations less than 0.6 µmol/m^3 after which the mobility of the biotinylated particles tend towards a plateau value near -1.2×10^{-8} $m^2V^{-1}s^{-1}$. The increase in mobility can again be explained by adsorption of avidin onto the functionalized particles: the ζ-potential increases firstly because the net surface charge of the (initially negatively charged) microparticles increases when positively charged avidin molecules adsorb to it. Also, the adsorption of these

nanometer-sized molecules shifts the slipping plane outward as a result of the hydrodynamic screening of the double layer by the soft layer, as was described in section 2.5.2. It can be noted that the plateau value of the biotinylated particles seems to coincide with the mobility of the bare polystyrene particles. This is probably by accident. Both the fact that the surface modification of both types of polystyrene particles is different and that the increase in mobility of the biotinylated particles is explained with soft particle electrokinetics makes that there is no physical ground for the two values to be equal and it is expected that both values would be significantly different at a different salinity of the solution.

Since the increase in mobility at low avidin concentration is only observed for the biotinylated particles, the surface adsorption is due to specific binding of the avidin molecules with the biotin coating. Because of the non-dissociative nature of the avidin-biotin bond, all molecules present in the solution are expected to bind to the available biotin sites until all binding sites are consumed. This explains the linear increase of the mobility as a function of the avidin concentration up to 0.6 μmol/m^3, which is the concentration at which all available biotin sites are occupied. At higher concentrations, further adsorption due to specific binding is inhibited and the electrophoretic mobility of the particle remains at a constant value, i.e. the observed plateau value.

b. Avidin concentration above 2.5 μmol/m^3 (165 ng/ml)

The mobility of bare and biotinylated particles show a similar dependence on the avidin concentration when the latter exceeds 2.5 μmol/m^3. This is represented in Figure 6-3. Both particle types show an increase in electrophoretic mobility and approach an asymptotic value of approximately 0 $m^2 V^{-1} s^{-1}$ for high avidin concentrations, i.e. above 500 μmol/m^3.

Again, the increase in mobility can be explained by the adsorption of avidin molecules onto the particles. Now the mechanism behind the

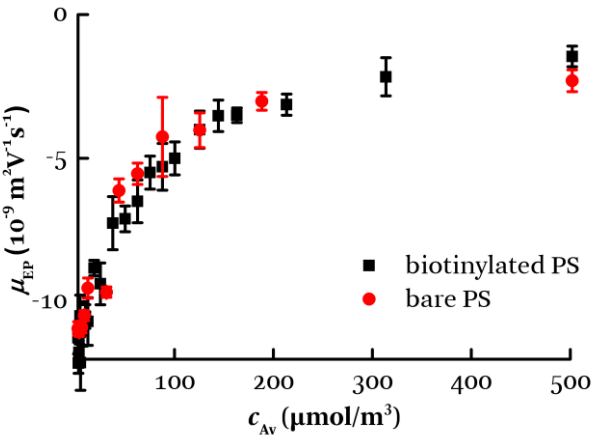

Figure 6-3: At higher avidin concentrations both the mobility of the bare and biotinylated polystyrene particles are affected. The observed change in mobility results from non-specific adsorption of avidin onto the particles.

adsorption is non-specific interaction of the avidin with the particle surface. The observed asymptotic value of the electrophoretic mobility can be linked to the mobility value at which all available nonspecific binding sites are occupied.

6.2.4 Adsorption model

The experimental results discussed above can be quantified in an adsorption model that provides an expression for the electrophoretic mobility of a particle in terms of the concentration of avidin c_{Av} (unit: mol/m^3) inside the solution. For this the assumption is made that the change in mobility is linearly proportional to the amount of avidin adsorbed on the particle. This is not obvious from a theoretical point of view and is, in this dissertation, an assumption that is fulfilled *a posteriori*. A proper treatment involving soft particle electrokinetics could justify this claim on a theoretical level. This treatment would involve characterizing the particles at different salinities of the medium to evaluate the different processes involved in the response

of an avidin coated particle to an external electric field. Such studies were however not undertaken in this work.

The model assumes that an amount N_S and N_{NS} (units: mol) can adsorb specifically and nonspecifically, respectively, on a particle. The electrophoretic mobility μ_{EP} of the particle is then expressed in terms of the fractions ϕ_S and ϕ_{NS} of these masses that are present on the particle:

$$\mu_{EP} = \mu_{EP,o} + \delta_\mu \left(\frac{N_S \phi_S + N_{NS} \phi_{NS}}{N_S + N_{NS}} \right). \tag{6.1}$$

In this equation $\mu_{EP,o}$ represents the particle mobility in the buffer with zero avidin concentration and δ_μ gives the increase in mobility when all binding sites, specific and nonspecific, are occupied (i.e. ϕ_S and ϕ_{NS} equal unity).

The specific adsorption is modeled as a high-affinity adsorption in which an avidin-biotin bond is considered irreversible. Consequently all avidin present inside the buffer will bind specifically to the biotin coating until all available specific sites are occupied, rendering a linear relationship between ϕ_S and the avidin concentration c_{Av} in the mixture until saturation:

$$\phi_S = \min\left(\frac{c_{Av}}{n_{part} N_S}, 1 \right), \tag{6.2}$$

where n_{part} represents the number of particles per unit volume.

The nonspecific adsorption is modeled as a Langmuir isotherm. This isotherm expresses the surface coverage of a species on a particle as a dynamic equilibrium between adsorption of avidin molecules inside the solution, termed free avidin molecules, onto available nonspecific binding sites and desorption of avidin to the bulk solution:

$$\mathrm{Av}_{\mathrm{free}} + \mathrm{site} \underset{}{\overset{K}{\rightleftharpoons}} \mathrm{Av}_{\mathrm{bound}}\,. \tag{6.3}$$

The equilibrium constant K (unit: $m^3\ mol^{-1}$) is the ratio of the adsorption rate constant to the desorption rate, or equivalently, the ratio of bound sites $\phi_{\mathrm{NS}} N_{\mathrm{NS}} n_{\mathrm{part}}$ to the product of the free avidin concentration and the concentration $c_{\mathrm{Av,free}}$ of unbound sites $\left(1-\phi_{\mathrm{NS}}\right) N_{\mathrm{NS}} n_{\mathrm{part}}$:

$$K = \frac{\phi_{\mathrm{NS}}}{c_{\mathrm{Av,free}}\left(1-\phi_{\mathrm{NS}}\right)}\,. \tag{6.4}$$

This provides an expression for ϕ_{NS}:

$$\phi_{\mathrm{NS}} = \frac{K c_{\mathrm{Av,free}}}{1 + K c_{\mathrm{Av,free}}}\,. \tag{6.5}$$

From a theoretical point of view, the Langmuir isotherm is only valid to describe species adsorption for particles with a uniform affinity across their surface that does not depend on the surface concentration of the adsorbant. However, equation (6.5) does give an adequate description of many experimental results that do not fulfill these conditions [35]. Moreover, possible electrostatic interactions between the individual molecules and between the molecules and the particle are not incorporated in this model. Also spatial constraints, limiting the number of avidin molecules on the surface, could make that equation (6.3) does not necessarily hold. To validate if the description by a Langmuir isotherm is appropriate, it is customary to plot $1/\phi_{\mathrm{NS}}$ as a function of $1/c_{\mathrm{Av}}$, from which a linear dependence should emerge according to equation (6.5). To make this plot for the mobility measurements of the biotinylated particles presented in Figure 6-3, the plateau value obtained in Figure 6-2 is subtracted from the measured mobility. This gives a mobility μ^* that is proportional to ϕ_{NS}. Figure 6-4 plots the reciprocal of μ^*as a function of $1/\ c_{\mathrm{Av}}$ for avidin concentrations higher than 30 µmol/m^3. Also provided is a linear fit to

this data. The R-squared value of 0.9652 indicates the mobility data is indeed well described by a Langmuir isotherm.

In equation (6.5), the concentration of unbound avidin is used to calculate ϕ_{NS}. It is retrieved by equating the initial concentration of avidin with the sum of the free avidin concentration and the bound avidin:

$$c_{Av,free} = c_{Av} - n_{part}\left(N_S\phi_S + N_{NS}\phi_{NS}\right). \tag{6.6}$$

Combined with equation (6.5), the above equation yields an expression for ϕ_{NS} as a function of c_{Av}:

$$\phi_{NS} = \frac{1}{2Kn_{part}N_{NS}}\left(Kc_{Av} + Kn_{part}\left(N_{NS} - N_S\phi_S\right) + 1 - \sqrt{\left(Kc_{Av} - Kn_{part}\left(N_{NS} + N_S\phi_S\right) + 1\right)^2 + 4Kn_{part}N_{NS}}\right). \tag{6.7}$$

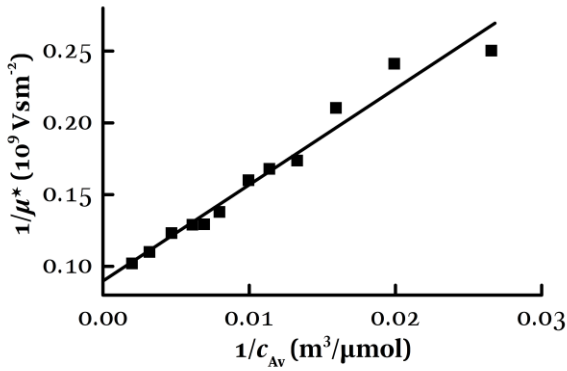

Figure 6-4: By plotting the reciprocal of the change in mobility versus the inverse avidin concentration, one can establish the non-specific binding follows a Langmuir isotherm given by equation (6.5).

Equations (6.2) and (6.7) now allow writing the measured electrophoretic mobility of a particle in terms of the concentration of avidin added to the solution via equation (6.1). Prior to an experiment, the original mixtures were diluted one in five as was described in section 6.2.1. Dilution of a sample makes that $c_{\mathrm{Av,free}}$ is decreased and the adsorption process (6.3) is out of equilibrium. Desorption of non-specifically bound avidin from the particle takes place until a new dynamic equilibrium between $c_{\mathrm{Av,free}}$ and ϕ_{NS} which is again given by equation (6.5). This makes that equation (6.7) holds, even for the diluted samples, as long as c_{Av} and n_{part} represent the concentrations of avidin and particles in the final mixture, respectively.

The above model is fitted to the mobility measurements of the biotinylated particle that were presented in section 6.2.3. Figure 6-5 repeats the experimental results and displays the best fit corresponding to this data. The best-fit values for the parameters are summarized in Table 6-1. The two different adsorption regimes can clearly be identified: the specific binding is predominant up to a concentration of 0.6 μmol/m^3, at which the curve shows a slope discontinuity. From this concentration onwards only non-specific binding is responsible for the mobility increase. The fit values provide the total amount of bound avidin, specific and non-specific combined, per unit particle mass. It should be noted however that avidin adsorption onto the microfluidic walls is not taken into account in this model. This may result in a wrongful estimate of the equilibrium constant K. More specifically, adsorption on the microfluidic wall depletes the bulk from free avidin. This gives a shift of the dynamic equilibrium presented in equation (6.3) to the left. This makes that non-specific adsorption onto the particle takes place only at higher concentrations of avidin compared to the case in which there would be no adsorption onto the microfluidic walls. This makes that, as a result of wall adsorption, the estimated value of the equilibrium constant based on the model may be lower than the actual value.

Table 6-1: best-fit parameters used to describe the mobility variation as a function of the concentration of avidin as presented in Figure 6-5.

parameter (unit)	value	95% CI
$\mu_{EP,0}$ (10^{-9} $m^2 V^{-1} s^{-1}$)	-20.4	[-21.8, -19.0]
δ_μ (10^{-9} $m^2 V^{-1} s^{-1}$)	20.4	[18.1,22.8]
K (10^3 m^3 mol^{-1})	13.7	[7.3, 20.1]
N_S (amol)	0.31	[0.25, 0.37]
N_{NS} (amol)	0.44	[0.30, 0.58]

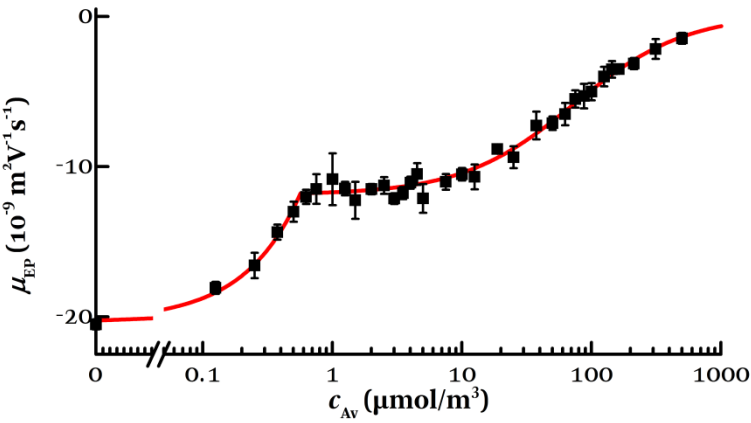

Figure 6-5: Fit of the adsorption model to the mobility measurements of the biotinylated particles that were presented in Figure 6-2 and Figure 6-3. The graphs shows that the model accurately describes the mobility for a concentration range spanning four orders of magnitude. The best-fit parameters are summarized in Table 6-1.

6.3 Time-dependent mobility measurements

The development of a biosensor is often a tradeoff between different parameters. For example, a long measurement time on a sample typically accounts for a more sensitive read-out but reduces the practical operation of the system in clinical circumstances. The experiments discussed in the previous section have allowed retrieving a binding characteristic of avidin to biotinylated polystyrene microparticles, but for this an incubation time of several days was necessary. It is clear that a different parameter than the steady-state mobility of a particle is to be used in an OTE-based biosensor.

In this section, I make use of the fact that OTE allows for time-dependent mobility measurements to retrieve different parameters that can establish the concentration of avidin inside a buffer solution. Foremost I focus on characterizing the dynamic binding of avidin onto a biotinylated particle via specific adsorption, since specificity is required for a biosensor. To further support the adsorption model presented in the previous section, also the time-dependent non-specific binding and unbinding of avidin is measured and modeled.

6.3.1 Experimental procedure

The experiments make use of the flow cell that was described in section3.3.2b. Two distinct liquids, each pumped at a flow rate of approximately 0.1 µl/s, can exist in one microfluidic channel. This enables for an optically trapped particle to be brought from one medium across the boundary between the two liquids to the other medium. The width of this boundary is determined by the diffusion of avidin from the high- to the low-concentration medium and is calculated to be in the order of 10 – 100 µm at the measurement position. The particle is moved across the boundary with a speed of 500 µm/s, which makes that it resides in this boundary far less than 1 s.

Two different experiments are undertaken. Firstly, adsorption experiments consist of bringing a biotinylated particle from an avidin-free buffer to a buffer containing a certain concentration of avidin. Different avidin concentrations, ranging from 0.1 μmol/m^3 (6.6 ng/ml) to 1600 μmol/m^3 (106 μg/ml) are considered. Secondly, a desorption experiment is performed. In this experiment, biotinylated particles are first mixed together with an avidin-rich buffer such that complete saturation occurs, i.e. the particles inside the mixture are initially located on the far-right of Figure 6-5. After incubation, this avidin-rich mixture is inserted into one arm of the Y-junction and an avidin-free buffer is injected into the other. A particle is trapped and brought to the avidin-free buffer, where desorption of the avidin can happen.

In each of these experiments, the mobility of the optically trapped particle is continuously monitored by observing its oscillation inside an AC electric field. This position measurement over several hundreds of seconds is split up in intervals of 1 s which are analyzed independently to retrieve a value of the mobility at each time interval. Again, attention is paid that the separation between the particle and the bottom substrate remains fixed. This makes that the EOF contribution to the observed mobility is constant. No calibration for electroosmosis was performed, but the EOF-contribution is eliminated by measuring the mobility of multiple biotinylated particles in an avidin-free medium and establishing the difference in this mobility with the mobility measured for these particles in section 6.2.3. This difference is then subtracted from the observed mobility to establish the electrophoretic mobility μ_{EP} .

6.3.2 Numerical simulations

To provide a physical understanding of the transport mechanisms leading to the avidin adsorption, numerical modeling of the above described experiment is carried out. Using COMSOL, a finite element simulation is used to jointly describe the fluid flow around the microsphere, the transport of avidin from the bulk solution toward the particle and adsorption reactions at the particle surface. This

happens in a 3D-axisymmetric geometry in which the sphere is defined as a half circle on a line defining the axial symmetry as presented in Figure 6-6.

The fluid flow is calculated using the assumptions of creeping flow. For this, the Reynolds number should be significantly smaller than 1, which is fulfilled in the presented experimental setup. As demonstrated in Figure 6-6, at the particle surface a no-slip boundary condition is introduced. An inlet, from which the fluid enters with a velocity U_o, and outlet are defined 10 µm from the particle center, perpendicular to the symmetry axis. The simulation region is closed by a line, parallel to the symmetry axis of the geometry, at 10 µm from the particle center. At this line a symmetry boundary condition is set. This means the influence of the walls of the microfluidic device on the flow profile are not taken into account and the particle is instead assumed to be in an infinite bath moving at a velocity U_0 with respect to the particle. The flow profile is calculated once and assumed to be time-independent. U_0 is taken to be 250 µm/s.

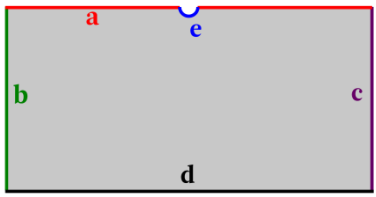

Figure 6-6: Schematic drawing of the used geometry in the numerical modeling of the adsorption experiment. A 3D-axisymmetry is obtained by defining an axis of symmetry at a. In b an outlet is defined for both the fluid as the avidin. Line c represents the inlet at which the avidin concentration is kept at a $c_{Av,0}$. At line d a symmetry boundary condition for the creeping flow and a no-flux boundary condition for the avidin is defined. The particle is represented by a half circle in e, at which a no-slip boundary condition for the flow is set, together with a flux condition by which the avidin adsorption is defined.

The transport of avidin throughout the buffer is modeled by the package *Transport of Diluted Species*. Based on the diffusion coefficient of avidin, which is taken to be 0.6×10^{-10} m² s⁻¹ [158], and the appropriate boundary conditions, the convection and diffusion of avidin is calculated. At the previously defined inlet, a constant avidin concentration $c_{\mathrm{Av,o}}$ is presumed. At the outlet the concentration gradient along the normal is set to zero. A no-flux boundary condition is set at the line D in Figure 6-6. At the particle a flux boundary condition is defined. The (outward) avidin flux is defined as the difference between the flux resulting from avidin adsorption onto and desorption from the particle surface:

$$\Phi = k_{\mathrm{ads}} c_{\mathrm{Av}} c_{\mathrm{s,Av}} - k_{\mathrm{des}} c_{\mathrm{s,Av}} . \tag{6.8}$$

In this equation k_{ads} and k_{des} represent the adsorption and desorption rate constant of the adsorption process (specific or non-specific). This flux definition at the particle surface is used to calculate the surface concentration of avidin onto the particle. To discard effects of any inhomogeneous adsorption on the particle surface, a surface diffusion coefficient of bound avidin was defined as 10^{-11} m² s⁻¹. In the case of non-specific binding, the values for k_{ads} and k_{des} come from a fit to the experimental results (see section6.3.5a.). In the case of specific binding, the desorption process is expected to be negligible, as was previously discussed. A discussion on the value for k_{ads} is discussed in the following section.

6.3.3 Time scales limiting surface adsorption

In general, two main phenomena can limit the binding kinetics of any species from bulk onto a surface [159]. Firstly, the binding can be reaction limited. In this case the transport of the species through diffusion and advection happens fast enough such that, around the particle, one finds the bulk concentration of the species. The rate of adsorption is solely determined by the balance between species adsorption onto and desorption from the surface. The second limit is encountered when the reaction rate is fast enough compared to the

species transport. The adsorption kinetics is then mainly determined by how fast the species can be delivered to the surface. In case of sufficiently low flow rates, the transport is mainly limited by diffusion of the species from the liquid to the surface of the particle. In this case, as the adsorption process takes place, the medium around the particle gets depleted from the species. Diffusion of this species towards the surface then enables the adsorption to continue. The time necessary for the species to reach the surface becomes larger as the adsorption continues and a decreasing adsorption rate is expected in a diffusion-limited regime. At higher flow rates the adsorption process becomes advection-limited: the species concentration gradient around the particle remains constant because it is balanced by the species delivered by the flow. The gradient makes for a diffusive flux of molecules towards the particle surface and the fixed concentration gradient makes that this flux is constant in time. In this regime the adsorption rate is thus a constant. The dimensionless Péclet number indicates whether the reaction is diffusion or advection limited. It is defined as

$$\mathrm{Pe}=\frac{ul}{D}, \tag{6.9}$$

where u is the local fluid velocity, l is a characteristic length scale of the microfluidic device and D is the diffusion coefficient of the species. In the case of Pe>>1, the transport is advection-limited, for Pe<<1 one has a diffusion-limited regime. For the device discussed here Pe=200 is calculated. This indicates that, in the case of transport limited kinetics, the advection of avidin molecules is the limiting factor on the adsorption rate.

6.3.4 Specific binding

a. Experimental results

The time-dependent specific binding of avidin onto a biotinylated polystyrene particle is observed well by bringing this particle from an avidin-free buffer solution to a solution containing a low (0.1 μmol/m^3 to 10 μmol/m^3) concentration of avidin. This measurement is done for a total of thirteen mixtures at different concentrations. Figure 6-7 displays the mobility of this particle as a function of time for seven of these measurements. The other measurements are not included in the figure for sake of clarity. The origin of the time scale coincides with the moment the particle crosses the boundary between the two liquids.

From the figure it is seen that, when the particle enters the avidin-containing solution, its mobility increases as a function of time. Moreover, the rate of increase depends clearly on the concentration of avidin in the final buffer: a larger avidin concentration accounts for a faster increase in mobility. This increase is due to the adsorption of avidin onto the particle. Moreover, at concentrations above 5 μmol/m^3, the particle mobility reaches a saturation value before the end of the experiment. This saturation mobility has the same value as the plateau observed in Figure 6-2 where the specific binding of avidin to the biotinylated particles was discussed. I recall that the occurrence of this plateau value was explained by associating this particle mobility with an avidin coverage of the particle in which all specific binding sites are occupied. This leads to stating that the adsorption process observed in Figure 6-7 is the specific binding of avidin onto biotin sites on the particle.

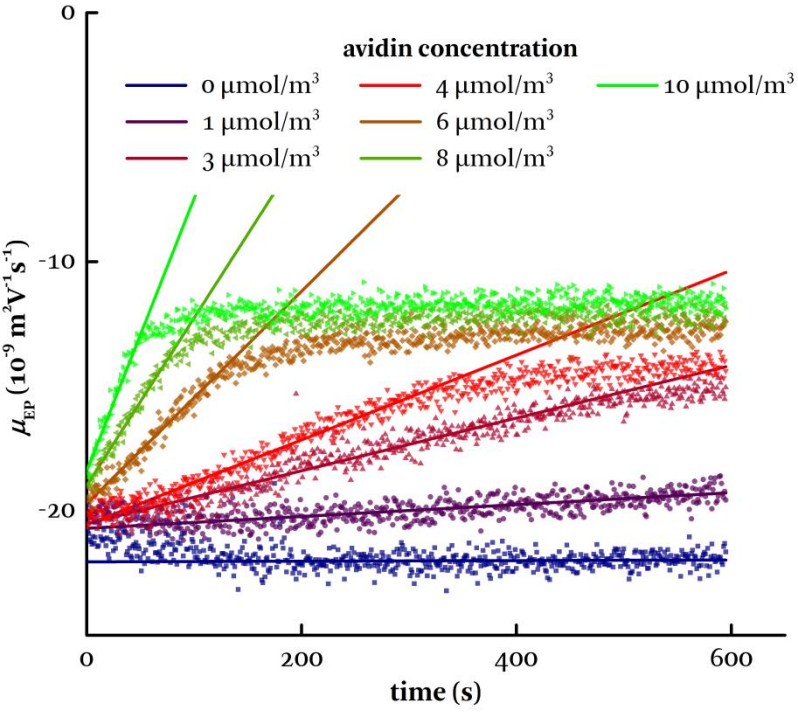

Figure 6-7: The time-dependent change in electrophoretic mobility when a biotinylated particle is transferred from an avidin-free to an avidin-containing buffer solution. At these concentrations the change in mobility is due to the specific adsorption of avidin onto the particle surface. The amount of absorbed molecules proves to be linear with time (solid lines), indicating the reaction kinetics is advection-limited.

b. Numerical simulations

Figure 6-8 presents the calculated surface concentration of avidin $c_{s,Av}$ on the particle as a function of time for various values of k_{ads}. As previously explained, k_{des} is taken at zero for the specific adsorption. The avidin concentration at the inlet is taken at 6 μmol/m^3 (400 ng/ml). It is seen that $c_{s,Av}$ increases monotonically with time until all binding sites are occupied, i.e. when a surface concentration of 0.31 amol is reached, after which $c_{s,Av}$ remains at this constant value. From the figure it is also concluded that as the surface coverage increases, the adsorption rate decreases. This decrease of adsorption rate is more pronounced at smaller values of k_{ads}. The degree of decrease is well characterized by the steepness of the transition between adsorption and saturation: a higher adsorption rate constant, giving an adsorption process less prone to a decrease in adsorption rate, delivers a steeper transition. Also the time necessary to obtain saturation is dependent on k_{ads}: saturation occurs faster when this parameter is higher. This decrease in adsorption rate is because the avidin flux towards the particle, as expressed by (6.8), is a function of the avidin surface concentration that is already present on the particle. However, the adsorption dynamics reaches a k_{ads}-independent characteristic for high enough k_{ads} (higher than 20×10^3 m^3 mol^{-1} s^{-1}). In this situation the flux towards the particle is only limited by the speed at which these molecules can be delivered to the particle by processes of convection and diffusion. This is exemplified in Figure 6-9 where the bulk avidin concentration profiles are depicted at a time t = 1 s for two values of the adsorption rate constant. It is seen that in both cases the flux boundary condition imposes a concentration gradient in the avidin around the particle. This concentration gradient ensures the supply of avidin molecules through diffusion to establish the flux boundary condition at the particle. At low k_{ads}, i.e. 10^3 m^3 mol^{-1} s^{-1}, the bulk avidin concentration near the particle surface is 4.15 μmol/m^3, while at k_{ads} equaling 10^5 m^3 mol^{-1} s^{-1} this concentration drops to 0.117 μmol/m^3. The maximal adsorption rate is obtained at the highest concentration gradient, i.e.

when the bulk avidin concentration at the particle surface is 0 µmol/m^3. An increasing k_{ads} approximates this situation at which the adsorption is only transport-limited.

Furthermore, the influence of the avidin concentration on the adsorption rate is modeled. Figure 6-10 presents the calculated flux of avidin molecules from the bulk to the particle surface as a function of the avidin concentration at the inlet. This is done at a time t = 1 s and for various values of the adsorption rate constant. It is seen than, for all values of k_{ads}, the influx of avidin molecules scales linearly with the avidin concentration. This is easily understood from the linearity of the diffusion process, described by Fick's law, delivering the molecules to the surface: an increase in concentration renders the same relative increase in species flux.

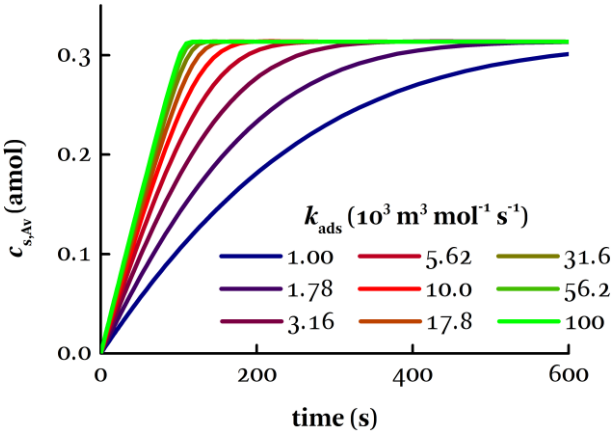

Figure 6-8: Simulated surface concentration of avidin $c_{s,Av}$ onto the particle as a function of time for different adsorption rate constants.

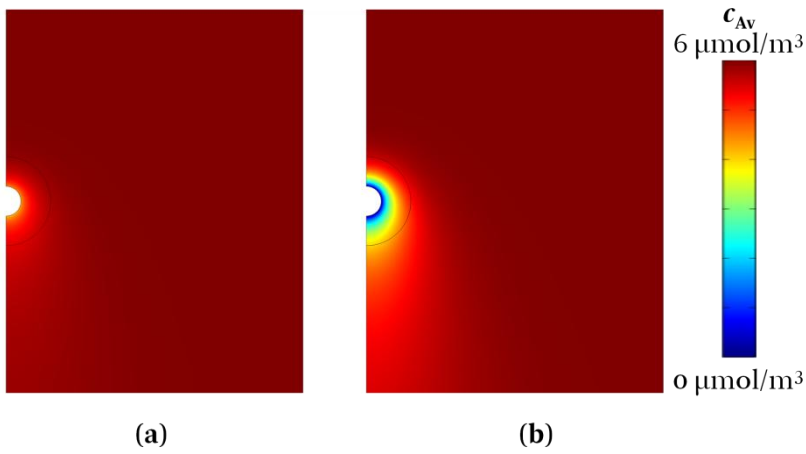

Figure 6-9: Simulated bulk avidin concentration profile in the case of specific adsorption onto the particle surface at t = 1 s for (a) k_{ads} = 10^3 m^3 mol^{-1} s^{-1} and (b) k_{ads} = 10^5 m^3 mol^{-1} s^{-1}.

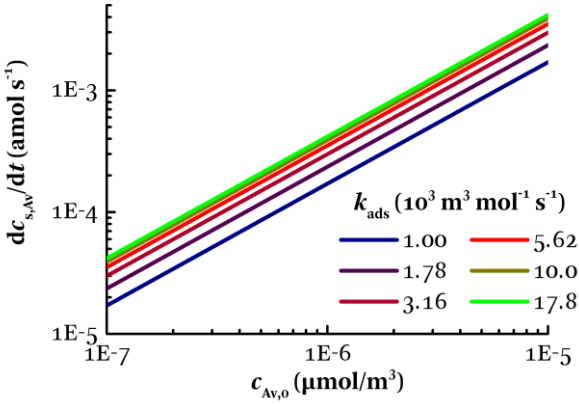

Figure 6-10: Adsorption rate of avidin molecules onto the particle as a function of the avidin concentration at the inlet $c_{Av,o}$ at time t = 1 s. For all values of the adsorption rate constant the adsorption rate increases linearly with $c_{Av,o}$.

c. Discussion

With the numerical simulations, the kinetics of the specific adsorption process was identified. Depending on the value of the adsorption rate constant the process is either solely transport-limited (in the case of large k_{ads}) or partly reaction limited (for k_{ads} of the order of 10^3 m^3 mol^{-1} s^{-1}). As was discussed, a purely advection-limited regime is characterized by a steep transition at the point of saturation, while a reaction-limited process shows a much smoother transition. Applying this to the measurements presented in Figure 6-7 one can conclude that the observed avidin adsorption is mainly advection limited: the increase in mobility is mostly linear and the transition towards the plateau is rather steep. Moreover, when looking at the $c_{Av,o}$ =6 µmol/m^3 solution, the time scale at which saturation occurs (120 s) is very close to the time scale retrieved from the numerical simulations for large k_{ads} (100 s). This further supports the premise that the adsorption process is advection limited.

Furthermore, the best-fit linear approximations to the data during which adsorption occurs, are given as solid lines in this figure. It is seen that these lines do not coincide exactly at t = 0 s. This is because the fitting of the experimental data at low concentrations ($c_{Av} \leq 3$ µmol/m^3) is done only after 200 s. When looking at the control experiment at which the particle is transported towards the same avidin-free buffer, one sees that during these initial 200 s the mobility decreases slightly. This can be due to the presence of chromium ions in the buffer solution due to electrode disintegration. These ions have typically a high valency and therefore could influence the electrokinetics of the particle.

It is clear from the figure that the adsorption rate, which is proportional to the slope of these lines, is dependent on the avidin concentration of the final buffer solution. This makes the property a good parameter to establish the avidin concentration in a solution. In Figure 6-11, the change of the mobility in time is plotted as a function of the avidin concentration. Note the log-log-scale used in this graph.

Also present on this graph are two lines to indicate the power law governing the concentration dependence of the adsorption rate. It is seen that for concentrations below 1 μmol/m^3, the adsorption rate increases linearly with the concentration of avidin in the solution. This is what is expected in an advection-limited system, as was already discussed with Figure 6-10. At concentrations above 1 μmol/m^3, however, the adsorption rate increases quadratically with an increasing concentration, which is not expected on the basis of species transport. This anomalous quadratic dependence is presently unexplained. Considering the fitting parameters given in Table 6-1, it is possible to relate the rate of mobility change to an influx of avidin molecules. This has been added as a second scale on Figure 6-11. For concentrations below 1 μmol/m^3, the measured adsorption rates are a factor two lower lower than the rate calculated in Figure 6-10 at high k_{ads}. The most striking difference between these two graphs is, again, the appearance of the quadratic behavior in the measured adsorption rate. Besides this, a good correspondence between the numerical simulations and the measurements exists.

The limit of detection of a concentration measurement is determined by the standard error on the estimate of the adsorption rate obtained from the linear fit, i.e. $\sigma_{\partial_t \mu}$. This error is calculated as a diagonal element of the covariance matrix and is given by

$$\sigma^2_{\partial_t \mu} = \frac{1}{N-1}\frac{\sigma^2_\mu}{\sigma^2_t}, \tag{6.10}$$

with N the number of data points, σ_t^2 the variance on the time steps and σ_μ^2 given by equation (3.20). For a measurement time of 10 minutes at the applied field strength, this standard error calculated to be 6.1×10^{-14} m^{2}V^{-1}s^{-2}. Assuming a linear concentration dependence of the adsorption rate, the theoretical limit of detection is established at approximately 0.03 mol/m^3 or 2 ng/ml. This value is comparable with benchmarks given with optical label-free detection methods [160], [161].

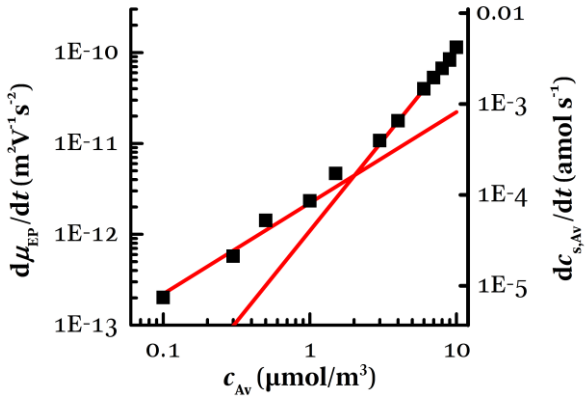

Figure 6-11: The change in mobility retrieved from the linear fits presented in Figure 6-7. The axis on the right provides a conversion to avidin flux towards the particle, based on the parameters given in Table 6-1. The red solid lines are guides to the eye to reveal the power dependence of the adsorption rate to the avidin concentration. For concentrations below 1 µmol/m^3, a linear dependence emerges, which is expected in the case of advection-limited adsorption. The quadratic dependence at higher concentration is unexpected and currently unexplained.

6.3.5 Non-specific binding

a. Experimental results

When performing the same adsorption experiments at higher avidin concentrations (from 30 μmol/m^3 to 1600 μmol/m^3), non-specific adsorption can be observed. A total of ten different mixtures were considered and the time-dependent mobility measurements of five of these mixtures are presented in Figure 6-12. Again, the origin of the time axis corresponds approximately with the time at which the particle crosses the boundary between the avidin-free and avidin-rich medium. Immediately after this crossing, i.e. during the first few seconds presented in the graph, the mobility shows a steep increase. This is the specific adsorption of avidin discussed in the previous subsection which takes place much faster than in Figure 6-7 because of the considerably higher concentrations of avidin. After this initial increase due to specific adsorptions, the mobility of the particle increases further at a longer time scale. After some time, the mobility approaches a constant value. This constant value is observable at the time scales presented in the graph for concentrations above 100 μmol/m^3. It is clear that the precise value of this constant mobility depends on the concentration of avidin in the solution. This is what is expected from the steady-state adsorption model presented in section 6.2.4: the non-specific adsorption follows a Langmuir isotherm describing the balance between adsorption and desorption in equilibrium. The amount of avidin bound to the particle depends on the concentration of the buffer solution around the particle, explaining the concentration dependence of the steady-state mobility observed in Figure 6-12.

To further support this Langmuir adsorption model, a desorption experiment is performed in which the mobility of a biotinylated particle changes when it moves from an avidin-rich medium to a buffer without avidin. The concentration of avidin in the initial medium is taken such that all specific and non-specific sites are occupied according to the model presented in section 6.2.4. The

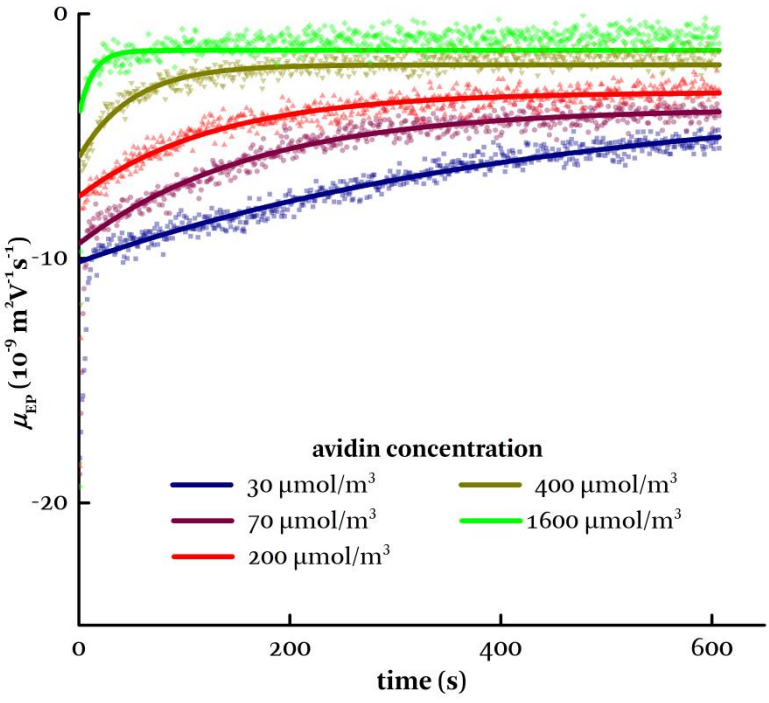

Figure 6-12: Non-specific binding is observed when the biotinylated particle enters a medium with a sufficiently high concentration of avidin. The aforementioned specific binding at these concentrations happens on a time scale of a few seconds, which is barely visible in the graph. The time-dependence of the mobility change is fitted as an exponential (solid lines), indicating a reaction-limited adsorption process.

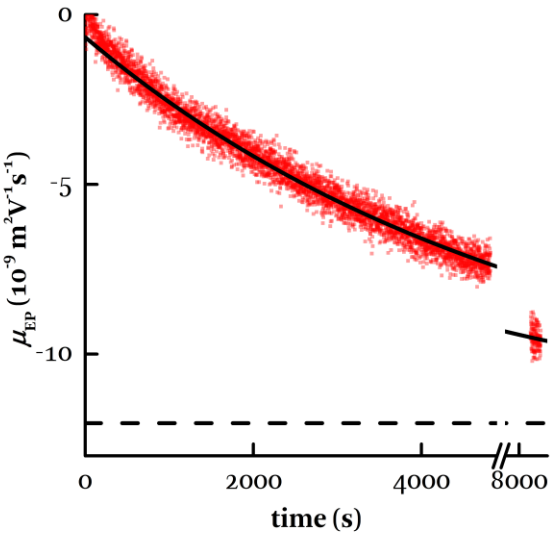

Figure 6-13: Desorption of non-specifically bound avidin occurs when transferring the biotinylated particle from an avidin-rich to an avidin-free medium. Again, an exponential time-dependence is fitted (solid line). The steady-state value, indicated by the dashed line, agrees with the mobility of a particle containing only specifically bound avidin.

measured change in mobility, observed when the particle enters the avidin-free buffer, is depicted in Figure 6-13. The graph presents the mobility recorded for the first 4500 s after the particle crosses the boundary between the two liquids. Additionally, the mobility of the same particle is measured at 8300 s for about 100 s. The mobility in between these two times was not recorded. The decrease in electrophoretic mobility of the particle is explained by desorption of non-specifically bound avidin.

Furthermore, it is possible to quantify the reaction rates that govern the non-specific adsorption. Note, firstly, that the adsorption process as a function of time cannot be described by a linear approximation.

This means the advection-limited regime is not valid to describe the adsorption kinetics as is the case with specific adsorption. Rather, the process is reaction limited. The reaction expressed by (6.3) is governed by a forward (adsorption) reaction rate constant and a reverse (desorption) reaction rate constant, k_{ads} (unit: $m^3\ mol^{-1}\ s^{-1}$) and k_{des} (unit: s^{-1}) respectively. They describe the reaction kinetics happening at the surface of the particle [159]:

$$\frac{d\phi_{NS}}{dt} = k_{ads} c_{Av} \left(1 - \phi_{NS}\right) - k_{des} \phi_{NS} . \tag{6.11}$$

Again, the notation ϕ_{NS} is used to indicate the fraction of non-specific binding sites on the particle to which an avidin molecule is bound. Note that, since a reaction-limited regime is presumed, the avidin concentration at the surface of the particle is taken the same as the bulk concentration. This differential equation is solved as

$$\phi_{NS} = \frac{K c_{Av}}{1 + K c_{Av}} \left(1 - \exp\left(-\left(k_{ads} c_{Av} + k_{des}\right) t\right)\right). \tag{6.12}$$

Here $K = k_{ads}/k_{des}$ constitutes the equilibrium constant that governs the Langmuir isotherm. Indeed, the steady-state value of the number of bound non-specific sites is given by this isotherm.

The desorption rate constant is retrieved by fitting an exponential function to the measured mobility in Figure 6-13. To achieve a good fit, it was necessary to ignore the first 600 data points. The discrepancy between the fit and the data at these points may indicate a second, less important and faster, desorption process takes place. Possible origins of this faster desorption could be a second layer of adsorbed avidin molecules present on top of the avidin layer bound to the surface. In any case, since the discrepancy with the fit is small, no further attention is given to it. From the fit, the desorption rate constant k_{des} is established at $(1.77 \pm 0.02) \times 10^{-4}\ s^{-1}$. The fit also establishes a steady-state value for the mobility ($-12.3 \times 10^{-9}\ m^2 V^{-1} s^{-1}$),

indicated by a dashed line in Figure 6-13) which corresponds well with the value of the mobility at which only specific binding sites are occupied. Similar exponential fits can be obtained for the adsorption experiments. They are presented as solid lines in Figure 6-12. The fit values for $k_{ads}c_{Av} + k_{des}$ as a function of the avidin concentration are plotted in Figure 6-14, together with a linear fit to these data points which has an R-squared value of 0.9421. Note the log-log-scale of this figure. k_{ads} is determined at 52 ± 5 $m^3\,mol^{-1}\,s^{-1}$ and k_{des} is fitted as $(1.7\pm2.7)\times10^{-3}$ s^{-1}. Note that this last parameter is not well estimated based on the adsorption experiments but is well characterized from the fit in the desorption experiment. From this the equilibrium constant of the reaction is calculated to be 282×10^3 $m^3\,mol^{-1}$. This value differs from the equilibrium constant presented in Table 6-1, possibly because, as previously discussed, the model explaining the affinity experiments does not take into account avidin adsorption onto the microfluidic walls.

b. Comparison with numerical modeling

Since the values for k_{ads} and k_{des} come directly from the measurements, numerical simulations are only necessary to verify the condition of a reaction-limited regime, i.e. that no significant avidin concentration gradient is present around the particle. Indeed, in the concentration regimes considered in Figure 6-12, the calculations confirm that the concentration of avidin at the particle surface never differs at most 3 % from the bulk concentration value.

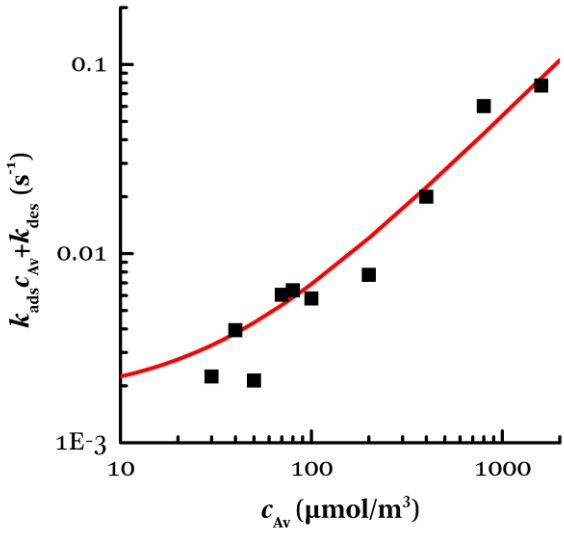

Figure 6-14: The time constant of the exponential fits presented in Figure 6-12 is a linear function of the avidin concentration. The adsorption and desorption rate constants are parameters of for this linear fit, presented as the solid line. Note the log-log scale used in this figure.

6.4 Conclusions

I have performed biosensing experiments in which OTE of a biotinylated particle was used to determine the concentration of avidin in a buffer solution. Two types of mobility measurements were discussed. From the steady-state mobility measurements an adsorption model was retrieved. This model describes the avidin adsorption to result from two distinct mechanisms: specific adsorption is dominant at low avidin concentrations (below 0.6 μmol/m^3) and involves the binding of avidin molecules to the biotin receptors on the particle surface. At higher concentrations of avidin also non-specific binding occurs which is governed by a Langmuir isotherm. The non-specificity is supported by the fact that the same Langmuir isoterm is observed with non-functionalized particles.

Time-dependent mobility measurements together with numerical modeling unraveled the binding kinetics of the adsorption process. The specific adsorption of avidin is advection-limited. The adsorption rate shows a linear dependence on the avidin concentration at concentrations below 1 μmol/m^3, which is expected in an advection-limited regime. However, an anomalous quadratic dependence is observed at higher avidin concentrations. The theoretical limit of detection of the experimental system is 0.03 μmol/m^3 (2 ng/ml). Similar adsorption experiments at higher avidin concentrations revealed the reaction kinetics of non-specific adsorption. This mechanism is reaction-limited and governed by an adsorption and desorption rate. The values for these parameters are 52 ± 5 m^3 mol^{-1} s^{-1} and $(1.77 \pm 0.02) \times 10^{-4}$ s^{-1}, respectively. Overall, a good quantitative agreement was found between the numerical simulations and the measurements, aside for the occurrence of a quadratic concentration dependence of the specific adsorption rate.

The avidin-biotin system is considered a model system for a receptor/ligand binding and these experiments give an indication of the feasibility of optical trapping electrophoresis as a label-free

detection technique for proteins. Future work could be directed towards investigating other biochemical systems by changing the surface modification of the used microspheres.

Chapter 7
Conclusions and perspectives

7.1 Conclusions

This dissertation has explored the possibility of using optical trapping electrophoresis (OTE) as a label-free biosensor. The method uses the electrophoretic mobility of an optically trapped functionalized particle as a measure for the concentration of a target analyte in the suspension. To achieve reproducible results with this method, I have introduced two calibration procedures. Firstly, I have shown that heating effects taking place during an experiment can be monitored by analyzing the Brownian motion of the optically trapped particle. This has allowed to assess Joule heating resulting from the electric field, which was shown to cause a significant temperature increase (i.e. several K) in the used microfluidic device at salt concentrations exceeding 15 g/l and applied RMS-voltages higher than 20 V. The accuracy and precision of this measurement method were established at 15% and 0.9 K, respectively. Furthermore it was demonstrated that transient heating processes can be monitored with this technique, albeit with a limited time resolution. Also heating due to laser absorption has been explored in a similar manner and was shown to be negligible even at maximal beam power.

I have also devised a calibration method to compensate for the influence of electroosmotic flow (EOF) on the mobility measurement when performing OTE. It was shown that from this calibration a map of the EOF inside the microfluidic device is obtained. From the calibration procedure the ζ-potential of the microfluidic wall emerges, which makes that, in general, the procedure can be employed to monitor the electrical properties of microfluidic walls. This has been demonstrated in an experiment in which the influence of the salt concentration on the electrical surface properties was evaluated. This experiment showed a quantitative agreement with theoretical predictions.

Finally, I have performed biosensing experiments that monitor the adsorption of avidin onto biotinylated particles. From steady-state mobility measurements of these particles in mixtures containing

various amounts of avidin I have constructed an adsorption model. Two adsorption mechanisms were identified: specific adsorption only occurs with the biotinylated particles and is dominant at relatively low avidin concentrations (< 0.6 μmol/m^3) and is caused by the binding of avidin to the biotin sites present on the particle. Non-specific adsorption is observed with both bare and biotinylated particles at comparably high avidin concentrations (> 1 μmol/m^3) and is shown to be governed by a Langmuir isotherm. This proposed model describes the electrophoretic mobility of these particles accurately over four orders of magnitude of the avidin concentration. Furthermore, time-dependent measurements were undertaken by transferring a particle from one buffer solution to another solution containing a different avidin concentration. Together with the numerical modeling of the experiment, these measurements have allowed me to unravel the reaction kinetics behind the two adsorption processes. Specific adsorption has proven to occur fast and to be advection-limited, while non-specific adsorption is reaction limited and happens on a much longer time scale. Analysis of these time dependencies has allowed me to establish the limit of detection in the used measurement system as 0.03 μmol/m^3.

7.2 Perspectives

The experiments performed for this thesis show that specific detection of a target analyte is indeed possible with OTE. However, this research has merely shown the possibility of the technique for these biosensing applications. The road towards useful and practical biosensors based on OTE is still a long one.

Future research directions should, in my opinion, be focused on two distinct fields. Firstly an application should be found in which OTE can prove its merits over other existing techniques. While the avidin-biotin system, characterized in this dissertation, is a model system often used to inspect new biosensing technologies, its practical relevance is limited. Moreover, other sensing technologies achieve similar benchmarks regarding limit-of-detection and sensitivity as this system. I would advocate testing the technology on a biologically more relevant system, which does not necessarily show the high binding affinity the avidin-biotin system offers. In selecting this system one should consider one of the advantages of the OTE technique: it can measure small molecules, as long as they are sufficiently charged. For example optical methods typically rely on the overlap of a light mode with the molecule. The signal retrieved from these biosensors directly scales with the volume of the analyte, which typically imposes a limit in terms of minimal molecular weight of these molecules. The detection of small biomolecules is not trivial with the current available methods, and OTE could offer new capabilities in that field.

As a second focus, the technological advancement of the measurement system should be considered. Currently, the OTE experiments rely on an exhaustive optical setup that needs to be regularly realigned during the course of an experiment. Also, calibration procedures for e.g. electroosmosis are required to obtain reliable quantitative measurements. This makes that OTE in its present form is far from a practical biosensor, both in construction and operation. On-chip integration could resolve the demanding

optical calibration and particle manipulation. However advances on on-chip optical tweezers are rather scarce. This makes that the practical realization of these integrated tweezers is still a long way ahead and could be considered as a research topic on its own. Finally, problems encountered as a result of electroosmosis could be eliminated by applying surface passivation, e.g. a silanization procedure, to remove surface charge from the microfluidic walls. Together with this, adsorption of ionic species from the sample onto these walls should be prevented, which may require adapted low-fouling layers.

Bibliography

[1] J. Kirsch, C. Siltanen, Q. Zhou, A. Revzin, and A. Simonian, "Biosensor technology: recent advances in threat agent detection and medicine.," *Chem. Soc. Rev.*, vol. 42, no. 22, pp. 8733–8768, 2013.

[2] L. C. Clark and C. Lyons, "Electrode systems for continuous monitoring in cardiovascular surgery," *Ann. N. Y. Acad. Sci.*, vol. 102, no. 1, pp. 29–45, 1962.

[3] J. Wang, "Electrochemical glucose biosensors," *Electrochem. Sensors, Biosens. their Biomed. Appl.*, pp. 57–69, 2008.

[4] P. Kozma, F. Kehl, E. Ehrentreich-Förster, C. Stamm, and F. F. Bier, "Integrated planar optical waveguide interferometer biosensors: A comparative review," *Biosens. Bioelectron.*, vol. 58, pp. 287–307, 2014.

[5] M. F. Juette, D. S. Terry, M. R. Wasserman, Z. Zhou, R. B. Altman, Q. Zheng, and S. C. Blanchard, "The bright future of single-molecule fluorescence imaging," *Curr. Opin. Chem. Biol.*, vol. 20, no. 1, pp. 103–111, 2014.

[6] H. K. Hunt and A. M. Armani, "Label-free biological and chemical sensors.," *Nanoscale*, vol. 2, no. 2001, pp. 1544–1559, 2010.

[7] W. Pang, H. Zhao, E. S. Kim, H. Zhang, H. Yu, and X. Hu, "Piezoelectric microelectromechanical resonant sensors for chemical and biological detection," *Lab Chip*, vol. 12, no. 1, pp. 29–44, 2012.

[8] A. J. Qavi, A. L. Washburn, J. Y. Byeon, and R. C. Bailey, "Label-free technologies for quantitative multiparameter biological analysis," *Anal. Bioanal. Chem.*, vol. 394, pp. 121–135, 2009.

[9] Y.-S. Sun, "Optical Biosensors for Label-Free Detection of Biomolecular Interactions," *Instrum. Sci. Technol.*, vol. 42, no. 2, pp. 109–127, 2014.

[10] V. Tsouti, C. Boutopoulos, I. Zergioti, and S. Chatzandroulis, "Capacitive microsystems for biological sensing," *Biosens. Bioelectron.*, vol. 27, no. 1, pp. 1–11, 2011.

[11] S. Nahavandi, S. Baratchi, R. Soffe, S.-Y. Tang, S. Nahavandi, A. Mitchell, and K. Khoshmanesh, "Microfluidic platforms for biomarker analysis.," *Lab Chip*, vol. 14, no. 9, pp. 1496–1514, 2014.

[12] C. P. Y. Chan, W. C. Mak, K. Y. Cheung, K. K. Sin, C. M. Yu, T. H. Rainer, and R. Renneberg, "Evidence-based point-of-care diagnostics: current status and emerging technologies.," *Annu. Rev. Anal. Chem. (Palo Alto. Calif).*, vol. 6, no. March, pp. 191–211, 2013.

[13] J. F. Rusling, C. V Kumar, J. S. Gutkind, and V. Patel, "Measurement of biomarker proteins for point-of-care early detection and monitoring of cancer.," *Analyst*, vol. 135, no. 10, pp. 2496–2511, 2010.

[14] P. Neuži, S. Giselbrecht, K. Länge, T. J. Huang, and A. Manz, "Revisiting lab-on-a-chip technology for drug discovery," *Nat. Rev. Drug Discov.*, vol. 11, no. 8, pp. 620–632, 2012.

[15] M. a Cooper, "Optical biosensors in drug discovery.," *Nat. Rev. Drug Discov.*, vol. 1, no. 7, pp. 515–528, 2002.

[16] O. Lazcka, F. J. Del Campo, and F. X. Muñoz, "Pathogen detection: A perspective of traditional methods and biosensors," *Biosens. Bioelectron.*, vol. 22, no. 7, pp. 1205–1217, 2007.

[17] G.-J. Zhang, L. Zhang, M. J. Huang, Z. H. H. Luo, G. K. I. Tay, E.-J. A. Lim, T. G. Kang, and Y. Chen, "Silicon nanowire biosensor for highly sensitive and rapid detection of Dengue virus," *Sensors Actuators B Chem.*, vol. 146, no. 1, pp. 138–144, 2010.

[18] A. Chen and S. Yang, "Replacing Antibodies With Aptamers In Lateral Flow Immunoassay," *Biosens. Bioelectron.*, vol. 71, pp. 230–242, 2015.

[19] G. Poste, "Bring on the biomarkers.," *Nature*, vol. 469, no. 7329, pp. 156–157, 2011.

[20] J. L. Arlett, E. B. Myers, and M. L. Roukes, "Comparative advantages of mechanical biosensors.," *Nat. Nanotechnol.*, vol. 6, no. 4, pp. 203–215, 2011.

[21] N. Chartuprayoon, M. Zhang, W. Bosze, and N. V. Myung, "One-dimensional nanostructures based bio-detection," *Biosens. Bioelectron.*, vol. 63, pp. 432–443, 2014.

[22] D. Mark, S. Haeberle, G. Roth, F. von Stetten, and R. Zengerle, "Microfluidic lab on a chip platforms: requirements, characteristics and applications," *Chem. Soc. Rev.*, vol. 39, no. 3, pp. 1153–1182, 2010.

[23] N. Garbow, M. Evers, and T. Palberg, "Optical tweezing electrophoresis of isolated, highly charged colloidal spheres," *Colloids Surfaces A Physicochem. Eng. Asp.*, vol. 195, no. 1–3, pp. 227–241, 2001.

[24] N. Garbow, M. Evers, T. Palberg, and T. Okubo, "On the electrophoretic mobility of isolated colloidal spheres," *J. Phys. Condens. Matter*, vol. 16, no. 23, pp. 3835–3842, 2004.

[25] G. Seth Roberts, T. a Wood, W. J. Frith, and P. Bartlett, "Direct measurement of the effective charge in nonpolar suspensions by optical tracking of single particles.," *J. Chem. Phys.*, vol. 126, no. 19, p. 194503, May 2007.

[26] F. Beunis, F. Strubbe, K. Neyts, and D. Petrov, "Beyond Millikan: The dynamics of charging events on individual colloidal particles," *Phys. Rev. Lett.*, vol. 108, no. January, p. 016101, 2012.

[27] F. Strubbe, P. J. M. Vanbrabant, F. Beunis, B. Verboven, M. Karvar, and K. Neyts, "In-plane electrophoresis in nonpolar liquids: Measurements and simulations," *Colloids Surfaces A Physicochem. Eng. Asp.*, vol. 376, no. 1–3, pp. 89–96, 2011.

[28] F. Strubbe, F. Beunis, T. Brans, M. Karvar, W. Woestenborghs, and K. Neyts, "Electrophoretic Retardation of Colloidal Particles in Nonpolar Liquids," *Phys. Rev. X*, vol. 3, no. 2, p. 021001, Apr. 2013.

[29] R. Galneder, V. Kahl, A. Arbuzova, M. Rebecchi, J. O. Rädler, and S. McLaughlin, "Microelectrophoresis of a bilayer-coated silica bead in an optical trap: application to enzymology.," *Biophys. J.*, vol. 80, no. 5, pp. 2298–2309, May 2001.

[30] V. Kahl, a Gansen, R. Galneder, and J. O. Rädler, "Microelectrophoresis in a laser trap: a platform for measuring electrokinetic interactions and flow properties within microstructures.," *Rev. Sci. Instrum.*, vol. 80, no. 7, p. 073704, Jul. 2009.

[31] J. A. van Heiningen and R. J. Hill, "Polymer adsorption onto a microsphere from optical tweezers electrophoresis.," *Lab Chip*, vol. 11, no. 1, pp. 152–162, Jan. 2011.

[32] J. A. Van Heiningen and R. J. Hill, "Poly(ethylene oxide) adsorption onto and desorption from silica microspheres: New insights from optical tweezers electrophoresis," *Macromolecules*, vol. 44, pp. 8245–8260, 2011.

[33] R. J. Hunter, *Foundations of Colloid Science*, Second. Oxford University Press, 2001.

[34] J. Lyklema, *Fundamentals of Interface and Colloid Science: Solid-Liquid Interfaces*. Elsevier Science, 1995.

[35] I. D. Morrison and S. Ross, *Colloidal Dispersions: Suspensions, Emulsions, and Foams*. Wiley, 2002.

[36] J. H. Masliyah and S. Bhattacharjee, *Electrokinetic and Colloid Transport Phenomena*. Wiley, 2006.

[37] D. J. Shaw and B. Costello, *Introduction to colloid and surface chemistry*, Fourth. Elsevier, 1993.

[38] G. G. Stokes, “On the Effect of the Internal Friction of Fluids on the Motion of Pendulums,” *Trans. Cambridge Philos. Soc.*, vol. 9, no. 11, pp. 8–14, 1851.

[39] K. Berg-Sørensen and H. Flyvbjerg, “The colour of thermal noise in classical Brownian motion: A feasibility study of direct experimental observation,” *New J. Phys.*, vol. 7, p. 38, 2005.

[40] H. Faxén, “Der Widerstand gegen die Bewegung einer starren Kugel in einer zähen Flüssigkeit, die zwischen zwei parallelen ebenen Wänden eingeschlossen ist,” *Ann. Phys.*, vol. 373, no. 10, pp. 89–119, Jan. 1922.

[41] D. S. Lemons, A. Gythiel, and I. Langevin, “Paul Langevin ’ s 1908 paper ‘“ On the Theory of Brownian Motion ,”’” *Am. J. Phys.*, vol. 65, no. 11, pp. 1079–1081, 1997.

[42] N. Pottier, *Nonequilibrium Statistical Physics: Linear Irreversible Processes*. Oxford University Press, 2009.

[43] G. E. Uhlenbeck and L. S. Ornstein, “On the theory of the Brownian motion,” *Phys. Rev.*, vol. 36, pp. 823–841, 1930.

[44] M. C. Wang and G. E. Uhlenbeck, “On the Theory of Brownian Motion II,” *Rev. Mod. Phys.*, vol. 17, no. 2–3, pp. 323–342, 1945.

[45] a. V. Delgado, F. González-Caballero, R. J. Hunter, L. K. Koopal, and J. Lyklema, “Measurement and interpretation of electrokinetic phenomena,” *J. Colloid Interface Sci.*, vol. 309, pp. 194–224, 2007.

[46] H. Li, S. Wei, C. Qing, and J. Yang, “Discussion on the position of the shear plane,” *J. Colloid Interface Sci.*, vol. 258, pp. 40–44, 2003.

[47] W. Ding, X. Liu, L. Song, Q. Li, Q. Zhu, H. Zhu, F. Hu, Y. Luo, L. Zhu, and H. Li, “An approach to estimate the position of the shear plane for colloidal particles in an electrophoresis experiment,” *Surf. Sci.*, vol. 632, pp. 50–59, 2015.

[48] M. Borkovec, I. Szilagyi, I. Popa, M. Finessi, P. Sinha, P. Maroni, and G. Papastavrou, “Investigating forces between charged particles in the presence of oppositely charged polyelectrolytes with the multi-particle colloidal probe technique,” *Adv. Colloid Interface Sci.*, vol. 179–182, pp. 85–98, 2012.

[49] S. K. Sainis, V. Germain, and E. R. Dufresne, “Statistics of particle trajectories at short time intervals reveal fN-scale colloidal forces,” *Phys. Rev. Lett.*, vol. 99, no. 1, pp. 1–4, 2007.

[50] J. Crocker and D. Grier, “Methods of Digital Video Microscopy for Colloidal Studies,” *J. Colloid Interface Sci.*, vol. 179, no. 179, pp. 298–310, 1996.

[51] M. Kosmulski and J. B. Rosenholm, “High ionic strength electrokinetics,” *Adv. Colloid Interface Sci.*, vol. 112, no. 1–3, pp. 93–107, 2004.

[52] H. Ohshima, "A Simple Expression for Henry's Function for the Retardation Effect in Electrophoresis of Spherical Colloidal Particles," *Journal of Colloid and Interface Science*, vol. 168. pp. 269–271, 1994.

[53] H. Ohshima, T. W. Healy, and L. R. White, "Approximate analytic expressions for the electrophoretic mobility of spherical colloidal particles and the conductivity of their dilute suspensions," *J. Chem. Soc. Faraday Trans. 2*, vol. 79, no. 11, pp. 1613–1628, 1983.

[54] H. Ohshima, "Electrophoresis of soft particles," *Adv. Colloid Interface Sci.*, vol. 62, pp. 189–235, 1995.

[55] R. W. O'Brien and L. R. White, "Electrophoretic mobility of a spherical colloidal particle," *J. Chem. Soc. Faraday Trans. 2*, vol. 74, pp. 1607–1626, 1978.

[56] R. J. Hill and D. A. Saville, "'Exact' solutions of the full electrokinetic model for soft spherical colloids: Electrophoretic mobility," *Colloids Surfaces A Physicochem. Eng. Asp.*, vol. 267, pp. 31–49, 2005.

[57] H. Ohshima, "Theory of electrostatics and electrokinetics of soft particles," *Sci. Technol. Adv. Mater.*, vol. 10, p. 63001, 2009.

[58] D. a. A. Saville, "Electrokinetic Properties of Fuzzy Colloidal Particles," *J. Colloid Interface Sci.*, vol. 222, pp. 137–145, 2000.

[59] R. J. Hill, D. A. Saville, and W. B. Russel, "Electrophoresis of spherical polymer-coated colloidal particles," *J. Colloid Interface Sci.*, vol. 258, pp. 56–74, 2003.

[60] G. Kopp and J. L. Lean, "A new, lower value of total solar irradiance: Evidence and climate significance," *Geophys. Res. Lett.*, vol. 38, no. January, p. L01706, 2011.

[61] O. M. Maragò, P. H. Jones, P. G. Gucciardi, G. Volpe, and A. C. Ferrari, "Optical trapping and manipulation of nanostructures.," *Nat. Nanotechnol.*, vol. 8, no. 11, pp. 807–819, 2013.

[62] K. Ajito and K. Torimitsu, "Single nanoparticle trapping using a Raman tweezers microscope," *Appl. Spectrosc.*, vol. 56, no. 4, pp. 541–544, 2002.

[63] E. Vergucht, T. Brans, F. Beunis, J. Garrevoet, M. De Rijcke, S. Bauters, D. Deruytter, M. Vandegehuchte, I. Van Nieuwenhove, C. Janssen, M. Burghammer, and L. Vincze, "In vivo X-ray elemental imaging of single cell model organisms manipulated by laser-based optical tweezers," *Sci. Rep.*, vol. 5, p. 9048, 2015.

[64] A. Ashkin, "Acceleration and Trapping of Particles by Radiation Pressure," *Phys. Rev. Lett.*, vol. 24, no. 4, pp. 156–159, Jan. 1970.

[65] A. Ashkin and J. M. Dziedzic, "Optical Levitation by Radiation Pressure," *Appl. Phys. Lett.*, vol. 19, no. 8, pp. 283–285, 1971.

[66] A. Ashkin, J. M. Dziedzic, J. E. Bjorkholm, and S. Chu, "Observation of a single-beam gradient force optical trap for dielectric particles.," *Opt. Lett.*, vol. 11, no. 5, pp. 288–290, 1986.

[67] M. J. Lang and S. M. Block, "Resource Letter: LBOT-1: Laser-based optical tweezers," *Am. J. Phys.*, vol. 71, no. 3, pp. 201–215, 2003.

[68] R. W. Bowman and M. J. Padgett, "Optical trapping and binding.," *Rep. Prog. Phys.*, vol. 76, p. 026401, 2013.

[69] J. Hilario and S. C. Kowalczykowski, "Visualizing protein-DNA interactions at the single-molecule level," *Curr. Opin. Chem. Biol.*, vol. 14, pp. 15–22, 2010.

[70] S. Forth, M. Y. Sheinin, J. Inman, and M. D. Wang, "Torque measurement at the single-molecule level.," *Annu. Rev. Biophys.*, vol. 42, pp. 583–604, 2013.

[71] Y. Pang and R. Gordon, "Optical trapping of a single protein," *Nano Lett.*, vol. 12, pp. 402–406, 2012.

[72] M.-C. Zhong, X.-B. Wei, J.-H. Zhou, Z.-Q. Wang, and Y.-M. Li, "Trapping red blood cells in living animals using optical tweezers.," *Nat. Commun.*, vol. 4, p. 1768, 2013.

[73] A. G. Hendricks, E. L. F. Holzbaur, and Y. E. Goldman, "Force measurements on cargoes in living cells reveal collective dynamics of microtubule motors," *Proc. Natl. Acad. Sci.*, vol. 109, no. 45, pp. 18447–18452, 2012.

[74] É. Roldán, I. a. Martínez, J. M. R. Parrondo, and D. Petrov, "Universal features in the energetics of symmetry breaking," *Nat. Phys.*, vol. 10, no. June, pp. 457–461, 2014.

[75] A. Ashkin, "Forces of a single-beam gradient laser trap on a dielectric sphere in the ray optics regime.," *Methods Cell Biol.*, vol. 61, no. 2, pp. 569–582, 1992.

[76] T. A. Nieminen, N. du Preez-Wilkinson, A. B. Stilgoe, V. L. Y. Loke, A. A. M. Bui, and H. Rubinsztein-Dunlop, "Optical tweezers: Theory and modelling," *J. Quant. Spectrosc. Radiat. Transf.*, vol. 146, pp. 59–80, 2014.

[77] A. Callegari, M. Mijalkov, and G. Volpe, "Computational toolbox for optical tweezers in geometrical optics," vol. 32, no. 5, pp. B11–B19, 2015.

[78] M. Dienerowitz, M. Mazilu, and K. Dholakia, "Optical manipulation of nanoparticles: a review," *J. Nanophotonics*, vol. 2, no. September, p. 021875, 2008.

[79] D. B. Phillips, M. J. Padgett, S. Hanna, Y.-L. D. Ho, D. M. Carberry, M. J. Miles, and S. H. Simpson, "Shape-induced force fields in optical trapping," *Nat. Photonics*, vol. 8, no. May, pp. 400–405, 2014.

[80] T. A. Nieminen, V. L. Y. Loke, A. B. Stilgoe, G. Knöner, A. M. Brańczyk, N. R. Heckenberg, and H. Rubinsztein-Dunlop, "Optical tweezers computational toolbox," *J. Opt. A Pure Appl. Opt.*, vol. 9, no. 8, pp. S196–S203, 2007.

[81] T. a. Nieminen, H. Rubinsztein-Dunlop, and N. R. Heckenberg, "Calculation of the T-matrix: General considerations and application of the point-matching method," *J. Quant. Spectrosc. Radiat. Transf.*, vol. 79–80, pp. 1019–1029, 2003.

[82] P. Bartlett and S. Henderson, "Three-dimensional force calibration of a single-beam optical gradient trap," *J. Phys. Condens. Matter*, vol. 14, no. 33, pp. 7757–7768, Aug. 2002.

[83] T. a. Nieminen, H. Rubinsztein-Dunlop, and N. R. Heckenberg, "Multipole expansion of strongly focussed laser beams," *J. Quant. Spectrosc. Radiat. Transf.*, vol. 79–80, pp. 1005–1017, 2003.

[84] T. a Nieminen, N. R. Heckenberg, and H. Rubinsztein-Dunlop, "Forces in optical tweezers with radially and azimuthally polarized trapping beams.," *Opt. Lett.*, vol. 33, no. 2, pp. 122–124, 2008.

[85] H. Deschout, F. Cella Zanacchi, M. Mlodzianoski, A. Diaspro, J. Bewersdorf, S. T. Hess, and K. Braeckmans, "Precisely and accurately localizing single emitters in fluorescence microscopy.," *Nat. Methods*, vol. 11, no. 3, pp. 253–266, 2014.

[86] F. Strubbe, S. Vandewiele, C. Schreuer, F. Beunis, O. Drobchak, T. Brans, and K. Neyts, "Characterizing and tracking individual colloidal particles using Fourier-Bessel image decomposition," *Opt. Express*, vol. 22, no. 20, p. 24635, 2014.

[87] B. C. Carter, G. T. Shubeita, and S. P. Gross, "Tracking single particles: a user-friendly quantitative evaluation.," *Phys. Biol.*, vol. 2, pp. 60–72, 2005.

[88] A. Huhle, D. Klaue, H. Brutzer, P. Daldrop, S. Joo, O. Otto, U. F. Keyser, and R. Seidel, "Camera-based three-dimensional real-time particle tracking at kHz rates and Ångström accuracy," *Nat. Commun.*, vol. 6, p. 5885, 2015.

[89] O. Otto, C. Gutsche, F. Kremer, and U. F. Keyser, "Optical tweezers with 2.5 kHz bandwidth video detection for single-colloid electrophoresis.," *Rev. Sci. Instrum.*, vol. 79, no. 2 Pt 1, p. 023710, Feb. 2008.

[90] S. Keen, J. Leach, G. Gibson, and M. J. Padgett, "Comparison of a high-speed camera and a quadrant detector for measuring displacements in optical tweezers," *J. Opt. A Pure Appl. Opt.*, vol. 9, pp. S264–S266, 2007.

[91] K. Visscher, S. P. Gross, and S. M. Block, "Construction of multiple-beam optical traps with nanometer-resolution position sensing,"

IEEE J. Sel. Top. Quantum Electron., vol. 2, no. 4, pp. 1066–1076, 1996.

[92] P. Wu, R. Huang, C. Tischer, A. Jonas, and E. L. Florin, "Direct measurement of the nonconservative force field generated by optical tweezers," *Phys. Rev. Lett.*, vol. 103, p. 108101, 2009.

[93] R. Huang, B. Lukic, S. Jeney, and E.-L. Florin, "Direct observation of ballistic Brownian motion on a single particle," vol. 7, no. March, pp. 576–580, 2010.

[94] A. . Pralle, M. . Prummer, E.-L. . Florin, E. H. K. . Stelzer, and J. K. H. Hörber, "Three-dimensional high-resolution particle tracking for optical tweezers by forward scattered light.," *Microsc. Res. Tech.*, vol. 44, no. November 1998, pp. 378–386, 1999.

[95] M. W. Allersma, F. Gittes, M. J. deCastro, R. J. Stewart, and C. F. Schmidt, "Two-dimensional tracking of ncd motility by back focal plane interferometry.," *Biophys. J.*, vol. 74, no. 2 Pt 1, pp. 1074–1085, 1998.

[96] F. Gittes and C. F. Schmidt, "Interference model for back-focal-plane displacement detection in optical tweezers.," *Opt. Lett.*, vol. 23, no. 1, pp. 7–9, 1998.

[97] A. Rohrbach and E. H. K. Stelzer, "Three-dimensional position detection of optically trapped dielectric particles," *J. Appl. Phys.*, vol. 91, no. 8, pp. 5474–5488, 2002.

[98] I. A. Martínez and D. Petrov, "Back-focal-plane position detection with extended linear range for photonic force microscopy," vol. 51, no. 25, pp. 5973–5977, 2012.

[99] Y. Jun, S. K. Tripathy, B. R. J. Narayanareddy, M. K. Mattson-hoss, and S. P. Gross, "Calibration of Optical Tweezers for In Vivo Force Measurements : How do Different Approaches Compare ?," *Biophysj*, vol. 107, no. 6, pp. 1474–1484, 2014.

[100] K. Berg-Sørensen and H. Flyvbjerg, "Power spectrum analysis for optical tweezers," *Rev. Sci. Instrum.*, vol. 75, no. 3, pp. 594–612, 2004.

[101] S. F. Tolić-Nørrelykke, E. Schäffer, J. Howard, F. S. Pavone, F. Jülicher, and H. Flyvbjerg, "Calibration of optical tweezers with positional detection in the back focal plane," *Rev. Sci. Instrum.*, vol. 77, p. 103101, 2006.

[102] I. M. Tolić-Nørrelykke, K. Berg-Sørensen, and H. Flyvbjerg, "MatLab program for precision calibration of optical tweezers," *Comput. Phys. Commun.*, vol. 159, pp. 225–240, 2004.

[103] T. Palberg, T. Köller, B. Sieber, H. Schweinfurth, H. Reiber, and G. Nägele, "Electro-kinetics of charged-sphere suspensions explored by integral low-angle super-heterodyne laser Doppler velocimetry," *J. Phys. Condens. Matter*, vol. 24, no. 46, p. 464109, 2012.

[104] F. Strubbe, F. Beunis, and K. Neyts, “Detection of elementary charges on colloidal particles,” *Phys. Rev. Lett.*, vol. 100, no. May, p. 218301, 2008.

[105] W. M. Lee, P. J. Reece, R. F. Marchington, N. K. Metzger, and K. Dholakia, “Construction and calibration of an optical trap on a fluorescence optical microscope.,” *Nat. Protoc.*, vol. 2, no. 12, pp. 3226–38, Jan. 2007.

[106] E. Fällman and O. Axner, “Design for fully steerable dual-trap optical tweezers.,” *Appl. Opt.*, vol. 36, no. 10, pp. 2107–2113, 1997.

[107] “IBIDI µ-Slide VI 0.4.” [Online]. Available: http://ibidi.com/xtproducts/en/ibidi-Labware/Flow-Chambers/m-Slide-VI-0.4. [Accessed: 17-Jun-2015].

[108] Á. Ríos, M. Zougagh, and M. Avila, “Miniaturization through lab-on-a-chip: Utopia or reality for routine laboratories? A review,” *Anal. Chim. Acta*, vol. 740, pp. 1–11, 2012.

[109] M. L. Kovarik, P. C. Gach, D. M. Ornoff, Y. Wang, J. Balowski, L. Farrag, and N. L. Allbritton, “Micro total analysis systems for cell biology and biochemical assays,” *Anal. Chem.*, vol. 84, pp. 516–540, 2012.

[110] X. Xuan, “Joule heating in electrokinetic flow,” *Electrophoresis*, vol. 29, pp. 33–43, 2008.

[111] A. Nakano, T. C. Chao, F. Camacho-Alanis, and A. Ros, “Immunoglobulin G and bovine serum albumin streaming dielectrophoresis in a microfluidic device,” *Electrophoresis*, vol. 32, pp. 2314–2322, 2011.

[112] Z. Ge, W. Wang, and C. Yang, “Analytica Chimica Acta Rapid concentration of deoxyribonucleic acid via Joule heating induced temperature gradient focusing in poly-dimethylsiloxane micro fl uidic channel,” *Anal. Chim. Acta*, vol. 858, pp. 91–97, 2015.

[113] G. Hu, Q. Xiang, R. Fu, B. Xu, R. Venditti, and D. Li, “Electrokinetically controlled real-time polymerase chain reaction in microchannel using Joule heating effect,” *Anal. Chim. Acta*, vol. 557, pp. 146–151, 2006.

[114] V. Miralles, A. Huerre, F. Malloggi, and M.-C. Jullien, “A Review of Heating and Temperature Control in Microfluidic Systems: Techniques and Applications,” *Diagnostics*, vol. 3, pp. 33–67, 2013.

[115] C. D. S. Brites, P. P. Lima, N. J. O. Silva, A. Millán, V. S. Amaral, F. Palacio, and L. D. Carlos, “Thermometry at the nanoscale,” *Nanoscale*, vol. 4, pp. 4799–4829, 2012.

[116] D. Ross, M. Gaitan, and L. E. Locascio, “Temperature Measurement in Microfluidic Systems Using a Temperature-Dependent Fluorescent Dye,” *Anal. Chem.*, vol. 73, no. 17, pp. 4117–4123, 2001.

[117] G. Tang, D. Yan, C. Yang, H. Gong, J. C. Chai, and Y. C. Lam, "Assessment of Joule heating and its effects on electroosmotic flow and electrophoretic transport of solutes in microfluidic channels.," *Electrophoresis*, vol. 27, pp. 628–639, 2006.

[118] L. M. Fu, J. H. Wang, W. B. Luo, and C. H. Lin, "Experimental and numerical investigation into the joule heating effect for electrokinetically driven microfluidic chips utilizing total internal reflection fluorescence microscopy," *Microfluid. Nanofluidics*, vol. 6, pp. 499–507, 2009.

[119] T. Brans, F. Strubbe, C. Schreuer, S. Vandewiele, K. Neyts, and F. Beunis, "Joule heating monitoring in a microfluidic channel by observing the Brownian motion of an optically trapped microsphere," *Electrophoresis*, 2015.

[120] W. A. Kestin, J., Sokolov, M., Wakeham, "Viscosity of liquid water in the range -80C to 150oC," *J. Phys. Chem. Ref. Data*, vol. 7, pp. 941–948, 1978.

[121] M. J. Weber, *Handbook of Optical Materials*. Taylor & Francis, 2002.

[122] R. R. Shannon, *The Art and Science of Optical Design*. Cambridge University Press, 1997.

[123] M. Islinger, C. Eckerskorn, and A. Völkl, "Free-flow electrophoresis in the proteomic era: A technique in flux," *Electrophoresis*, vol. 31, pp. 1754–1763, 2010.

[124] R. Pethig, "Dielectrophoresis: Status of the theory, technology, and applications," *Biomicrofluidics*, vol. 4, p. 022811, 2010.

[125] D. Lide, Ed., *CRC Handbook of Chemistry and Physics:*, 86th ed. 2005.

[126] W. Gobie and C. F. Ivory, "Thermal model of capillary electrophoresis and a method for counteracting thermal band broadening," *J. Chromatogr.*, vol. 516, pp. 191–210, 1990.

[127] C. J. Evenhuis and P. R. Haddad, "Joule heating effects and the experimental determination of temperature during CE," *Electrophoresis*, vol. 30, pp. 897–909, 2009.

[128] Y. Liu, D. K. Cheng, G. J. Sonek, M. W. Berns, C. F. Chapman, and B. J. Tromberg, "Evidence for localized cell heating induced by infrared optical tweezers.," *Biophys. J.*, vol. 68, no. 5, pp. 2137–2144, 1995.

[129] Y. Liu, G. J. Sonek, M. W. Berns, and B. J. Tromberg, "Physiological monitoring of optically trapped cells: assessing the effects of confinement by 1064-nm laser tweezers using microfluorometry.," *Biophys. J.*, vol. 71, no. 4, pp. 2158–2167, 1996.

[130] A. Ashkin, J. M. Dziedzic, and T. Yamane, "Optical trapping and manipulation of single cells using infrared laser beams," *Nature*, vol. 330, no. 6150, pp. 769–771, 1987.

[131] K. C. Neuman and S. M. Block, "Optical trapping," *Rev. Sci. Instrum.*, vol. 75, no. 9, pp. 2787–2809, 2004.

[132] S. Ebert, K. Travis, B. Lincoln, and J. Guck, "Fluorescence ratio thermometry in a microfluidic dual-beam laser trap.," *Opt. Express*, vol. 15, no. 23, pp. 15493–15499, 2007.

[133] M. Jonasz, "Absorption coefficient of water: Data sources (data of Querry MR et al 1991)." [Online]. Available: www.tpdsci.com/Tpc/AbsCfOfWaterDat.php. [Accessed: 17-Apr-2015].

[134] E. J. G. Peterman, F. Gittes, and C. F. Schmidt, "Laser-induced heating in optical traps.," *Biophys. J.*, vol. 84, no. 2, pp. 1308–1316, 2003.

[135] S. Wall, "The history of electrokinetic phenomena," *Curr. Opin. Colloid Interface Sci.*, vol. 15, no. 3, pp. 119–124, 2010.

[136] P. N. Nge, C. I. Rogers, and A. T. Woolley, "Advances in Microfluidic Materials , Functions , Integration , and Applications," vol. 113, pp. 2550–2283, 2013.

[137] M. Campisi, D. Accoto, F. Damiani, and P. Dario, "A soft-lithographed chaotic electrokinetic micromixer for efficient chemical reactions in lab-on-chips," *J. Micro-Nano Mechatronics*, vol. 5, no. 3, pp. 69–76, 2009.

[138] M. Iwata, T. Tanaka, and M. S. Jami, "Application of Electroosmosis for Sludge Dewatering—A Review," *Dry. Technol.*, vol. 31, no. 2, pp. 170–184, 2013.

[139] L. Shui, R. A. Hayes, M. Jin, X. Zhang, P. Bai, A. van den Berg, and G. Zhou, "Microfluidics for electronic paper-like displays," *Lab Chip*, vol. 14, pp. 2374–2384, 2014.

[140] P. M. Reppert and F. D. Morgan, "Frequency-dependent electroosmosis.," *J. Colloid Interface Sci.*, vol. 254, no. 2, pp. 372–383, 2002.

[141] a. Bhattacharyya, J. H. Masliyah, and J. Yang, "Oscillating laminar electrokinetic flow in infinitely extended circular microchannels," *J. Colloid Interface Sci.*, vol. 261, no. 1, pp. 12–20, 2003.

[142] Marcos, C. Yang, T. N. Wong, and K. T. Ooi, "Dynamic aspects of electroosmotic flow in rectangular microchannels," *Int. J. Eng. Sci.*, vol. 42, no. 13–14, pp. 1459–1481, 2004.

[143] D. Erickson and D. Li, "Analysis of alternating current electroosmotic flows in a rectangular microchannel," *Langmuir*, vol. 19, no. 13, pp. 5421–5430, 2003.

[144] X. Xuan and D. Li, "Electroosmotic flow in microchannels with arbitrary geometry and arbitrary distribution of wall charge," *J. Colloid Interface Sci.*, vol. 289, no. 1, pp. 291–303, 2005.

[145] I. Semenov, O. Otto, G. Stober, P. Papadopoulos, U. F. Keyser, and F. Kremer, "Single colloid electrophoresis," *J. Colloid Interface Sci.*, vol. 337, no. 1, pp. 260–264, 2009.

[146] J. A. van Heiningen, A. Mohammadi, and R. J. Hill, "Dynamic electrical response of colloidal micro-spheres in compliant micro-channels from optical tweezers velocimetry.," *Lab Chip*, vol. 10, no. 15, pp. 1907–1921, Aug. 2010.

[147] B. J. Kirby, A. R. Wheeler, R. N. Zare, J. a Fruetel, and T. J. Shepodd, "Programmable modification of cell adhesion and zeta potential in silica microchips.," *Lab Chip*, vol. 3, no. 1, pp. 5–10, 2003.

[148] B. J. Kirby and E. F. Hasselbrink, "Zeta potential of microfluidic substrates: 1. Theory, experimental techniques, and effects on separations," *Electrophoresis*, vol. 25, no. 2, pp. 187–202, 2004.

[149] T. López-León, A. B. Jódar-Reyes, D. Bastos-González, and J. L. Ortega-Vinuesa, "Hofmeister Effects in the Stability and Electrophoretic Mobility of Polystyrene Latex Particles," *J. Phys. Chem. B*, vol. 107, no. 24, pp. 5696–5708, 2003.

[150] H. N. Stein, "Electrokinetics of Polystyrene Particles," in *Interfacial electrokinetics and electrophoresis*, Á. V Delgado, Ed. CRC Press, 2001, pp. 619–639.

[151] I. Semenov, P. Papadopoulos, G. Stober, and F. Kremer, "Ionic concentration- and pH-dependent electrophoretic mobility as studied by single colloid electrophoresis," *J. Phys. Condens. Matter*, vol. 22, p. 494109, 2010.

[152] J. B. Haun, N. K. Devaraj, S. a Hilderbrand, H. Lee, and R. Weissleder, "Bioorthogonal chemistry amplifies nanoparticle binding and enhances the sensitivity of cell detection.," *Nat. Nanotechnol.*, vol. 5, no. 9, pp. 660–665, 2010.

[153] C. Kotsmar, T. Sells, N. Taylor, D. E. Liu, J. M. Prausnitz, and C. J. Radke, "Aqueous solute partitioning and mesh size in HEMA/MAA hydrogels," *Macromolecules*, vol. 45, no. 22, pp. 9177–9187, 2012.

[154] H. M. Said, "Biotin: biochemical, physiological and clinical aspects," in *Water Soluble Vitamins*, O. E. Stanger, Ed. Springer, 2012, pp. 1–19.

[155] S. Ray, R. T. Steven, F. M. Green, F. Höök, B. Taskinen, V. P. Hytönen, and A. G. Shard, "Neutralized Chimeric Avidin Binding at a Reference Biosensor Surface," *Langmuir*, vol. 31, pp. 1921–1930, 2015.

[156] K. De Vos, J. Girones, S. Popelka, E. Schacht, R. Baets, and P. Bienstman, "SOI optical microring resonator with poly(ethylene glycol) polymer brush for label-free biosensor applications," *Biosens. Bioelectron.*, vol. 24, pp. 2528–2533, 2009.

[157] T. Brans, F. Strubbe, C. Schreuer, K. Neyts, and F. Beunis, "Optical tweezing electrophoresis of single biotinylated colloidal particles for

avidin concentration measurement," *J. Appl. Phys.*, vol. 117, no. 21, p. 214704, 2015.

[158] M. Firnkes, D. Pedone, J. Knezevic, M. Döblinger, and U. Rant, "Electrically facilitated translocations of proteins through silicon nitride nanopores: conjoint and competitive action of diffusion, electrophoresis, and electroosmosis.," *Nano Lett.*, vol. 10, no. 6, pp. 2162–7, Jun. 2010.

[159] T. M. Squires, R. J. Messinger, and S. R. Manalis, "Making it stick: convection, reaction and diffusion in surface-based biosensors.," *Nat. Biotechnol.*, vol. 26, no. 4, pp. 417–426, 2008.

[160] A. Densmore, D.-X. Xu, S. Janz, P. Waldron, J. Lapointe, T. Mischki, G. Lopinski, A. Delâge, J. H. Schmid, and P. Cheben, "Sensitive Label-Free Biomolecular Detection Using Thin Silicon Waveguides," *Adv. Opt. Technol.*, vol. 2008, p. 725967, 2008.

[161] F. Vollmer and L. Yang, "Review Label-free detection with high-Q microcavities: a review of biosensing mechanisms for integrated devices," *Nanophotonics*, vol. 1, no. 3–4, pp. 267–291, 2012.